Polycrystalline Plasticity and its Applications to Deformation Processing

by

Srihari Balasubramanian

B.Tech., Mechanical Engineering,
Indian Institute of Technology, Madras, 1992

Submitted to the Department of Mechanical Engineering
in partial fulfillment of the requirements for the degree of

Master of Science in Mechanical Engineering

at the

MASSACHUSETTS INSTITUTE OF TECHNOLOGY

June 1995

Author .....
Department of Mechanical Engineering
May 12, 1995

Certified by .....
Lallit Anand
Professor
Thesis Supervisor

Accepted by .....
Ain Sonin
Chairman, Departmental Committee on Graduate Students

Polycrystalline Plasticity and its Applications to Deformation Processing

by

Srihari Balasubramanian

Submitted to the Department of Mechanical Engineering
on May 12, 1995, in partial fulfillment of the
requirements for the degree of
Master of Science in Mechanical Engineering

Abstract

A rate and temperature dependent crystal plasticity model with a physically-based constitutive law for slip has been proposed. The predictions for simple tension of single crystals for two different forms of hardening models has been investigated. The extension of the forms to represent hardening of polycrystalline response and the modifications required are examined. The predictions of the polycrystalline model are compared with experimental results for a non-homogeneous deformation at an elevated temperature. Also, the problem of ear-formation in deep-drawing has been addressed and the predictive capability of the model for the same is demonstrated for face centered cubic single-crystals and a polycrystal.

Thesis Supervisor: Lallit Anand
Title: Professor

Acknowledgments

I begin by thanking my thesis advisor and mentor, Prof. Lallit Anand, without whose guidance and encouragement this work would not have been possible. Discussions with him have always been educative.

I also thank my colleagues in the lab, Christine Allan, Clarence Chui, Brian Gally, Suryaprakash Ganti, Fred Haubensak, Manish Kothari, Chuang Chia Lin for their helpful suggestions.

My special thanks go to my parents, brother and sister whose affection and constant encouragement has given me tremendous impetus in my academic pursuits.

Contents

List of Figures

List of Tables

Chapter 1

Introduction

The foundations of crystal plasticity date back to the early 1900's. Orowan [1934], Polyani [1934] and Taylor [1934] proposed that plasticity was due to the glide of *dislocations*, which are line defects on crystallographically well-defined slip planes. Taylor ([Taylor, 1938]) was among the first to propose a theory for single crystal and polycrystal deformations based on some careful experiments done on aluminum single crystals and polycrystals ([Taylor and Elam, 1923]). In his polycrystalline model, he assumed that in an aggregate of randomly oriented grains, the deformation in each grain was the same as that at the macroscopic level, and he predicted the tensile stress-strain behavior of the polycrystal based on the single crystal response. His assumption that each grain in the aggregate underwent the same homogeneous deformation satisfied the compatibility requirement by definition, however, the equilibrium of stress across grain boundaries was violated. In his model, he assumed plasticity to be rate-independent and the hardening to be isotropic *i.e.*, all slip systems hardened at an identical rate which was a function of the total accumulated shear strain on all the slip systems.

It had already been established that any arbitrary strain in a polycrystal could be accomodated by just five independent slip systems in each grain([von Mises, 1928]). The availability of more than five slip systems (e.g., twelve in an fcc metal) posed a non-uniqueness in the choice of active slip-systems. Taylor postulated that the active set was chosen by minimizing the net work of plastic deformation done on the

crystal. Though this reduced the number of candidates for the active set, there were still some indeterminacies in the choice. In spite of this ambiguity, his predictions for the macroscopic stress-strain behavior based on this hypothesis agreed reasonably well with experimental observations.

In more recent years, Asaro and Needleman ([Asaro and Needleman, 1985]) extended the regime of application of Taylor-type models to rate-dependent plasticity. The rate-dependence of slip was assumed to be power-law viscoplastic ([Hutchinson, 1976]). The latter serves as a constitutive relation for determining the shearing rate in each slip system unambiguously. The validity of the Taylor-type model and its capabilities to predict texture evolution has been amply demonstrated with extensions to non-homogeneous, non-steady deformations ([Bronkhorst *et al.*, 1992]) and modeling of complex metal-forming processes like rolling, deep-drawing etc ([Chastel and Mathur, 1991] and [Becker *et al.*, 1993]).

An aspect of significance in the modeling of deformation of crystalline materials is the understanding of its hardening with continued deformation. As has already been stated, Taylor assumed an isotropic form for the hardening of the slip systems. The general form of the hardening relationship is

$$\dot{s}^{\alpha} = \sum_{\beta=1}^{N} h^{\alpha\beta}\dot{\gamma}^{\beta};\ \alpha = 1,2,....N;\ \alpha = 1,2,....N \tag{1.1}$$

where s^{α} is the slip system deformation resistance on the α^{th} slip system; $h^{\alpha\beta}$ are the instantaneous hardening modulii which are themselves functions of the deformation and $\dot{\gamma}^{\beta}$ is the shearing rate on slip system β. The diagonal terms in this hardening matrix refer to self-hardening while the off-diagonal terms refer to cross-hardening. Taylor's isotropic hardening rule implies that

$$h^{\alpha\beta} = h;\ \alpha = 1,2,...,N;\ \beta = 1,2,...,N \tag{1.2}$$

Other kinds of hardening that have been proposed include the *independent hardening* (purely diagonal form for the hardening matrix) ([Koiter, 1953]) and *kinematic*

hardening ([Budiansky and Wu, 1962]) where

$$h^{\alpha\beta} = h\,\mathbf{n}^{\alpha}\cdot\mathbf{n}^{\beta};\ \alpha = 1,2,...,N;\ \beta = 1,2,...,N \tag{1.3}$$

where $\mathbf{n}^{\alpha}$ is the normal to the yield surface of the α^{th} slip system.

Pierce, Asaro and Needleman [1983] have used a form of hardening

$$h^{\alpha\beta} = h(\bar{\gamma})\{q + (1-q)\delta_{\alpha\beta}\};\ \alpha = 1,2,...,N;\ \beta = 1,2,...,N \tag{1.4}$$

$$h(\bar{\gamma}) = h_o \text{sech}^2\left[\frac{h_o}{\tau_s - \tau_o}\bar{\gamma}\right] \tag{1.5}$$

where q is the latent hardening parameter chosen in the range $1 < q < 1.4$ ([Kocks, 1970]); h_o is the initial hardening rate; τ_o and τ_s are the critical resolved shear stress and the saturation strength respectively; and $\bar{\gamma}$ is the accumulated slip strain.

Kalidindi, Bronkhorst and Anand [1992] have used a similar form of hardening with a different form for the self-hardening,

$$h^{\alpha\beta} = h^{(\beta)}q^{\alpha\beta} \tag{1.6}$$

$$h^{(\beta)} = h_o\left|\,1 - \frac{s^{(\beta)}}{s_s}\,\right|^{a}\text{sign}\left(1 - \frac{s^{(\beta)}}{s_s}\right) \tag{1.7}$$

Here, $s^{(\beta)}$ is the deformation resistance on slip system β and s_s is the saturation slip system deformation resistance. $[q^{\alpha\beta}]$ is the latent hardening matrix represented as follows

$$[q^{\alpha\beta}] = \begin{Bmatrix} A & q_l A & q_l A & q_l A \\ q_l A & A & q_l A & q_l A \\ q_l A & q_l A & A & q_l A \\ q_l A & q_l A & q_l A & A \end{Bmatrix}, \tag{1.8}$$

where A is a matrix fully-populated by 1's and q_l is the latent hardening factor which is 1 for coplanar systems and $1 \leq q_l \leq 1.4$ for the non-coplanar ones. Kalidindi *et al* [1992] have shown the capability of this form to predict texture evolution and

stress-response in various deformation modes.

More recently, Bassani and Wu [1991] have proposed a model for hardening in single crystals based on some careful experiments on copper single crystals ([Wu *et al.*, 1991]) in which the hardening modulii take the form

$$h^{\alpha\alpha} = \left[(h_o - h_s)\mathrm{sech}^2\left\{\frac{h_o - h_s}{\tau_1 - \tau_o}\gamma^\alpha\right\} + h_s\right]\left[1 + \sum_{\beta=1\beta\neq\alpha}^{N} f^{\alpha\beta}\tanh(\frac{\gamma^\beta}{\gamma_o})\right] \tag{1.9}$$

$$h^{\alpha\beta} = \epsilon h^{\alpha\alpha};\ \alpha \neq \beta;\ \epsilon \ll 1 \tag{1.10}$$

where τ_1 is the stage I strength, *i.e.*, the breakthrough stress level at which large plastic flow initiates; h_o and h_s define the hardening slope immediately following initial yield and during easy glide, respectively; ϵ is a small parameter which defines the off-diagonal terms and $f^{\alpha\beta}$ is an interaction matrix that depends on the nature of the junctions formed between slip systems α and β. Wu, Bassani and Laird [1991] argue that the activation of secondary slip during stage II deformation before tensile overshoot, is inconsistent with the notion of strong latent hardening during single slip for most crystal orientations. They interpret the experimental results as showing a very small latent hardening but high active hardening rate on latent systems. This, they claim, has been overlooked owing to the back extrapolation methods used to estimate the critical resolved shear stress. More recently, Bassani [1993] has proposed a hardening form to include the effects of stage III hardening by assuming that h_s depends on the total accumulated slip $\bar{\gamma} = \sum_\alpha \gamma^\alpha$ on all systems,

$$h_s = {h_s}^I + ({h_s}^{III} - {h_s}^I)\tanh(\frac{\bar{\gamma}}{{\gamma_o}^{III}}) \tag{1.11}$$

where ${\gamma_o}^{III}$ is approximately the accumulated slip at the onset of stage III deformation; ${h_s}^I$ and ${h_s}^{III}$ are the hardening modulii at the beginning of easy glide and stage III deformation respectively.

Plasticity is inherently rate-dependent. The rate effects are due to the thermal activation of various flow processes and therefore plastic flow is also intrinsically

temperature-sensitive. Hence, there is a need to cast the constitutive law for slip based on these considerations. Such a form would not only be more physically-based but also dispense with the issues of non-uniqueness of solutions encountered in the rate-independent framework. The slip-system hardening laws are crucial in predicting observed phenomena such as premature secondary slip, tensile overshoot, etc. in single crystals, though these are not very critical in polycrystal deformations. Finally, there is a need to exercise the sophisticated models in hand and gauge their success in predicting macroscopic shape changes, loads and defect formation during industrial forming operations. These are the issues that this work has tried to address.

In the present study, a rate and temperature dependent single-crystal plasticity model has been outlined. The framework for the constitutive model based on the work of Kalidindi [1992] is presented in Chapter 2. The specific forms of the constitutive functions used are also described. Here, an alternate form for slip based on thermally-activated motion of dislocations is discussed. The Bassani *et al* [1991] hardening form is investigated in this rate-dependent framework. The predictions for monotonic tension of single crystal copper are presented and discussed. The results of the same are compared with those obtained using Kalidindi *et al* [1992] hardening form. The feasibility of extending the forms to represent hardening of polycrystalline response and the modifications required are discussed in in Chapter 3. Predictions of the model for high temperature polycrystal deformation and their comparison with experiments are also shown. The capabilities of the model to predict shape changes and evolution of crystallographic texture in complex bulk-forming processes is illustrated with deep-drawing as an example in Chapter 4. The earing of single crystals and polycrystals is studied. The conclusions are summarised in Chapter 5.

Chapter 2

Single Crystal Plasticity

In this chapter, the framework for a finite-deformation, rate-dependent, temperature-dependent constitutive model for single-crystal plasticity is described. It is essentially an extension of the model proposed by Kalidindi *et al* [1992] to a temperature dependent framework. The specific constitutive forms for the slip and hardening on individual slip systems and the motivation for the same are also discussed. The predictions of single-crystal response for various orientations using the hardening form of Bassani and Wu [1991] implemented in a rate-dependent framework is also presented and compared with predictions from Kalidindi, Bronkhorst and Anand [1992] form of hardening.

2.1 Constitutive model

The basic framework for the constitutive model is as proposed by Kalidindi *et al* [1992]. The stress response of each macroscopic continuum material point is governed by the microstructure associated with it, the latter comprises of the crystal lattice orientation at the material point concerned.

The constitutive equation for the stress at each material point is given by the hyperelastic relation ([Anand, 1985]):

$$\mathbf{T}^* = \mathcal{C}\,[\mathbf{E}^* - \mathbf{A}(\theta - \theta_o)] \tag{2.1}$$

where $\mathbf{E}^*$ is an elastic strain measure given by

$$\mathbf{E}^* = \frac{1}{2}(\mathbf{F}^{*T}\mathbf{F}^* - \mathbf{1}) = \frac{1}{2}(\mathbf{C}^* - \mathbf{1}) \tag{2.2}$$

$\mathcal{C}$ is the fourth-rank anisotropic elasticity tensor; $\mathbf{T}^*$ is a stress measure work-conjugate to the strain measure $\mathbf{E}^*$ related to the Cauchy stress $\mathbf{T}$ by

$$\mathbf{T}^* = \mathbf{F}^{*-1}\{(\det \mathbf{F}^*)\mathbf{T}\}\mathbf{F}^{*-T} \tag{2.3}$$

$\mathbf{A}$ is the thermal expansion tensor; $\mathbf{C}^* = \mathbf{F}^{*T}\mathbf{F}^*$ is the right Cauchy Green tensor; θ is the temperature of the material point and θ_o is a reference temperature.

The local deformation gradient $\mathbf{F}$ is multiplicatively decomposed into an elastic part $\mathbf{F}^*$ and a plastic part $\mathbf{F}^p$ ([Lee, 1969], [Asaro and Needleman, 1985]) as

$$\mathbf{F} = \mathbf{F}^*\mathbf{F}^p;\ \det \mathbf{F}^* > 0,\ \det \mathbf{F}^p = 1 \tag{2.4}$$

According to this mathematical construct, the crystal deforms solely through plastic shearing on crystallographic slip systems from the reference configuration to an intermediate configuration by the plastic deformation gradient $\mathbf{F}^p$. The elastic deformation gradient, $\mathbf{F}^*$ then stretches and rotates the crystalline lattice to bring the crystal to the final configuration.

The evolution of the plastic deformation gradient $\mathbf{F}^p$ is given by the flow rule,

$$\dot{\mathbf{F}}^p = \mathbf{L}^p\mathbf{F}^p \tag{2.5}$$

where $\mathbf{L}^p$ is the local velocity gradient referred to the isoclinic configuration.

$\mathbf{L}^p$ is assumed to arise only from the plastic shearing [1] of individual slip systems of the crystal defined as

$$\mathbf{L}^p = \sum_{\alpha=1}^{N} \dot{\gamma}^\alpha \mathbf{S}_o^\alpha \tag{2.6}$$

[1] Plastic flow is assumed to be only through crystallographic slip. This assumption is reasonable at low homologous temperatures for fcc metals.

where $\dot{\gamma}^\alpha$ is the shearing rate of the α^{th} slip system. The slip system basis $\mathbf{S}_o^\alpha$ is given by

$$\mathbf{S}_o^\alpha = \mathbf{m}_o^\alpha \otimes \mathbf{n}_o^\alpha \tag{2.7}$$

where $\mathbf{m}_o^\alpha$ and $\mathbf{n}_o^\alpha$ are orthonormal directions along the slip direction and slip plane normal respectively. These are time-independent as they are referred to a fixed reference configuration. The particular form of $\mathbf{S}_o^\alpha$ depends on the structure of the crystal.

The plastic shearing rate on the slip system α is given by a constitutive relation

$$\dot{\gamma}^\alpha = \hat{\dot{\gamma}}^\alpha(\tau^\alpha, s^\alpha, \theta) \tag{2.8}$$

where τ^α is the resolved shear stress and s^α is the slip system deformation resistance.

The plastic work rate per unit volume is given as

$$\dot{\omega}^p = (\mathbf{C}^*\mathbf{T}^*) \cdot \mathbf{L}^p = \sum_\alpha \{(\mathbf{C}^*\mathbf{T}^*) \cdot \mathbf{S}_o^\alpha\}\dot{\gamma}^\alpha = \sum_\alpha \tau^\alpha \dot{\gamma}^\alpha \tag{2.9}$$

The resolved shear stress in turn is defined from above as

$$\tau^\alpha = (\mathbf{C}^*\mathbf{T}^*) \cdot \mathbf{S}_o^\alpha \tag{2.10}$$

Since the elastic stretches in metals are small, $\mathbf{C}^* \approx \mathbf{1}$, thus,

$$\tau^\alpha \approx \mathbf{T}^* \cdot \mathbf{S}_o^\alpha \tag{2.11}$$

Positive plastic work during slip on a slip system requires that $\dot{\gamma}^\alpha$ be in the same direction as τ^α.

The constitutive law for slip system hardening is defined through a set of evolution equations for s^α,

$$\dot{s^\alpha} = \sum_\beta h^{\alpha\beta} \mid \dot{\gamma}^\beta \mid \tag{2.12}$$

where $h^{\alpha\beta}$ is the hardening rate on slip system α due to shearing on slip system β.

2.2 Specific Constitutive Functions

In this section, the specific forms for the various constitutive functions and the motivation for the same are discussed. The forms are general and pertain to mechanisms of plastic deformation in crystals with sufficient number of slip systems *i.e.,* greater than five. In this chapter and in later chapters, these forms are presented and tested for fcc materials. But, the same forms could also be used for bcc materials with appropriate changes in the crystallographic planes and directions of slip, the number of slip systems and the material parameters.

2.2.1 Anisotropic elasticity tensor

Due to the nature of crystal symmetry in fcc materials, their elastic properties can be described through three independent elastic constants, C_{11}, C_{12} and C_{44} ([Nye, 1957]) which are defined in terms of the elasticity tensor as :-

$$C_{11} = (\mathbf{e}_1{}^c \otimes \mathbf{e}_1{}^c) \cdot \mathcal{C}[\mathbf{e}_1{}^c \otimes \mathbf{e}_1{}^c], \tag{2.13}$$

$$C_{12} = (\mathbf{e}_1{}^c \otimes \mathbf{e}_1{}^c) \cdot \mathcal{C}[\mathbf{e}_2{}^c \otimes \mathbf{e}_2{}^c], \tag{2.14}$$

$$C_{44} = (\mathbf{e}_1{}^c \otimes \mathbf{e}_2{}^c) \cdot \mathcal{C}[2\,\mathrm{sym}\,\{\mathbf{e}_1{}^c \otimes \mathbf{e}_2{}^c\}], \tag{2.15}$$

where $\mathbf{e}_i{}^c$, $i = 1, 2, 3$ is an orthonormal basis aligned with the [100], [010], [001] directions of the fcc crystal lattice respectively. The values of these constants in this work have been obtained from Simmons and Wang [1971].

Also, for cubic materials,

$$\mathbf{A} = \alpha_e \, \mathbf{1} \tag{2.16}$$

where α_e is the coefficient of thermal expansion.

2.2.2 Constitutive law for slip

Plastic deformation is assumed to occur only through slip on well-defined crystallographic planes and directions. For fcc crystals, these are the twelve

$\{111\}\langle 110\rangle$ slip systems[2]. These slip systems are shown schematically in Figure 2-1. Here, we follow the Schmid and Boas convention ([Schmid and Boas, 1935]) of labeling the slip systems. The slip plane normals and the slip directions referred to an orthonormal basis in the crystal lattice are tabulated in Table 2.1.

The constitutive function for slip in each slip system $\hat{\dot{\gamma}}^\alpha(\tau^\alpha, s^\alpha, \theta)$ in 2.8 is given by

$$\dot{\gamma}^\alpha = \begin{cases} 0 & \text{if } \mid \tau^\alpha \mid < s^{th} \\ \dot{\gamma}_o \exp\left(-\frac{\Delta \hat{G}^*(|\tau^\alpha|, s^\alpha)}{k_B \theta}\right) \text{sign}(\tau^\alpha) & \text{otherwise} \end{cases} \tag{2.17}$$

where $\dot{\gamma}_o$ is a reference shearing rate, s^{th} is a threshold slip system resistance, k_B is the Boltzmann constant, θ is the temperature and ΔG^* is a thermal activation energy ([Kocks *et al.*, 1975]) given as

$$\Delta G^* = F_o \left\{ 1 - \left(\frac{\mid \tau^\alpha \mid - s^{th}}{s^\alpha} \right)^p \right\}^q \tag{2.18}$$

Here, F_o is the Helmholtz free energy and p and q are fit parameters related to the "shape" of the obstacles on the slip plane α ([Frost and Ashby, 1982])

Motivation for the form of the constitutive law for slip

The motivation for the constitutive equation for slip 2.17 has its underpinnings in thermodynamics and kinetics of plastic flow.

Thermodynamics and Kinetics of slip

We now study the kinetics of slip and endeavor to establish a basis for 2.17 based on the fundamental principles of thermodynamics.

Let $\mathcal{P}$ be a representative volume element (RVE) of volume V in a body $\mathcal{B}$. Let α be the index denoting a slip system. The RVE is assumed to deform under a uniform macroscopic stress by straining locally at numerous *sites* ([Kocks *et al.*, 1975]) as shown in Figure 2-2. If the crystals were assumed to deform only through

[2]These comprise the planes of the greatest atomic density and the closest-packed directions within these planes

crystallographic slip, the sites are dislocation loops and the strain transformations are the shear transformations associated with the glide of these dislocation loops. Let us consider a dislocation loop with a Burgers vector of magnitude b^α, area $a^\alpha = \pi r^{\alpha 2}$ and thickness t on the slip system α as shown in Figure 2-3. Here, r^α is the radius of the loop. The shear increment associated with each shear transformation on the slip plane α (see Figure 2-4) is given by

$$\gamma^\alpha{}_{(\mathrm{tr})} \approx \frac{b^\alpha}{h} \tag{2.19}$$

The macroscopic plastic deformation $\mathbf{F}^{p,\alpha}{}_{(\mathrm{tr})}$ on the slip system α associated with this shear transformation is thus,

$$\mathbf{F}^{p,\alpha}{}_{(\mathrm{tr})} = \gamma^\alpha{}_{(\mathrm{tr})}(\mathbf{m}_o^\alpha \otimes \mathbf{n}_o^\alpha) \tag{2.20}$$

$V^\alpha{}_{(\mathrm{tr})}$, the volume associated with each shear transformation, is given by

$$V^\alpha{}_{(\mathrm{tr})} = a^\alpha\, h \tag{2.21}$$

Let N^α be the number of sites undergoing shear transformation on slip system α. The macroscopic velocity gradient in the RVE due to the shear transformations can now be written in terms of the microscopic variables as

$$\mathbf{L}^p = \dot{\mathbf{F}}^p \mathbf{F}^{p-1} = \frac{1}{V}\left\{\sum_\alpha \mathbf{F}^{p,\alpha}{}_{(\mathrm{tr})}(N^\alpha V^\alpha{}_{(\mathrm{tr})})^{\cdot}\right\} \tag{2.22}$$

Substituting for $\mathbf{F}^{p,\alpha}{}_{(\mathrm{tr})}$ and $V^\alpha{}_{(\mathrm{tr})}$ in the expression above we get,

$$\mathbf{L}^p = \sum_\alpha \left[\left\{\frac{b^\alpha N^\alpha 2\pi r^\alpha}{V}\right\}\dot{r}^\alpha + \left\{\frac{b^\alpha \pi r^{\alpha 2}}{V}\right\}\dot{N}^\alpha\right](\mathbf{m}_o^\alpha \otimes \mathbf{n}_o^\alpha) \tag{2.23}$$

Thus, the macroscopic shearing rate on slip system α can be written as

$$\dot{\gamma}^\alpha = \dot{\gamma}^\alpha_{\mathrm{glide}} + \dot{\gamma}^\alpha_{\mathrm{nuc}} \tag{2.24}$$

where $\dot{\gamma}^{\alpha}_{\text{glide}}$ is the shearing due to the glide of the dislocations represented by the first term in the square brackets in 2.23 and $\dot{\gamma}^{\alpha}_{\text{nuc}}$ is the shearing due to nucleation of shear transformation sites represented by the second term in the square brackets in 2.23. Hence,

$$\mathbf{L}^{p} = \sum_{\alpha} \dot{\gamma}^{\alpha}_{\text{glide}} (\mathbf{m}_{o}{}^{\alpha} \otimes \mathbf{n}_{o}{}^{\alpha}) + \sum_{\alpha} \dot{\gamma}^{\alpha}_{\text{nuc}} (\mathbf{m}_{o}{}^{\alpha} \otimes \mathbf{n}_{o}{}^{\alpha}) \tag{2.25}$$

Under the assumption that plastic flow is glide-controlled,

$$\dot{\gamma}^{\alpha}_{\text{glide}} \gg \dot{\gamma}^{\alpha}_{\text{nuc}} \tag{2.26}$$

Thus, the expression for the macroscopic velocity gradient reduces to

$$\mathbf{L}^{p} = \sum_{\alpha} \dot{\gamma}^{\alpha} (\mathbf{m}_{o}{}^{\alpha} \otimes \mathbf{n}_{o}{}^{\alpha}) \approx \sum_{\alpha} \dot{\gamma}^{\alpha}_{\text{glide}} (\mathbf{m}_{o}{}^{\alpha} \otimes \mathbf{n}_{o}{}^{\alpha}) \tag{2.27}$$

where, the shearing rate on the α^{th} slip system $\dot{\gamma}^{\alpha}$ is given by

$$\begin{aligned} \dot{\gamma}^{\alpha} &= \rho^{\alpha}{}_{m}\, b^{\alpha}\, \bar{v}^{\alpha}; \\ \rho^{\alpha}{}_{m} &= \frac{N^{\alpha} 2\pi r^{\alpha}}{V}; \\ \bar{v}^{\alpha} &= \dot{r}^{\alpha} \end{aligned} \tag{2.28}$$

Here, $\bar{v}^{\alpha}$ is the mean expansion velocity of the dislocation loops on slip system α and $\rho^{\alpha}{}_{m}$ is the mobile dislocation density on slip system α. Eqn 2.28 is the generalization of the classical Orowan's relation for finite viscoplastic deformation.

The movement of dislocations is impeded by the presence of two kinds of obstacles: extended obstacles which are also termed as long-range obstacles e.g., dislocation pile-ups within a glide plane and local obstacles, which act only over a few atomic distances e.g., dislocations threading a glide plane. Only the local obstacles can be overcome with the help of thermal fluctuations, under the action of a stress. Fig 2-5 shows a schematic of the two types of obstacles on a slip plane.

Let us now consider the movement of dislocation loops on any one slip system. In

the following discussion, we will drop the index α for convenience. Let the macroscopic deformation process be characterized by an experimental time t_E. As the dislocations glide on a slip plane, they encounter local obstacles (see Fig 2-5), which can be overcome after a mean wait time $t_W \ll t_E$. The dislocations travel between two obstacles in a mean flight time $t_F \ll t_E$. A useful estimate for the mean dislocation velocity is

$$\bar{v} = \frac{l_F}{t_W + t_F} \tag{2.29}$$

where l_F is the mean separation distance between two successive local obstacles on the slip plane. Under the assumption that $t_F \ll t_W$, we can write 2.29 as

$$\bar{v} \approx \frac{l_F}{t_W} = l_F \, {t_W}^{-1} \tag{2.30}$$

From statistical mechanics, the mean time required by a dislocation to overcome a local obstacle through thermal energy fluctuations at a temperature θ is given by

$${t_W}^{-1} = \nu \left[\exp\left\{ -\frac{\Delta G_f}{k_B \, \theta} \right\} - \exp\left\{ -\frac{\Delta G_r}{k_B \, \theta} \right\} \right] \tag{2.31}$$

where ν is a frequency factor expressed as a fraction of the Debye frequency ν_D, $\nu \approx 10^{-2} - 10^{-1} \, \nu_D$; $\nu_D \approx 8$ x 10^{12}sec^{-1}; k_B is the Boltzmann constant; ΔG_f and ΔG_r are the activation energies for the forward and the backward jumps, respectively, between the ground point and saddle point in front of an obstacle. From 2.28, 2.30 and 2.31,

$$\dot{\gamma}^\alpha = b^\alpha \, {\rho^\alpha}_m \, l_F \, \nu \left[\exp\left\{ -\frac{\Delta G_f}{k_B \, \theta} \right\} - \exp\left\{ -\frac{\Delta G_r}{k_B \, \theta} \right\} \right] \tag{2.32}$$

Since, the jumping of a dislocation over a local obstacle takes place within a very short period of time, the activation process can be assumed to occur at a constant stress and temperature. This implies that the approriate choice for the activation energies ΔG_f and ΔG_r in 2.32 is the activation free enthalpy.

In order to evaluate the activation free enthalpy and its dependence on the resolved shear stress on the slip system, let us consider the RVE as the thermodynamic system. Now, let us consider a small variational shear increment $\delta\gamma$ on one slip plane with slip

direction and slip plane normal $\mathbf{m}$ and $\mathbf{n}$ respectively due to a unit plastic process *i.e.*, jumping of a single dislocation line over a local obstacle. The corresponding variation in the free enthalpy of the thermodynamic system is,

$$\delta G = \delta F - \delta W \tag{2.33}$$

where δF is the variation in the Helmholtz free energy of the system and δW is the variational work done on the system. The variation in the free enthalpy with shear is shown schematically in Figure 2-6. The activation free enthalpy change, ΔG^*, as shown in the diagram, is the free enthalpy change in the system when the dislocation moves from the stable configuration (ground point) to the unstable configuration (saddle point).

Let ψ denote the specific energy per unit mass of the thermodynamic system under consideration. The variation in the free energy of the system can be decomposed into the variation in the interaction energy between the dislocation line and the local obstacle, δF_i and the variation in the free energy of the rest of the RVE $\delta\{\int_V \rho\psi \, dV\}$ as follows,

$$\delta F = \delta \left[F_i(\gamma) + \int_V \rho\psi \, dV \right] = \delta F_i(\gamma) \tag{2.34}$$

The variational work is given by

$$\delta W = \int_V \bar{\mathbf{S}} \cdot \delta\mathbf{F} \, dV \tag{2.35}$$

where $\mathbf{F}$ is the deformation gradient and $\bar{\mathbf{S}}$ is the first Piola-Kirchoff stress that is work-conjugate to $\mathbf{F}$ related to the Cauchy stress $\mathbf{T}$ by

$$\bar{\mathbf{S}} = (\det \mathbf{F}^*)\mathbf{T}\mathbf{F}^{-T} \tag{2.36}$$

Using the multiplicative decomposition of $\mathbf{F}$ in 2.36, we have,

$$\bar{\mathbf{S}} = (\det \mathbf{F}^*)\mathbf{T}\mathbf{F}^{*-T}\mathbf{F}^{p-T} \tag{2.37}$$

Also,

$$\delta \mathbf{F} = \delta \mathbf{F}^* \mathbf{F}^p + \mathbf{F}^* \delta \mathbf{F}^p \tag{2.38}$$

Since we have assumed that the stress is constant during the unit plastic process, the elastic strain which gives rise to the stress is also constant, meaning that the elastic deformation gradient $\mathbf{F}^*$ is a constant. Hence, the first term in 2.38 is zero. From 2.38, 2.37 and 2.35, we get,

$$\begin{aligned}
\delta W &= \int_V \mathrm{tr}\left[(\det \mathbf{F}^*)\mathbf{T}\mathbf{F}^{*-T}\mathbf{F}^{p-T}\delta\mathbf{F}^{pT}\mathbf{F}^{*T}\right]\, dV \\
&= \int_V \mathrm{tr}\left[(\det \mathbf{F}^*)(\mathbf{F}^{*T}\mathbf{F}^*)\mathbf{F}^{*-1}\mathbf{T}\mathbf{F}^{*-T}(\delta\mathbf{F}^p\mathbf{F}^{p-1})^T\right]\, dV \\
&= \int_V (\mathbf{C}^*\mathbf{T}^*)\cdot(\delta\mathbf{F}^p\mathbf{F}^{p-1})\, dV \\
&= \int_V (\mathbf{C}^*\mathbf{T}^*)\cdot\delta\gamma\,(\mathbf{m}_o\otimes\mathbf{n}_o)\, dV
\end{aligned} \tag{2.39}$$

From the definition for the resolved shear stress τ^α on slip system α, 2.10, the above equation reduces to

$$\delta W = \int_V \tau\,\delta\gamma\, dV \tag{2.40}$$

From 2.33, 2.34 and 2.40,

$$\delta G = \delta F_i - \int_V \tau\,\delta\gamma\, dV = \frac{\partial F_i(\gamma)}{\partial\gamma}\,\delta\gamma - \int_V \tau\,\delta\gamma\, dV \tag{2.41}$$

As the resolved shear stress τ is a constant during the variation,

$$\delta G = \frac{\partial F_i(\gamma)}{\partial\gamma}\,\delta\gamma - \tau\, V\,\delta\gamma \tag{2.42}$$

Dividing both sides of 2.42 by V,

$$\frac{\delta G}{V} = \left[\left\{\frac{1}{V}\frac{\partial F_i(\gamma)}{\partial\gamma}\right\} - \tau\right]\delta\gamma \tag{2.43}$$

The dependence of the variation in the free enthalpy of the system on the resolved shear stress is evident in 2.43. The two equilibrium positions γ_s and γ_u are the roots

of the equation,

$$\left\{\frac{1}{V}\frac{\partial F_i(\gamma)}{\partial \gamma}\right\} - \tau = 0 \tag{2.44}$$

The term in the curly brackets in 2.44 has the units of stress and is a measure of the resistance to the glide of the dislocation line considered. We shall denote this quantity by s_d and call it the glide resistance on the dislocation. Thus, 2.43 becomes,

$$\frac{\delta G}{V} = s_d\,\delta\gamma - \tau\,\delta\gamma \tag{2.45}$$

The glide resistance on the dislocation changes as the dislocation moves on the slip plane and can be represented schematically by a glide-resistance diagram as shown in Figure 2-7. The stable equilibrium configuration γ_s and the unstable equilibrium configuration γ_u are represented by the points A and B, respectively. The free energy change per unit volume required for the dislocation to move under an applied stress τ from A to B, $\frac{\Delta F^*}{V}$, is given by the area under the glide resistance curve between A and B. A part of this free energy change, shown by the hatched area in Figure 2-7, is provided by the work done per unit volume by the applied stress τ during the change, $\frac{\Delta W^*}{V}$. The remaining part of the free energy change, shown as the cross-hatched area above the $s_d = \tau$ line in Figure 2-7, represents the activation free enthalpy change per unit volume, $\frac{\Delta G^*}{V}$ (see also Figure 2-6). The activation free enthalpy change is thus expressed as,

$$\Delta G^* = V\left[\int_{\gamma_s}^{\gamma_u} s_d\,\delta\gamma - \int_{\gamma_s}^{\gamma_u} \tau\delta\gamma\right] \tag{2.46}$$

Thus, the activation free enthalpy change, ΔG^* required to overcome a local obstacle is a function of the applied stress τ and the glide resistance s_d. The absloute value of the maximum of s_d is the slip system resistance s on the slip system considered. Hence, $\Delta G^* = \Delta\hat{G}^*(\mid \tau \mid, s)$ where τ is the applied resolved shear stress on the slip system and s is the slip system resistance. The foregoing result can be extended to all the slip systems (now we introduce the index α to specify the α^{th} slip system) as,

$$\Delta\hat{G}^* = \Delta\hat{G}^*(\mid \tau^\alpha \mid, s^\alpha) \tag{2.47}$$

Any phenomenological form for $\Delta\hat{G}^*$ must reduce to the free energy change ΔF^* under the absence of an applied resolved shear stress τ^α and must become zero when $\mid \tau^\alpha \mid = s^\alpha$. Keeping this mind, a variety of forms can be proposed which are shown schematically in Figure 2-8. For *box-shaped* obstacles ([Kocks *et al.*, 1975]), this takes a simple linear form,

$$\Delta\hat{G}^*(\mid \tau^\alpha \mid, s^\alpha) = F_o \left(1 - \frac{\mid \tau^\alpha \mid}{s^\alpha}\right) \tag{2.48}$$

where F_o is the activation free energy change. F_o is a measure of the strength of the local obstacle. An order of magnitude estimate for the F_o ([Frost and Ashby, 1982]) is given by

$$F_o \sim \alpha\, \mu\, b^3 \tag{2.49}$$

where μ is the shear modulus[3], b is the magnitude of the Burgers vector and α is a small factor. Ashby [1982] has suggested different values of α based on the *strength* of the obstacles. In this study, $\alpha \approx 0.5$ was found to give good predictions for the macroscopic response.

To account for changes in the *shape* of the obstacles, Kocks, Argon and Ashby [1975] have proposed a form,

$$\Delta\hat{G}^*(\mid \tau^\alpha \mid, s^\alpha) = F_o \left[1 - \left(\frac{\mid \tau^\alpha \mid}{s^\alpha}\right)^p\right]^q \tag{2.50}$$

where $0 \leq p \leq 1$ and $1 \leq q \leq 2$ are shape factors to be determined by fits to macroscopic response. In this study, we adopt this form together with 2.32 to describe the constitutive behavior of slip. Under a large applied resolved shear stress, the reverse activation in 2.32 can be neglected and the constitutive law for slip reduces to

$$\dot{\gamma}^\alpha = b^\alpha\, {\rho^\alpha}_m\, l_F\, \nu \left[\exp\left\{-\frac{\Delta\hat{G}^*(\mid \tau^\alpha \mid, s^\alpha)}{k_B\, \theta}\right\}\right] \tag{2.51}$$

2.51 takes the form of the constitutive law defined in 2.17 with $\dot{\gamma}_o = b^\alpha\, {\rho^\alpha}_m\, l_F\, \nu$. $\dot{\gamma}_o$ is a reference shearing rate which can be considered to be constant

[3]For cubic metals, $\mu = \{C_{44}\, \frac{1}{2}(C_{11} - C_{22})\}^{\frac{1}{2}}$

([Frost and Ashby, 1982]) as $\dot{\gamma}^{\alpha}$ is not very sensitive to changes in $\dot{\gamma}_o$ for large values of ΔG^*.

Thermal activation cannot produce slip when the resolved shear stress is below a threshold value s_{th} ([Kocks *et al.*, 1975]). s_{th} here represents an athermal resistance and is due to long-range internal stresses. As this value is quite small for fcc materials, s_{th} was neglected in our calculations.

Relationship between the viscoplastic power law and the exponential form for shearing

The viscoplastic power law form for the slip is given by the relation ([Kalidindi *et al.*, 1992])

$$\dot{\gamma}^{\alpha} = \dot{\gamma}_o \left\{ \frac{\mid \tau^{\alpha} \mid}{s^{\alpha}} \right\}^{\frac{1}{m}} \text{sign}(\tau^{\alpha}) \tag{2.52}$$

where m is the strain-rate sensitivity parameter.

At a fixed temperature, a rate-sensitivity parameter, m may be defined as

$$\frac{1}{m} = \frac{\partial \ln \mid \dot{\gamma}^{\alpha} \mid}{\partial \ln \mid \tau^{\alpha} \mid}|_{\theta} \tag{2.53}$$

A definition of the strain-rate sensitivity parameter in the lines of 2.53 for the exponential form for the shearing 2.17, gives

$$\frac{1}{m} = \frac{F_o \, p \, q}{k_B \, \theta} \left[1 - \left\{ \frac{\mid \tau^{\alpha} \mid}{s^{\alpha}} \right\}^{p} \right]^{q-1} \left\{ \frac{\mid \tau^{\alpha} \mid - s^{th}}{s^{\alpha}} \right\} \tag{2.54}$$

For simple box-shaped obstacles ($p = q = 1$),

$$\frac{1}{m} \approx \frac{F_o}{k_B \, \theta} \left\{ \frac{\mid \tau^{\alpha} \mid}{s^{\alpha}} \right\} \approx \frac{F_o}{k_B \, \theta} \tag{2.55}$$

2.55 shows a linear dependence of m on the temperature.

2.2.3 Constitutive law for slip system hardening

Slip-system hardening is accounted for by an increase in slip-system deformation resistance with slip. This is given by

$$\dot{s}^{\alpha} = \sum_{\beta} h^{\alpha\beta} \mid \dot{\gamma}^{\beta} \mid \tag{2.56}$$

The hardening matrix $h^{\alpha\beta}$ contains information about the interaction between dislocations on various slip systems and, hence, is very complicated in form.

In theory, knowledge about the interactions between dislocations can be obtained through a calculation of forces on each dislocation due to the elastic stress field of the others. Even with the availability of powerful computing resources, this is a formidable task owing to the large number of dislocations which increase dramatically with strain. Hence, the hardening behavior has to be inferred through macroscopic measurements on single crystals. However, direct measurements of the evolution of the hardening moduli with plastic strain is difficult due to limitations in simultaneously measuring stress and strain increment on different slip systems. Instead, indirect measurements are used to infer hardening rates on different slip systems. This procedure usually involves loading a single crystal in single-slip orientation to activate the most highly stressed (primary) slip-system followed by a secondary test wherein a previously latent slip-system is activated ([Kocks, 1970],[Wu *et al.*, 1991]). Such an experiment provides information about the hardening on active systems and also about the hardening on latent systems due to activity on active systems.

In this work, two forms of hardening are studied:-

(i) Kalidindi, Bronkhorst and Anand, 1992 :-

$$h^{\alpha\beta} = q^{\alpha\beta} h^{(\beta)} \tag{2.57}$$

where $q^{\alpha\beta}$ is the latent hardening matrix which accounts for the interaction between different slip systems.

For fcc crystals ([Pierce *et al.*, 1983]),

$$[q^{\alpha\beta}] = \begin{Bmatrix} A & q_l A & q_l A & q_l A \\ q_l A & A & q_l A & q_l A \\ q_l A & q_l A & A & q_l A \\ q_l A & q_l A & q_l A & A \end{Bmatrix} \tag{2.58}$$

Here, A is a matrix fully-populated by 1's and q_l is the latent hardening factor which is 1 for coplanar systems and slightly greater than 1 for non-coplanar ones. In general, $1 \leq q_l \leq 1.4$ ([Kocks, 1970]).

The form for the self-hardening rate, h^β ([Brown *et al.*, 1989]) is given as

$$h^{(\beta)} = h_o \mid 1 - \frac{s^{(\beta)}}{s_s} \mid^a \text{sign}\left(1 - \frac{s^{(\beta)}}{s_s}\right) \tag{2.59}$$

where h_o is the initial hardening rate and s_s is a saturation value for the deformation resistance s. To account for the rate sensitivity of s_s the following form is adopted,

$$s_s = \tilde{s}\,\{\frac{\mid \dot{\gamma}^\beta \mid}{\dot{\gamma}_o} \exp\left(\frac{F_o}{k_B\,\theta}\right)\}^n \tag{2.60}$$

where, $\tilde{s}$ and n are additional material parameters.

(ii) Bassani and Wu, 1991 :-

$$h^{\alpha\alpha} = \left[(h_o - h_s)\text{sech}^2\left\{\frac{h_o - h_s}{s_1 - s_o}\bar{\gamma}^\alpha\right\} + h_s\right]\left[1 + \sum_{\beta=1\neq\alpha}^{N} f^{\alpha\beta}\tanh(\frac{\bar{\gamma}^\beta}{\gamma_o})\right] \tag{2.61}$$

$$h^{\alpha\beta} = \epsilon h^{\alpha\alpha};\ \alpha \neq \beta;\ \epsilon \ll 1 \tag{2.62}$$

where s_0 is the intital yield, s_1 is the stage I strength, *i.e.*, the breakthrough stress level at which large plastic flow initiates; h_o and h_s define the hardening slope immediately following initial yield and during easy glide, respectively (Figure 2-9); ϵ is a small parameter which defines the off-diagonal terms and $f^{\alpha\beta}$ is an interaction matrix that depends on the nature of the junctions formed between slip systems α and β.

The interaction matrix $f^{\alpha\beta}$ for fcc crystals ([Bassani and Wu, 1991]) is given as

$$f^{\alpha\beta} = \begin{Bmatrix} 0 & C & C & S & G & H & N & G & G & H & S & G \\ C & 0 & C & G & N & G & G & S & H & S & H & G \\ C & C & 0 & H & G & S & G & H & S & G & G & N \\ S & G & H & 0 & C & C & G & N & G & G & S & H \\ G & N & G & C & 0 & C & S & G & H & G & H & S \\ H & G & S & C & C & 0 & H & G & S & N & G & G \\ N & G & G & G & S & H & 0 & C & C & H & G & S \\ G & S & H & N & G & G & C & 0 & C & S & G & H \\ G & H & S & G & H & S & C & C & 0 & G & N & G \\ H & S & G & G & G & N & H & S & G & 0 & C & C \\ S & H & G & S & H & G & G & G & N & C & 0 & C \\ G & G & N & H & S & G & S & H & G & C & C & 0 \end{Bmatrix} \tag{2.63}$$

where

N = a_1 (No junction)

H = a_2 (Hirth lock)

C = a_3 (Coplanar junction)

G = a_4 (Glissile junction)

S = a_5 (Sessile junction)

Here, a_1, a_2,, a_3, a_4 and a_5 are parameters whose values depend on the relative strengths of the junctions.

The Bassani and Wu form differs from the Kalidindi *et al* form in that the former is based on accumulated slip strains which is not a good state variable. Also, by virtue of a small cross-hardening parameter, the $h^{\alpha\beta}$ matrix is rendered positive definite owing to its diagonal dominance.

2.3 Time-integration procedure

The time-integration procedure involves the efficient and accurate computation of the stress $\mathbf{T}$ and the state vector ξ at a time $\tau = t + \Delta t$, given $\mathbf{T}$ and ξ at time t and the deformation gradient $\mathbf{F}$ and the temperature θ at time t and $\tau = t + \Delta t$. The state vector here comprises of the plastic deformation gradient $\mathbf{F}^p$ and the slip system deformation resistance s^α at every material point. Hence, the time-integration procedure requires the updating of the vector $\{\mathbf{F}^p, s^\alpha, \mathbf{T}\}$ for each time step. The macroscopic stress can then be evaluated from 2.1. The crystallographic orientation at each material point can be obtained from $\mathbf{F}(\tau)$ [4], $\mathbf{F}^p(\tau)$ using the relation for lattice rotation as

$$\mathbf{m}^\alpha(\tau) = \mathbf{F}^*(\tau)\mathbf{m}^\alpha{}_o;\ \mathbf{n}^\alpha(\tau) = \mathbf{F}^{*-T}(\tau)\mathbf{n}^\alpha{}_o \tag{2.64}$$

and using the relation 2.4 for $\mathbf{F}^*$.

In an implicit finite element method, Newton-Raphson iterates are used to improve estimates of $\mathbf{F}(\tau)$ so as to satisfy the principle of virtual work to some tolerance. This necessitates the evaluation of a Jacobian [5] which is defined as

$$\mathcal{J} = \frac{\partial \mathbf{T}}{\partial \Delta \mathbf{E}_t} \tag{2.65}$$

which is a measure of the changes in the values of the components of stress $\mathbf{T}$ at a material point with small changes in the incremental strain $\mathbf{E}_t$. The details of the time-integration procedure are given in Appendix A. The objectivity of this procedure for large time steps has been demonstrated by Kalidindi [1992].

The time-integration procedure has been implemented in a user-material subroutine UMAT in ABAQUS-5.2 version IMPLICIT finite element solver and the calculations in the following sections have been performed using the same.

[4] $\mathbf{F}(\tau)$ is the deformation gradient at time τ in an explicit finite element solver and is the *estimated* deformation gradient at time τ in an implicit finite element solver

[5] In an explicit analysis, however, owing to the non-iterative nature of the solver, a Jacobian is not required. See chapter 4, for a detailed discussion of explicit integration schemes

2.4 Predictions of the model for deformation of single crystal

In this section, we simulate isothermal, monotonic tension of a single crystal of OFHC fcc copper at room temperature using the model and the computational procedures presented in the previous sections. In this context, we study both the hardening forms (Bassani *et al* [1991] and Kalidindi *et al* [1992]) and their ability in predicting the slip systems' activity, tensile overshoot and macroscopic response.

The simulations reported here were performed using a single 8-noded C3D8 finite element. The tensile direction is aligned with the element axis. The load faces of the cube are constrained to remain parallel to each other and perpendicular to the loading axis. These boundary conditions simulate a stiff-testing machine in which the clamps are prevented from rotating.

The elastic properties of OFHC copper ([Simmons and Wang, 1971]) are taken as
$C_{11} = 170$ GPa; $C_{12} = 124$ GPa; $C_{44} = 75$ GPa
for both forms of hardening.

2.4.1 Bassani and Wu hardening

The form of hardening is

$$h^{\alpha\alpha} = \left[(h_o - h_s)\mathrm{sech}^2\left\{\frac{h_o - h_s}{s_1 - s_o}\bar{\gamma}^{\alpha}\right\} + h_s\right]\left[1 + \sum_{\beta=1\neq\alpha}^{N} f^{\alpha\beta}\tanh(\frac{\bar{\gamma}^{\beta}}{\gamma_o})\right] \tag{2.66}$$

$$h^{\alpha\beta} = \epsilon h^{\alpha\alpha};\ \alpha \neq \beta;\ \epsilon \ll 1 \tag{2.67}$$

We use the hardening parameters suggested by Bassani and Wu:
$h_o = 90s_o$; $h_s = 1.5s_o$
$s_1 = 1.3s_o$; $\gamma_o = 0.001$; $\epsilon = 0$ (no latent hardening)
$a_1 = a_2 = a_3 = 8$; $a_4 = 15$; $a_5 = 20$

In order to obtain the parameters for the shearing rate 2.17, we fit the macroscopic response of our simulation of monotonic tension with the loading axis along the $[\bar{1}11]$

direction with those of Bassani and Wu. Since the simulations are for isothermal conditions, we use $\theta = \theta_o = 25^oC$. The fit obtained is shown in Figure 2-10. The parameters for the shearing rate obtained from this fit are :-

$\dot{\gamma_o} = 10^6$ sec^{-1}; $F_o = 4.7536$ x 10^{-19} J; $p = q = 1$

$s_o = 1.15$ MPa gave a good fit.

The slip-system activity for this orientation and the rotation of the tensile axis for the same are shown in Figures 2-11(c) and 2-11(b) respectively. The tensile axis does not rotate since this is a stable orientation. Figures 2-11(c) and 2-11(d) show equal activity on six slip systems, B5, B2, C5, C3, A3, A2. The material parameters obtained from the fit are used to predict the response in some other orientations.

Figure 2-12 shows the response in a multislip orientation where the loading axis is along the [001] direction. Eight slip systems, namely, B4, B5, C5, C3, D4, D6, A3, A6 are equally active as shown in Figure 2-12(c). Though the stability of this orientation in tension is well-predicted [Figure 2-12(b)], the macroscopic response does not show non-linear hardening and saturation.

Figure 2-13 shows the evaluated response for the single-slip orientation [$\bar{2}36$]. For this orientation, the primary slip system is A3. Stage I (easy-glide) is manifest as the initial region of low-hardening rate in the τ-γ curve for A3 in Figure 2-13(d). During stage I, the tensile axis rotates on a great circle towards the primary slip direction [$\bar{1}01$] of A3. Figure 2-13(c) shows fine activity on the conjugate slip system B5 during stage I. Since latent hardening is absent, the hardening matrix $[h^{\alpha\beta}]$ for the stage I is diagonal with

$$h^{11} = \left[(h_o - h_s)\text{sech}^2\left\{\frac{h_o - h_s}{s_1 - s_o}\bar{\gamma}^1\right\} + h_s\right] \tag{2.68}$$

$$h^{\alpha\alpha} = h_o\left[1 + f^{\alpha 1}\tanh(\frac{\bar{\gamma}^1}{\gamma_o})\right] \tag{2.69}$$

Here, the index 1 represents the primary slip system and α represents all the other slip systems. Eqn 2.69 implies that the conjugate slip system B5 shows high active hardening during stage I. By the time the tensile axis rotates and reaches the symmetry boundary [001]-[$\bar{1}11$], B5 hardens much more than A3. As a consequence, the loading axis overshoots the symmetry boundary even in the absence of latent

hardening [Figure 2-13(b)]. At about a tensile strain of $\epsilon = 0.1$, the conjugate slip system B5 begins to show significant activity. Since the shearing rate on both the slip systems after this strain is the same, the tensile axis rotates in a direction parallel to the [001]-[$\bar{1}$11] symmetry boundary.

2.4.2 Kalidindi, Bronkhorst and Anand hardening

The form of hardening is

$$h^{\alpha\beta} = q^{\alpha\beta} h^{(\beta)} \tag{2.70}$$

$$q^{\alpha\beta} = \begin{Bmatrix} A & q_l A & q_l A & q_l A \\ q_l A & A & q_l A & q_l A \\ q_l A & q_l A & A & q_l A \\ q_l A & q_l A & q_l A & A \end{Bmatrix} \tag{2.71}$$

Here, A is a matrix fully-populated by 1's and q_l is the latent hardening factor which is 1 for coplanar systems and $1 \leq q_l \leq 1.4$.

$$h^{(\beta)} = h_o \left| 1 - \frac{s^{(\beta)}}{s_s} \right|^a \text{sign}\left(1 - \frac{s^{(\beta)}}{s_s}\right) \tag{2.72}$$

Following the work of Kalidindi *et al* [1992], the hardening parameters are obtained by fitting the macroscopic response to the experiments of Kalidindi [1992] of simple compression of copper single crystal along [011] direction [see Figure 2-14]. The hardening parameters are:-

$h_o = 300$ MPa; $s_o = 19$ MPa; $s_s = 215$ MPa; $a = 2.2$; $n = 0$; $q_l = 1.4$

For the purpose of comparison, the parameters for the slip rate equation, $\dot{\gamma}_o = 10^6$ sec^{-1}; $F_o = 4.7536$ x 10^{-19} J; $p = q = 1$ are the same as used for the Bassani *et al* model.

The stability of the [011] orientation under compression is well-predicted [as seen in Figure 2-15(b)]. Figures 2-16 and 2-17 show predicitons for the multislip orientations [001] and [$\bar{1}$11]. The principal difference in the predictions of the two different hardening forms is in the form of the macroscopic response. Bassani *et al*

hardening shows linear hardening [Figure 2-12(a)] while Kalidindi *et al* hardening shows non-linear hardening and saturation [Figure 2-16(a)].

Figure 2-18 shows predictions for the single-slip orientation [$\bar{2}36$]. In comparison with Figure 2-13, we see that the tensile overshoot in Figure 2-18(b) is larger than in Figure 2-13(b). This is due to the strong latent hardening in the latter. The conjugate slip system B5 becomes active at a tensile strain which is slightly larger than $\epsilon = 0.1$. This is followed by the rotation of the tensile axis. But, the rotation is not quite parallel to the symmetry boundary due to the slightly different shearing rates on A3 and B5 (seen in the slight difference in slopes in A3 and B5 after $\epsilon = 0.1$ in Figure 2-18(c)). The stress-strain response [Figure 2-18(a)], however, does not show a region of low hardening, as seen in Figure 2-13(a). This is because of the difference in the nature of the self hardening terms in both the models. As is evident from Figure 2-9, the Bassani *et.al* form has a region of low hardening while the Kalidindi *et.al* form lacks such a facility.

In conclusion, we see that although the Bassani *et al* form captures easy glide, tensile overshoot etc., it lacks a non-linear stress-strain response and saturation of stress at large strains. Also, the hardening is dependent on the accumulated slip $\bar{\gamma}$ which is not a good state variable. The macroscopic linear hardening is a consequence of neglecting the stage III effects. Bassani [1993] has suggested a way to include the effects of stage III hardening by assuming that the hardening slope during easy glide h_s evolves with the accumulated slip $\bar{\gamma} = \sum_\alpha \gamma^\alpha$ on all slip systems,

$$h_s = {h_s}^I + ({h_s}^{III} - {h_s}^I)\tanh(\frac{\bar{\gamma}}{{\gamma_o}^{III}}) \tag{2.73}$$

where ${\gamma_o}^{III}$ is approximately the accumulated slip at the onset of stage III deformation; ${h_s}^I$ and ${h_s}^{III}$ are the hardening modulii in the beginning of easy glide and stage III deformation respectively. This form has not be investigated in this study. In contrast with the Bassani *et al* form, the Kalidindi *et al* form exhibits non-linear stress-strain response and saturation of stress at large strains. It predicts the response in multislip orientations well, however, it does not capture easy-glide for

single-slip orientations.

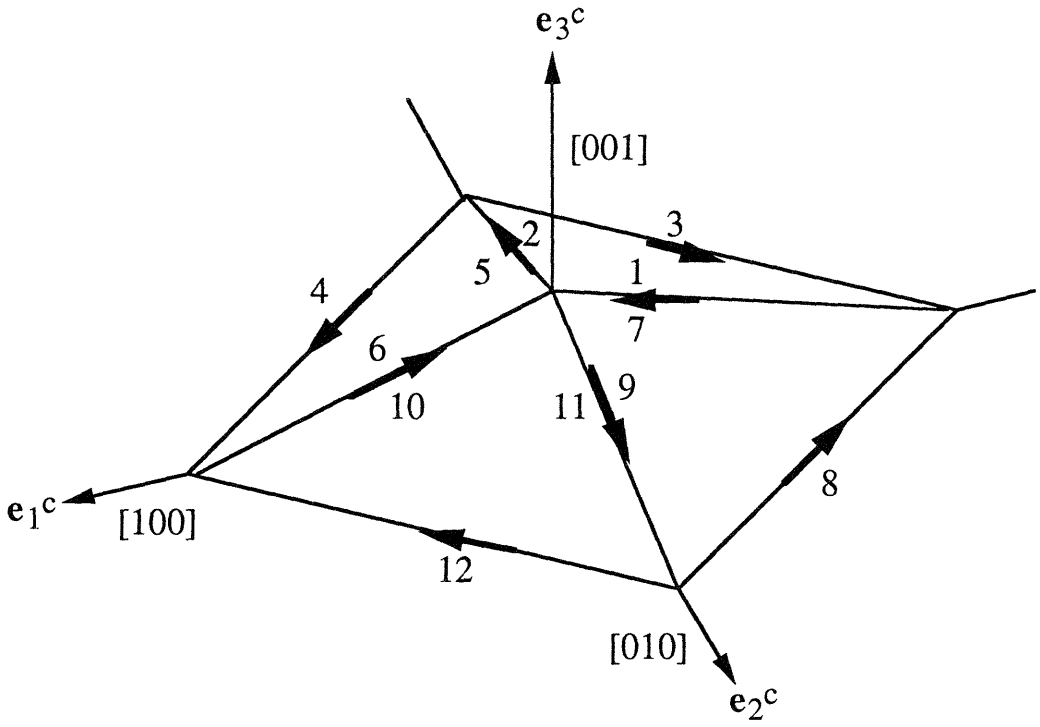

Figure 2-1: Schmid and Boas convention for slip systems in fcc crystals

α	Label	$[\mathbf{m}_o^\alpha]_c$	$[\mathbf{n}_o^\alpha]_c$
1	B4	$\frac{1}{\sqrt{2}}\ 0\ \frac{1}{\sqrt{2}}$	$\frac{1}{\sqrt{3}}\ \frac{1}{\sqrt{3}}\ -\frac{1}{\sqrt{3}}$
2	B5	$0\ \frac{1}{\sqrt{2}}\ \frac{1}{\sqrt{2}}$	$\frac{1}{\sqrt{3}}\ \frac{1}{\sqrt{3}}\ -\frac{1}{\sqrt{3}}$
3	B2	$\frac{1}{\sqrt{2}}\ -\frac{1}{\sqrt{2}}\ 0$	$\frac{1}{\sqrt{3}}\ \frac{1}{\sqrt{3}}\ -\frac{1}{\sqrt{3}}$
4	C1	$\frac{1}{\sqrt{2}}\ \frac{1}{\sqrt{2}}\ 0$	$\frac{1}{\sqrt{3}}\ -\frac{1}{\sqrt{3}}\ \frac{1}{\sqrt{3}}$
5	C5	$0\ \frac{1}{\sqrt{2}}\ \frac{1}{\sqrt{2}}$	$\frac{1}{\sqrt{3}}\ -\frac{1}{\sqrt{3}}\ \frac{1}{\sqrt{3}}$
6	C3	$\frac{1}{\sqrt{2}}\ 0\ -\frac{1}{\sqrt{2}}$	$\frac{1}{\sqrt{3}}\ -\frac{1}{\sqrt{3}}\ \frac{1}{\sqrt{3}}$
7	D4	$\frac{1}{\sqrt{2}}\ 0\ \frac{1}{\sqrt{2}}$	$\frac{1}{\sqrt{3}}\ -\frac{1}{\sqrt{3}}\ -\frac{1}{\sqrt{3}}$
8	D1	$\frac{1}{\sqrt{2}}\ \frac{1}{\sqrt{2}}\ 0$	$\frac{1}{\sqrt{3}}\ -\frac{1}{\sqrt{3}}\ -\frac{1}{\sqrt{3}}$
9	D6	$0\ \frac{1}{\sqrt{2}}\ -\frac{1}{\sqrt{2}}$	$\frac{1}{\sqrt{3}}\ -\frac{1}{\sqrt{3}}\ -\frac{1}{\sqrt{3}}$
10	A3	$\frac{1}{\sqrt{2}}\ 0\ -\frac{1}{\sqrt{2}}$	$\frac{1}{\sqrt{3}}\ \frac{1}{\sqrt{3}}\ \frac{1}{\sqrt{3}}$
11	A6	$0\ -\frac{1}{\sqrt{2}}\ \frac{1}{\sqrt{2}}$	$\frac{1}{\sqrt{3}}\ \frac{1}{\sqrt{3}}\ \frac{1}{\sqrt{3}}$
12	A2	$\frac{1}{\sqrt{2}}\ -\frac{1}{\sqrt{2}}\ 0$	$\frac{1}{\sqrt{3}}\ \frac{1}{\sqrt{3}}\ \frac{1}{\sqrt{3}}$

Table 2.1: Components of $\mathbf{m}_0^\alpha$ and $\mathbf{n}_0^\alpha$ referred to an orthonormal basis $\{\mathbf{e}_i{}^c\}$ associated with the crystal lattice for fcc crystals

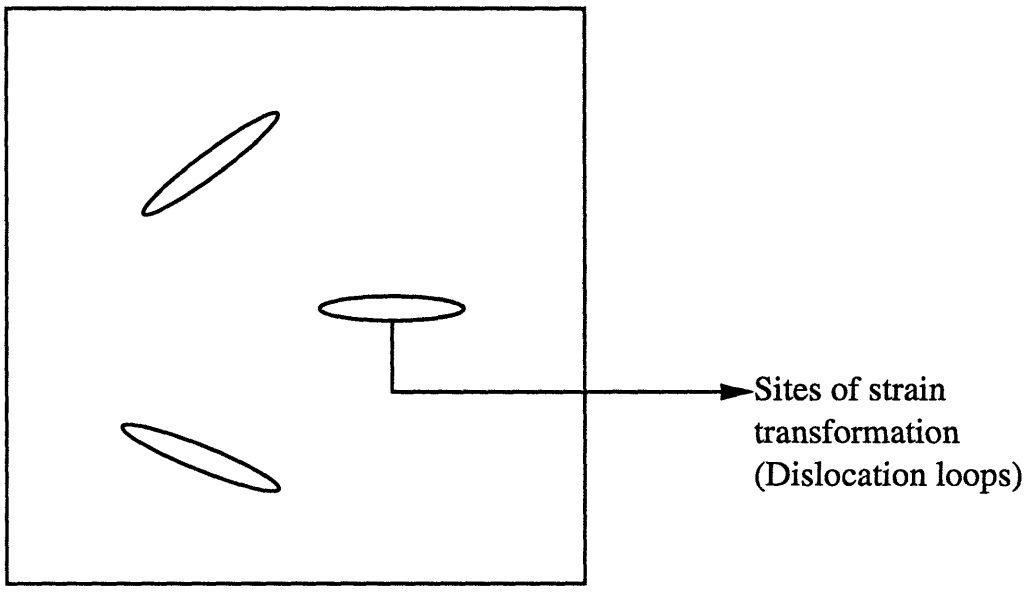

Figure 2-2: Representative volume element with *sites* of strain transformation

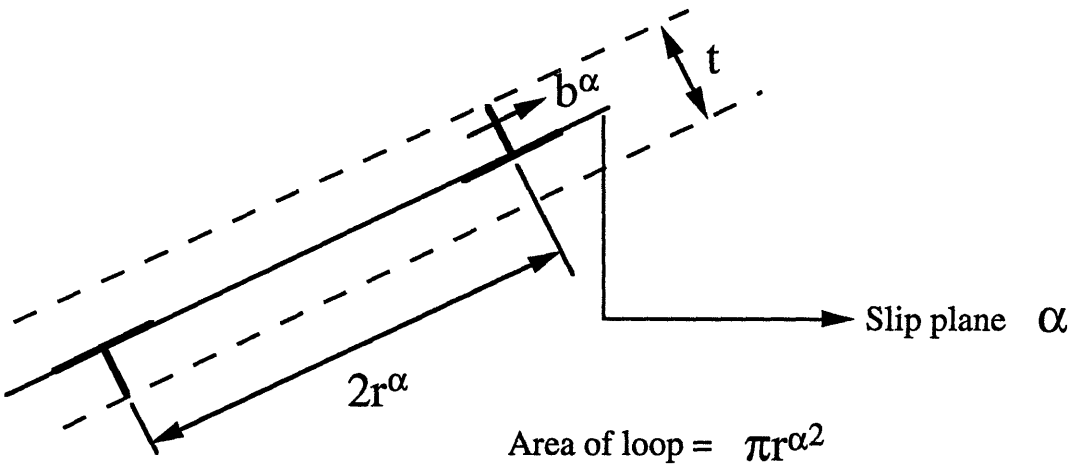

Figure 2-3: A representative dislocation loop on a slip plane

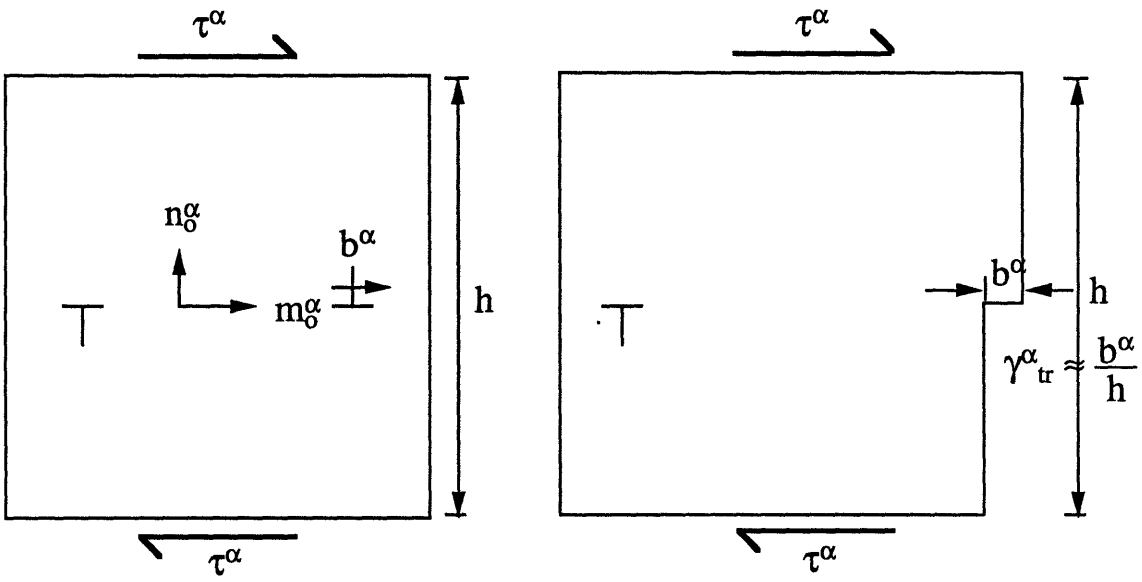

Figure 2-4: A dislocation loop emerging out of the crystal and forming a slip step

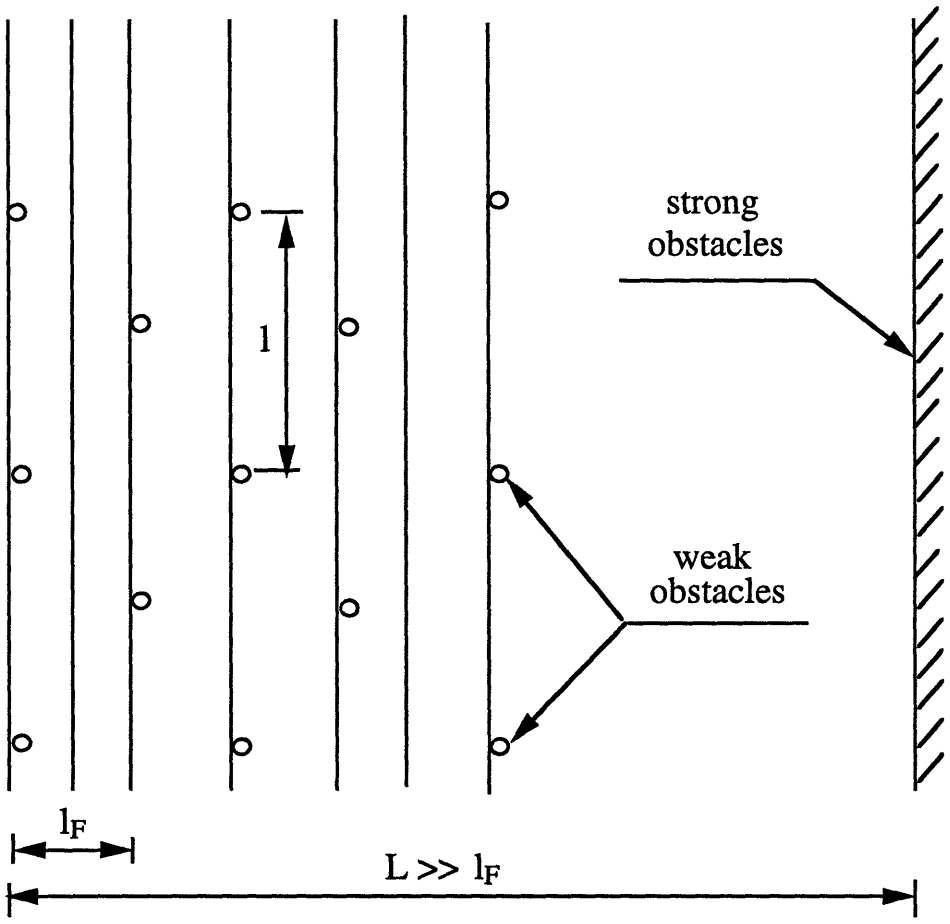

Figure 2-5: Schematic representation of the gliding dislocations on a slip plane (from Teodosiu *et al* [1976])

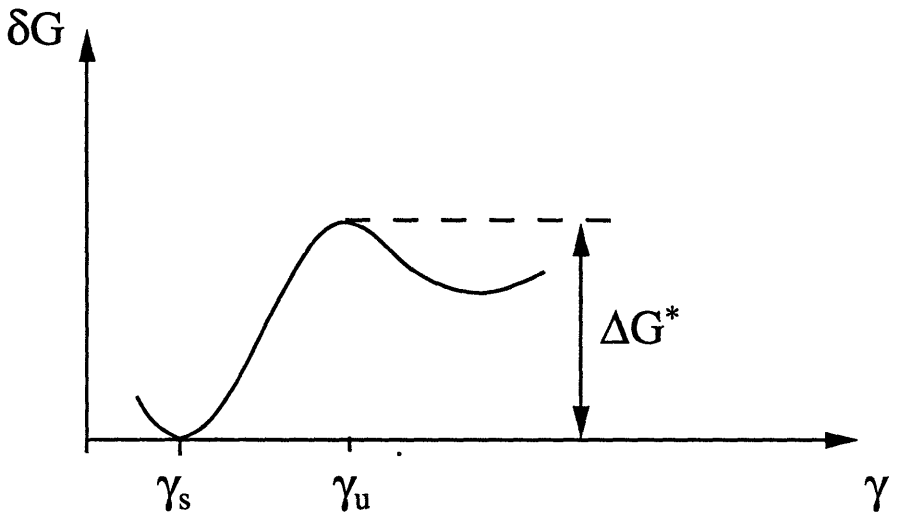

Figure 2-6: Schematic diagram of the variation in the free enthalpy with shear

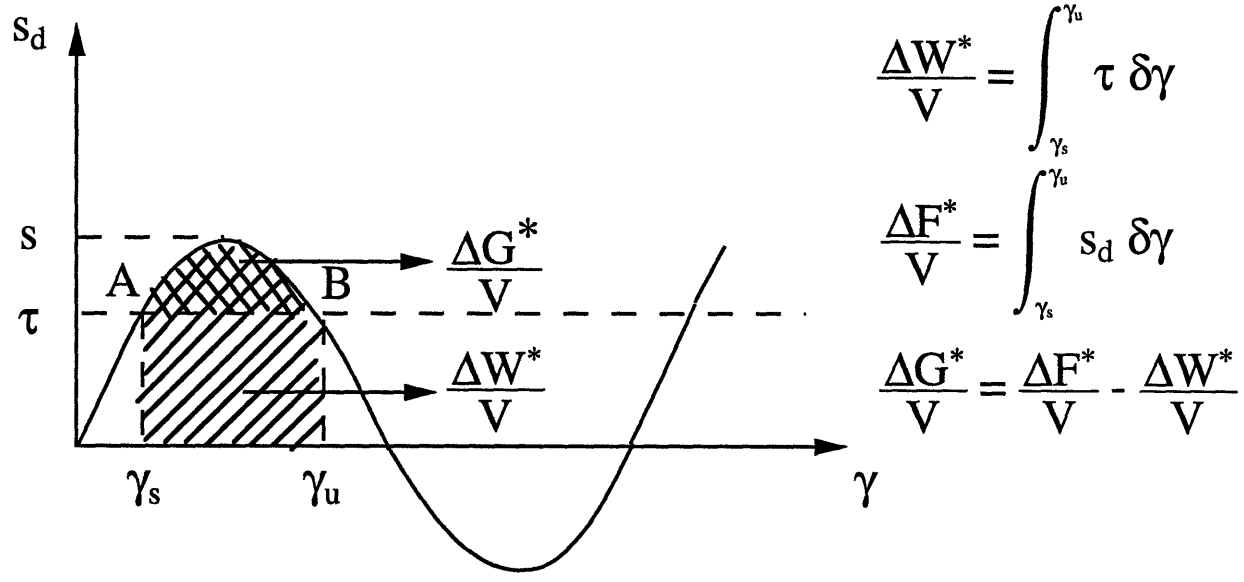

Figure 2-7: Schematic diagram of thermal activation of a unit plastic process

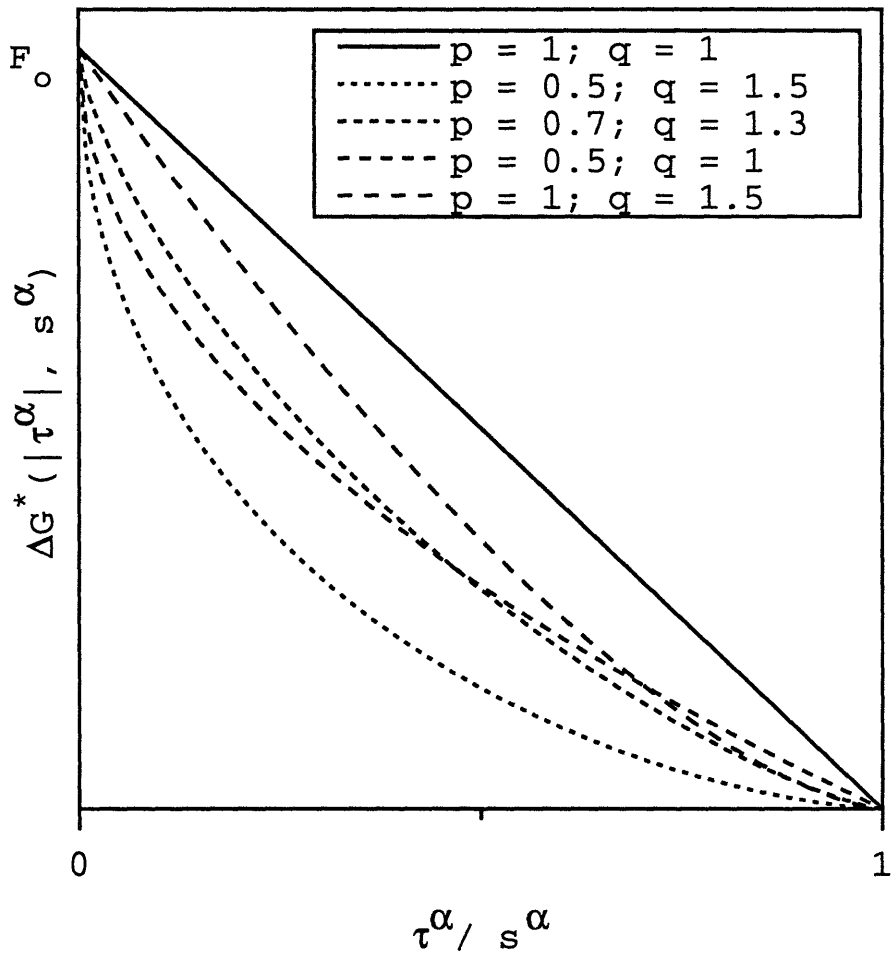

Figure 2-8: Schematic diagram of variation of $\Delta G^*(\mid \tau^\alpha \mid, s^\alpha)$ with $\frac{\tau^\alpha}{s^\alpha}$ for different values of parameters p and q

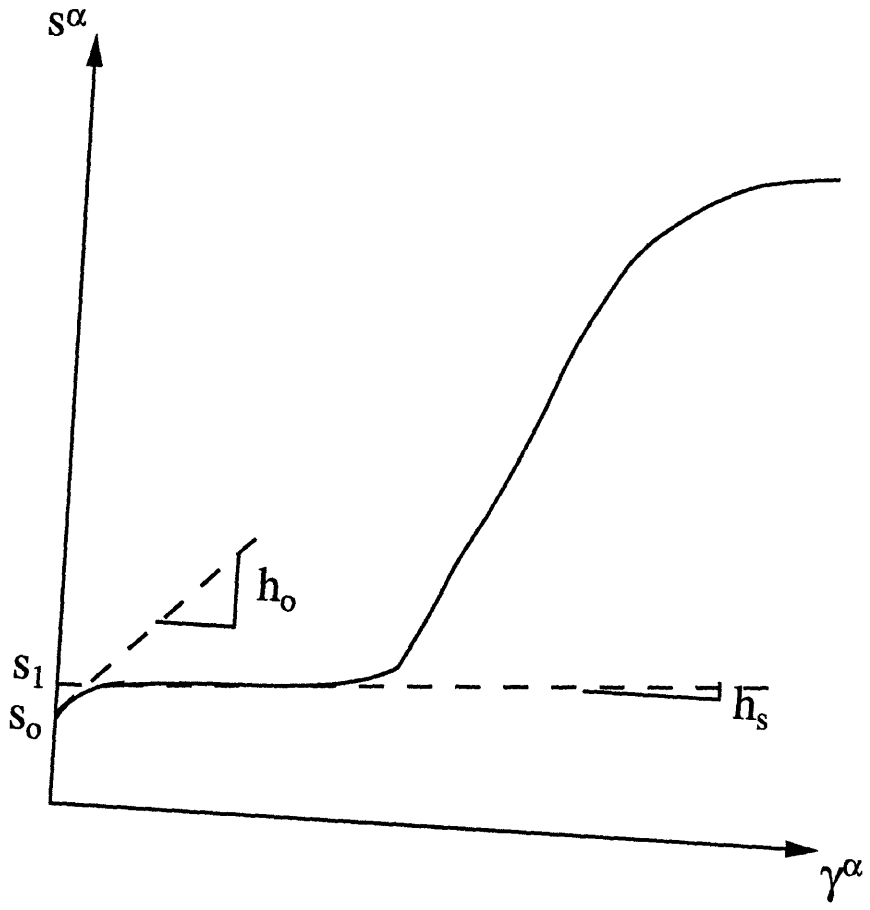

Figure 2-9: Schematic diagram for the Bassani and Wu [1991] form of hardening

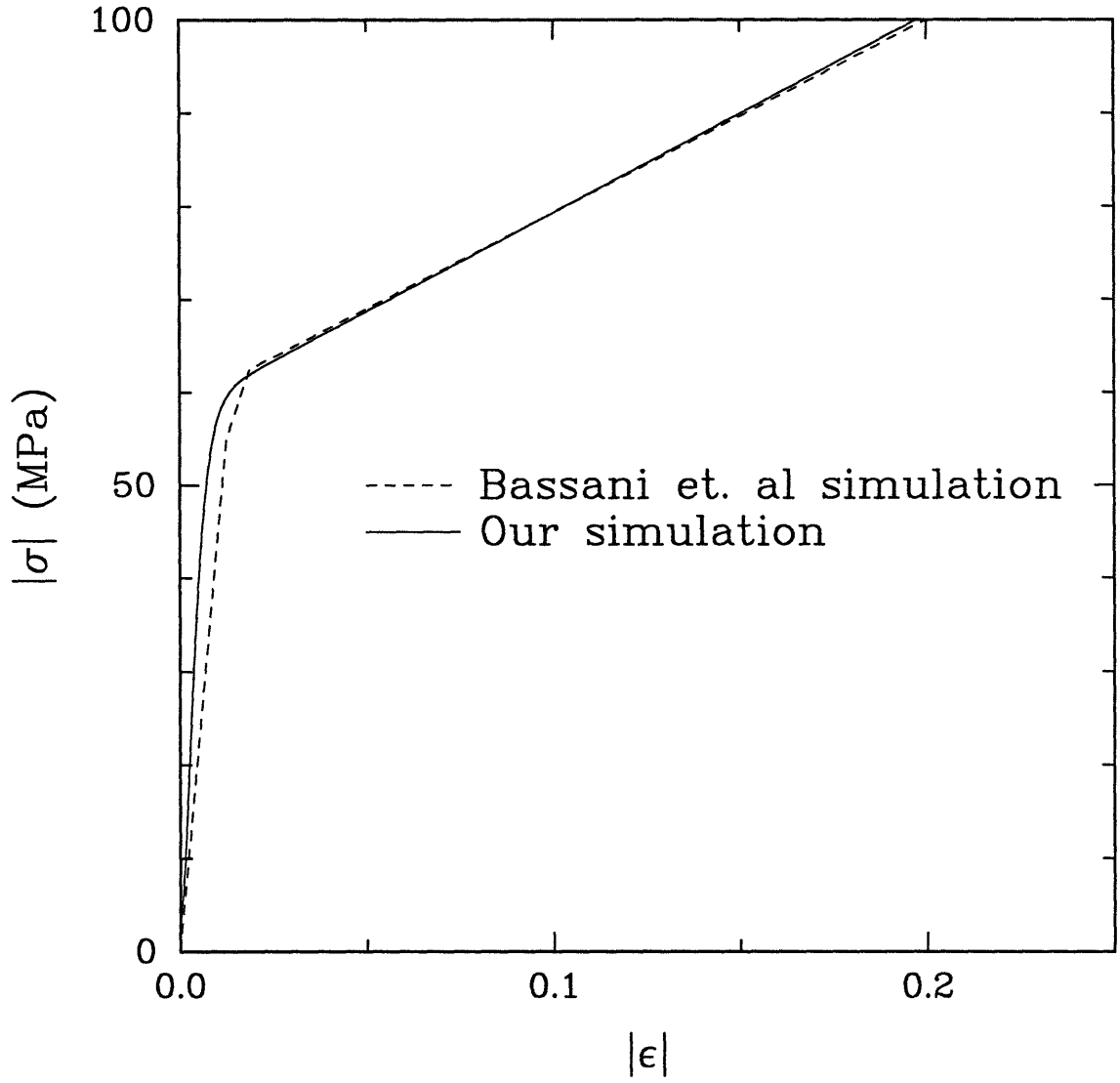

Figure 2-10: The fit for macroscopic response for simple tension of copper single crystal with the loading axis along the [$\bar{1}$11] direction, Bassani and Wu [1991] hardening

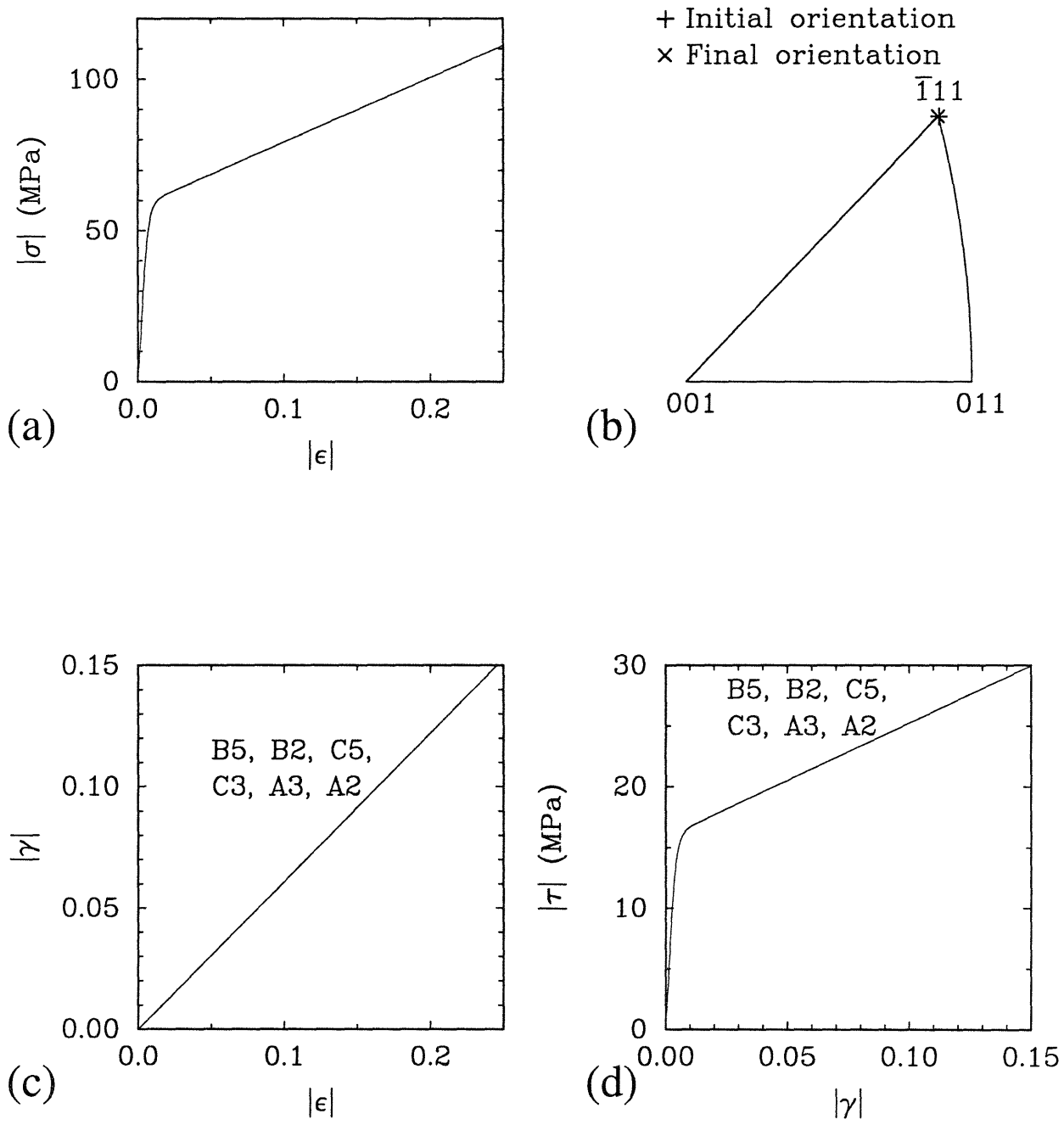

Figure 2-11: Simple tension of copper single crystal with the loading axis along the $[\bar{1}11]$ direction, Bassani and Wu [1991] hardening: (a) The macroscopic stress-strain response (b) The evolution of the orientation of the loading axis (c) The accumulated slip vs. macroscopic strain for active slip systems (d) The shear stress-shear strain response on active slip systems

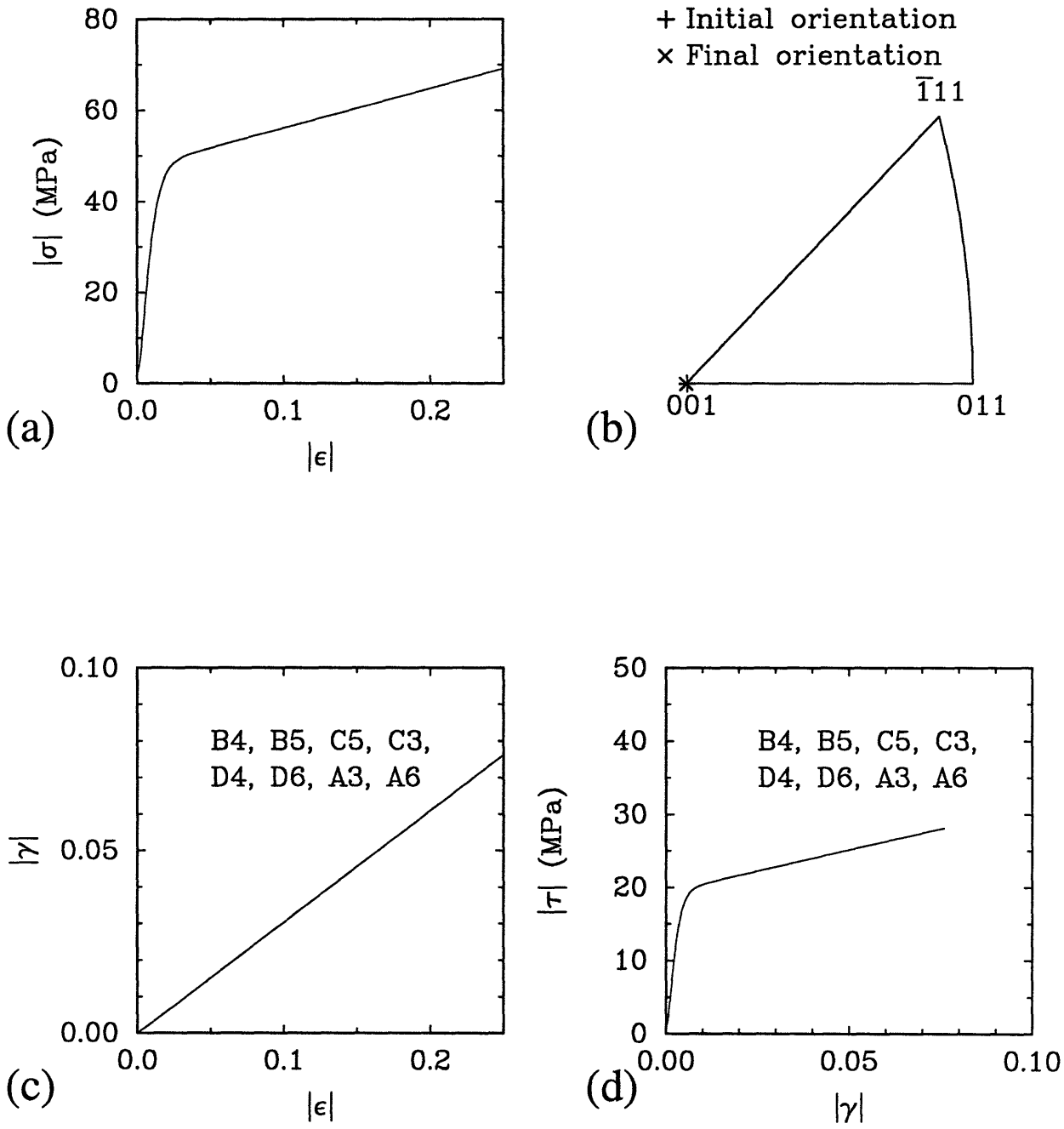

Figure 2-12: Simple tension of copper single crystal with the loading axis along the [001] direction, Bassani and Wu [1991] hardening: (a) The macroscopic stress-strain response (b) The evolution of the orientation of the loading axis (c) The accumulated slip vs. macroscopic strain for active slip systems (d) The shear stress-shear strain response on active slip systems

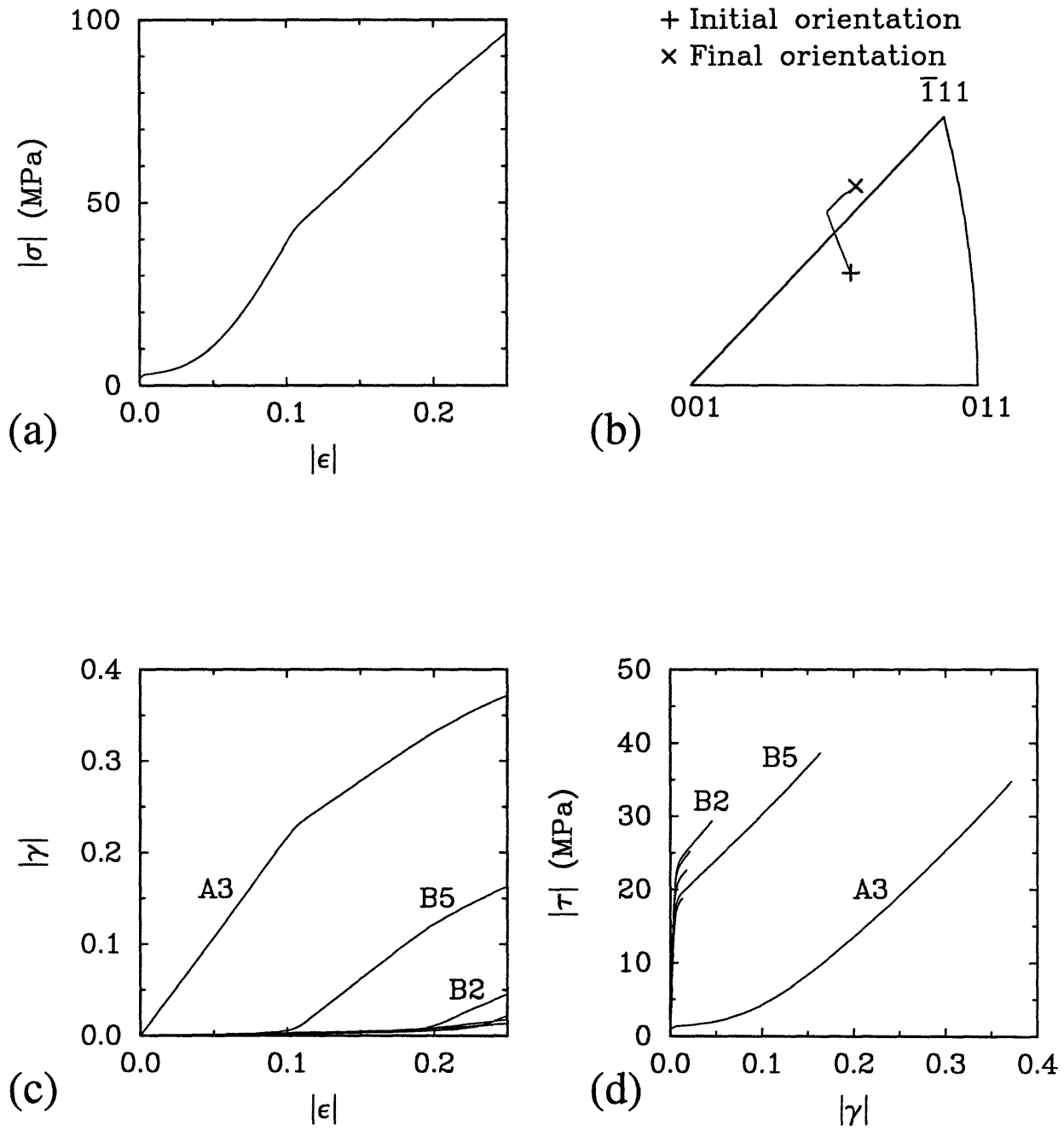

Figure 2-13: Simple tension of copper single crystal with the loading axis along the $[\bar{2}36]$ direction, Bassani and Wu [1991] hardening: (a) The macroscopic stress-strain response (b) The evolution of the orientation of the loading axis (c) The accumulated slip vs. macroscopic strain for active slip systems (d) The shear stress-shear strain response on active slip systems

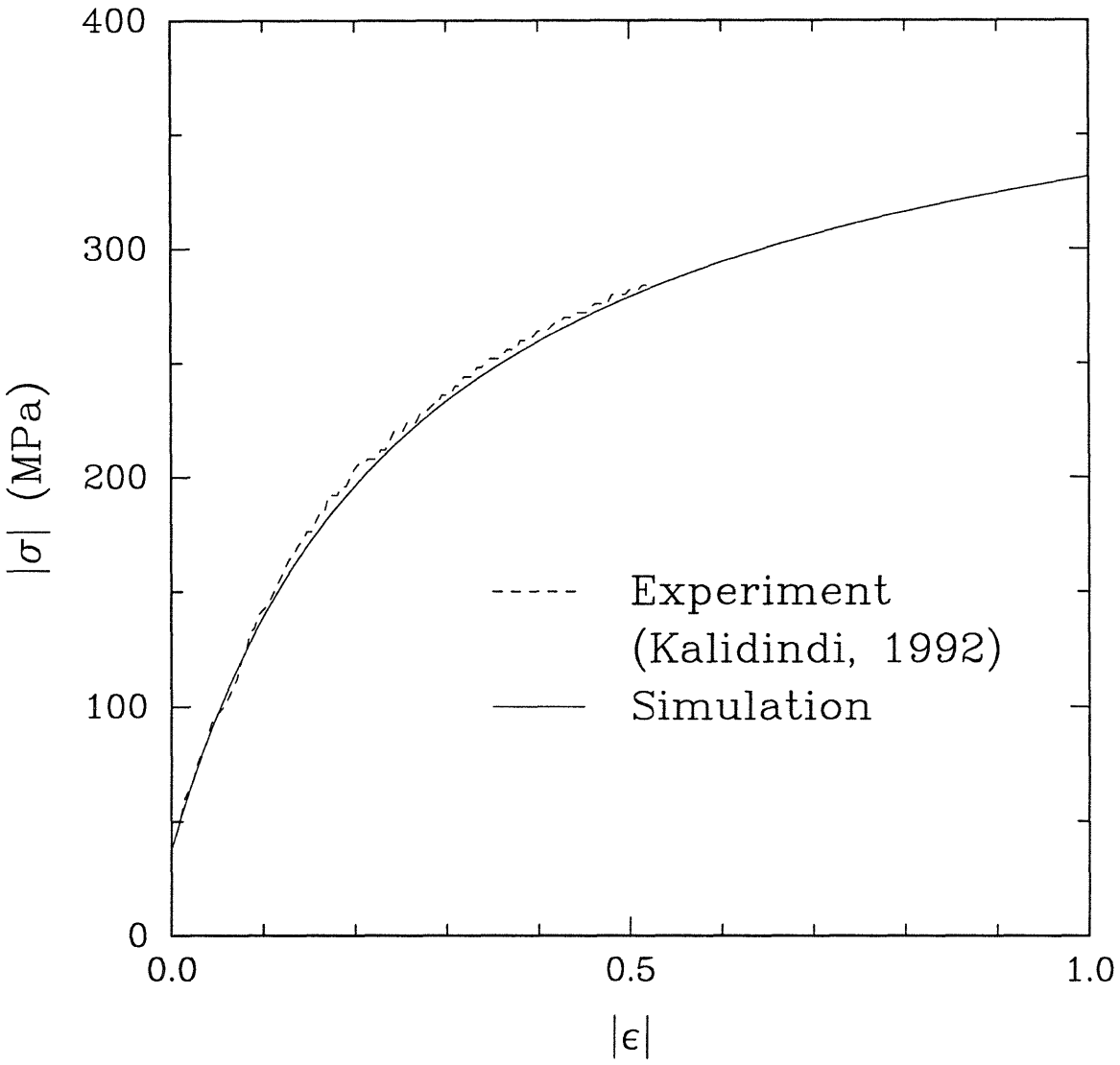

Figure 2-14: The fit for macroscopic response for simple compression of copper single crystal with the loading axis along the [011] direction, Kalidindi *et al* [1992] hardening

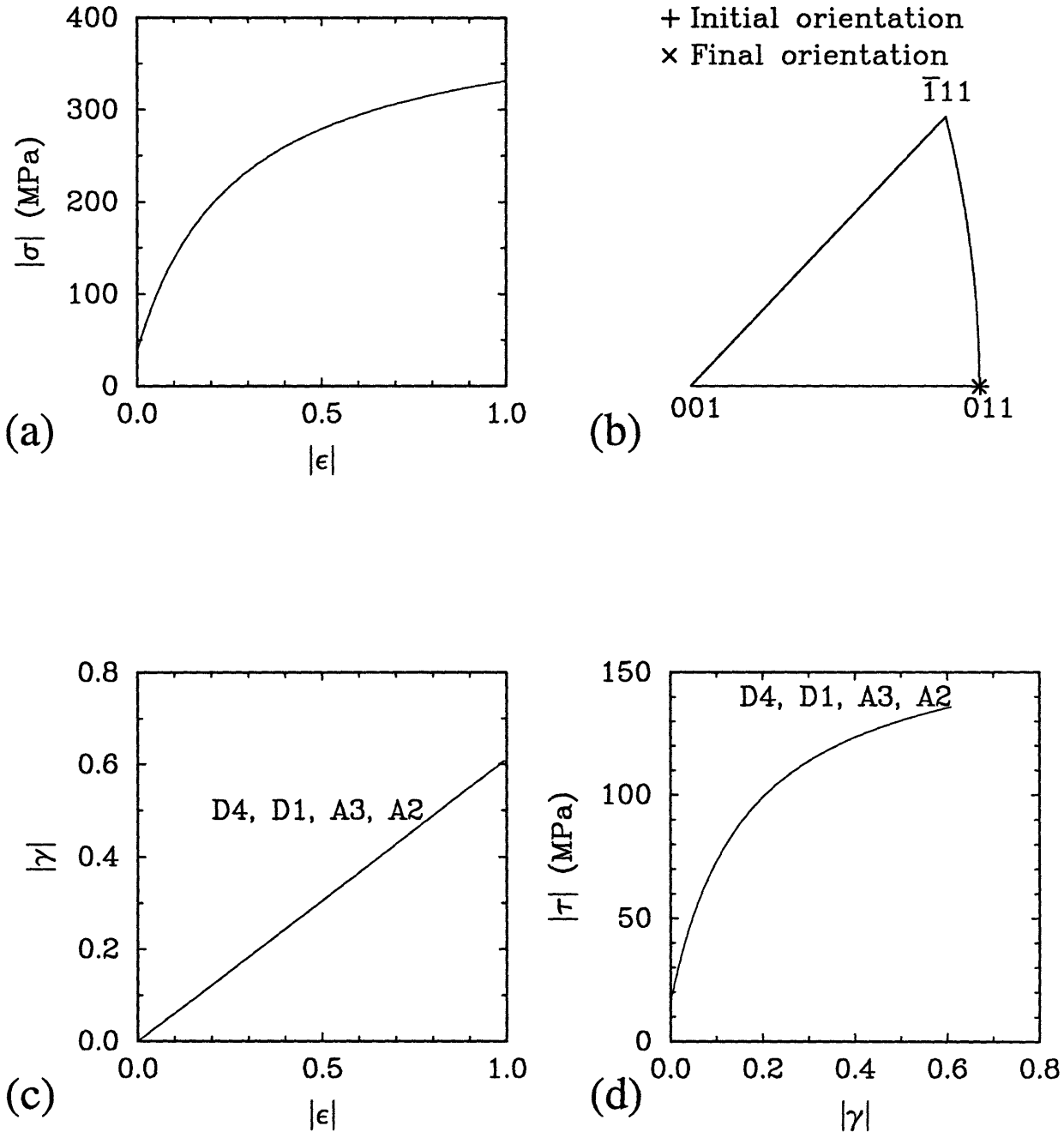

Figure 2-15: Simple compression of copper single crystal with the loading axis along the [011] direction, Kalidindi *et al* [1992] hardening: (a) The macroscopic stress-strain response (b) The evolution of the orientation of the loading axis (c) The accumulated slip vs. macroscopic strain for active slip systems (d) The shear stress-shear strain response on active slip systems

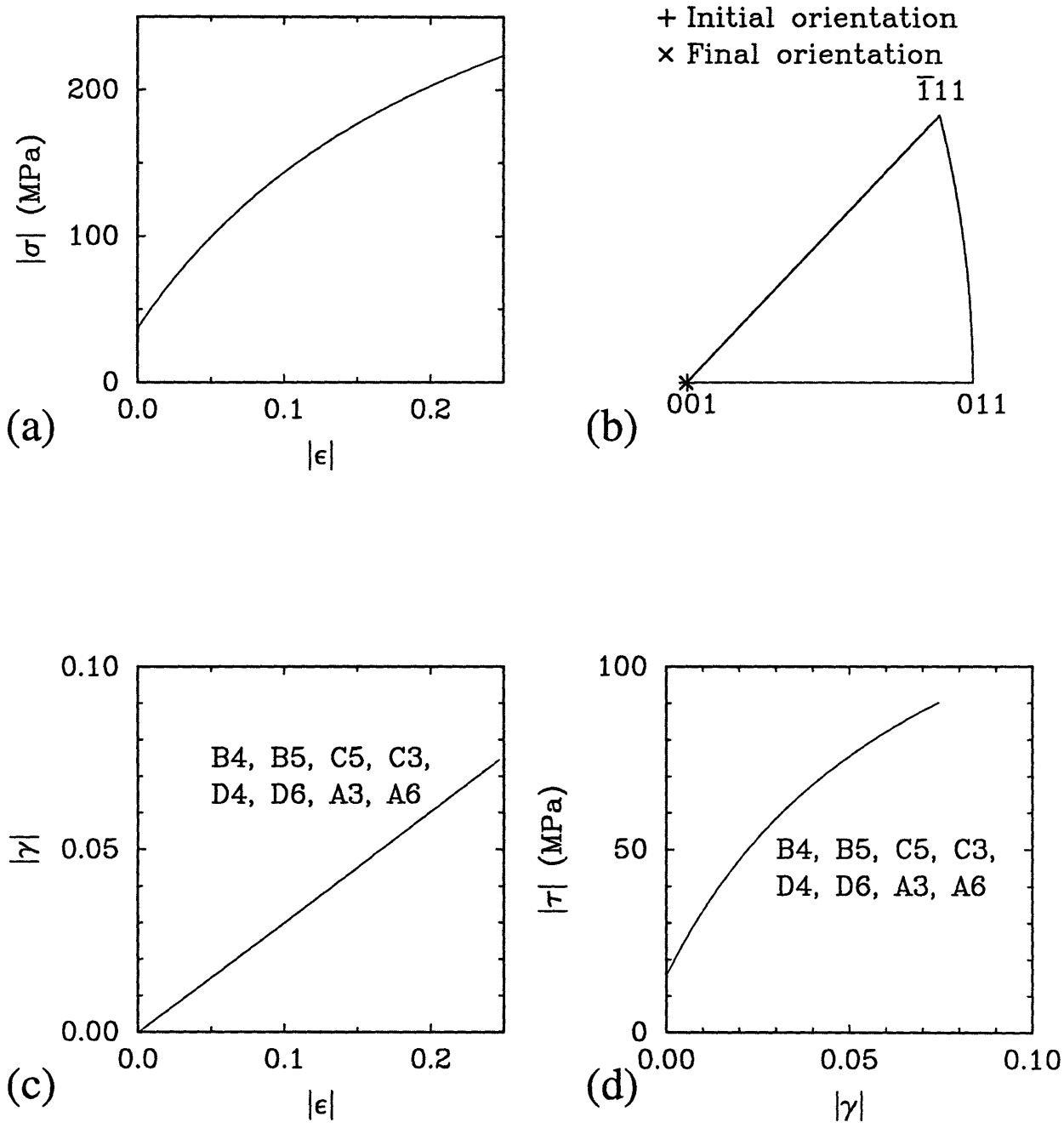

Figure 2-16: Simple tension of copper single crystal with the loading axis along the [001] direction, Kalidindi *et al* [1992] hardening: (a) The macroscopic stress-strain response (b) The evolution of the orientation of the loading axis (c) The accumulated slip vs. macroscopic strain for active slip systems (d) The shear stress-shear strain response on active slip systems

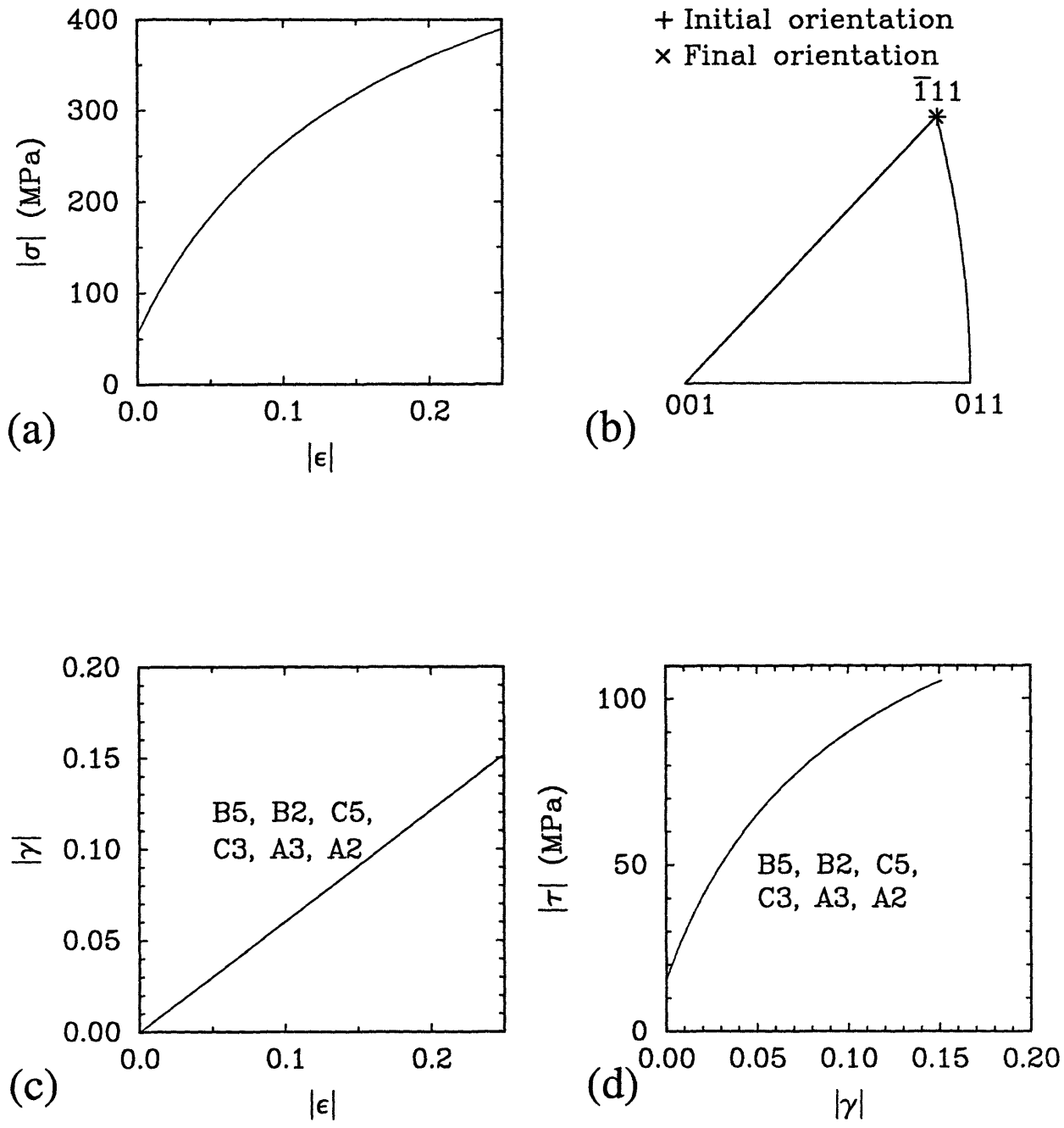

Figure 2-17: Simple tension of copper single crystal with the loading axis along the [$\bar{1}$11] direction, Kalidindi *et al* [1992] hardening: (a) The macroscopic stress-strain response (b) The evolution of the orientation of the loading axis (c) The accumulated slip vs. macroscopic strain for active slip systems (d) The shear stress-shear strain response on active slip systems

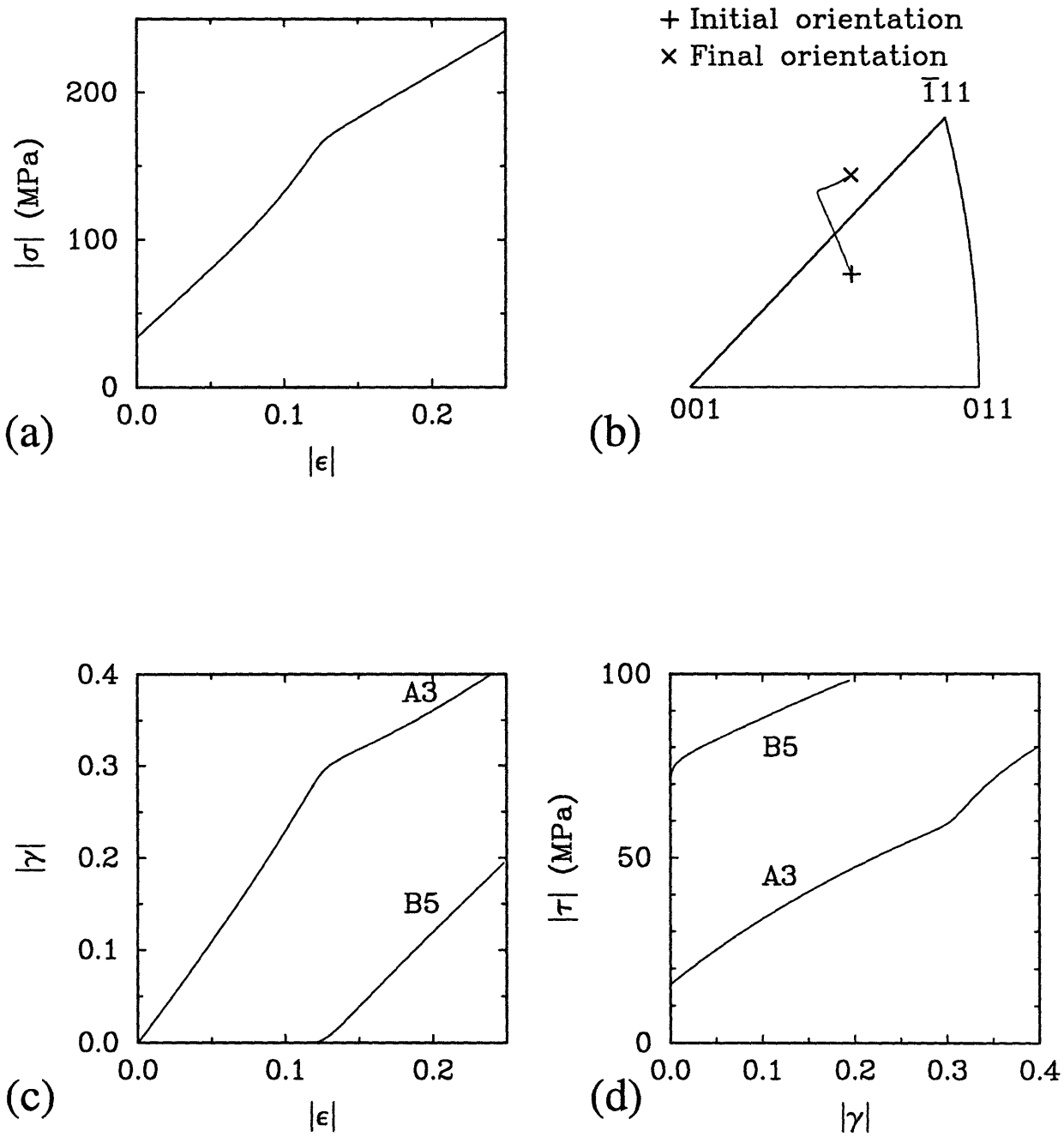

Figure 2-18: Simple tension of copper single crystal with the loading axis along the [$\bar{2}36$] direction, Kalidindi *et al* [1992] hardening: (a) The macroscopic stress-strain response (b) The evolution of the orientation of the loading axis (c) The accumulated slip vs. macroscopic strain for active slip systems (d) The shear stress-shear strain response on active slip systems

Chapter 3

Polycrystalline plasticity

In the previous chapter, the differences in the predictions of the Bassani *et al* hardening form and the Kalidindi *et al* form for single crystals were studied. In this chapter, the model is extended to polycrystalline plasticity invoking the Taylor assumption. The predictions of both the forms for simple compression with regards to the stress-strain response and the texture evolution are investigated. Finally, the predictions of the model for high temperature polycrystal deformations are presented and compared against experimental results.

3.1 Constitutive Equations for a Polycrystal

The Taylor assumption [Asaro and Needleman, 1985] is invoked to evaluate the response of a polycrystal. A polycrystal is considered to be an aggregate of single crystals. Local deformation in each grain $\mathbf{F}^{(k)}$, $k = 1, N$ is homogeneous and is the same as the macroscopic deformation gradient $\mathbf{F}$.

The macroscopic stress at a material point is the volume-averaged stress over all the grains constituting the material point,

$$\bar{\mathbf{T}} = \sum_{k=1}^{N} v_k \mathbf{T}^{(k)} \tag{3.1}$$

where $\mathbf{T}^{(k)}$ is the Cauchy stress in the k^{th} grain and $v^{(k)}$ is the volume fraction of the

k^{th} grain. When all grains are assumed to be of equal volume, the stress $\bar{\mathbf{T}}$ is just the number average over all the grains.

The texture at each material point at any instant of time τ comprises of the orientations of the lattice $\{\mathbf{m}^{\alpha}(\tau)^{(k)}, \mathbf{n}^{\alpha}(\tau)^{(k)}\}$ of the individual grains at the material point.

3.2 Simple Compression of a Polycrystal

In this section, simple compression of annealed polycrystalline copper is considered. The numerical simulations are carried out for both the hardening forms based on the single crystal data obtained in the last chapter. In these simulations, the simple compression experiments are approximated by the following isochoric motion with repect to a fixed rectangular Catesian coordinate system with origin $\mathbf{o}$ and orthonormal base vectors $\{\mathbf{e}_i \mid i = 1, 2, 3\}$:

$$\mathbf{x} = \exp\{-\frac{1}{2}\dot{\epsilon}t\}\, p_1\mathbf{e}_1 + \exp\{-\frac{1}{2}\dot{\epsilon}t\}\, p_2\mathbf{e}_2 + \exp\{\dot{\epsilon}t\}\, p_3\mathbf{e}_3 \tag{3.2}$$

with $\dot{\epsilon} = -0.001\text{sec}^{-1}$. The response from the Taylor-model to the isochoric motion is the volume-averaged stress behavior $\mathbf{T}' = \mathbf{T} + p\mathbf{1}$. Since the pressure is indeterminate, it is determined from the boundary conditions, namely, the lateral tractions are zero. The axial Cauchy stress is thus,

$$\sigma = T_{33} = T_{33}{}' - p \tag{3.3}$$

where $p = \frac{1}{2}(T_{11}{}' + T_{22}{}')$

The initial isotropic texture is represented numerically by 400 random grains (see Figure 3-1). The macroscopic response obtained from the simulations is compared with the experiments of Kalidindi [1992] in Figure 3-2. Both the hardening forms predict the polycrystalline response poorly. This is due to the neglect of the effects of grain-grain interaction and grain size that come into play in polycrystals. The Bassani *et al* form shows linear hardening even in polycrystals. This emphasizes the

need to take into account the stage III hardening which their model does not. On the other hand, the Kalidindi *et al* form shows saturation in the stress at large strains which is in qualitative agreement with the experiment.

An interesting observation is that the textures at large compressive strain obtained from the two hardening forms are different. Figure 3-3 shows the texture obtained from the Bassani *et al* hardening compared with the experimental texture at ϵ = -0.99. The prediction is not very accurate – the calculated texture is diffuse[1]. On the other hand, though the texture obtained from the Kalidindi *et al* hardening (see Figure 3-4) is sharper than the measured texture, it is in closer agreement with the latter. The poorer prediction of the evolution of texture using the Bassani *et al* form can be attributed to the linear hardening response shown by their form. But, this can be ascertained only by studying the texture predictions of the Bassani [1993] form which includes the effects of stage III hardening. Such a task has not been undetaken in this study.

The results based on the single crystal data imply that the polycrystalline response cannot be inferred from the single crystal response using either hardening forms. Either the hardening forms would have to be modified or the hardening parameters need to be altered to take into account the additional features of grain-size, grain-grain interaction etc. Owing to the simpler nature of the Kalidindi *et al* form and also due to its better prediction of evolution of texture, it is retained in preference to the Bassani *et al* form. However, the hardening parameters are altered to fit the polycrystalline response as done previously by [Kalidindi *et al.*, 1992] and [Bronkhorst *et al.*, 1992]. Figure 3-5 shows a fit using this form to a strain-rate jump test. The hardening parameters obtained from this fit are:

h_o = 190 MPa; s_o = 19 MPa; $\tilde{s}$ = 173 MPa

a = 2; n = 0; q_l = 1.4

The shearing rate parameters are the same as those for the single crystal:

$\dot{\gamma}_o = 10^6 \text{sec}^{-1}$; F_o = 4.7536x10^{-19} J; $p = q = 1$

The prediction of the stress-strain response using the new set of hardening

[1]this is an interesting fact since Taylor model is known to give sharp textures

parameters (see Figure 3-6) is reasonable.

3.3 Polycrystalline plasticity at elevated temperatures

The prime objective of a rate and temperature dependent form for the shearing on slip systems is to allow for a good predictive capability for a wide range of temperatures. In order to test the same, in this section, homogeneous and non-homogeneous deformations at moderately high temperature are discussed. The primary interest is in the prediction of the texture evolution and the load.

All the experiments here were performed by Kalidindi [1992] on annealed 1100-type aluminum which has an fcc crystal structure. The experiments were done at a temperature of 250°C which is about 0.56 times the absolute melting temperature of Al1100. This temperature is low enough to assume that plastic deformation occurs primarily by crystallographic slip and high enough to observe a significant rate sensitivity of plastic flow.

The initial texture is quite random as shown in the {111} and {110} pole figures in Figure 3-7(a). The initial texture is represented by a set of 100 grain orientations Figure 3-7(b). The next task is to evaluate the material parameters required for a Taylor-type model.

The elastic constants for Aluminum crystal at this temperature are:-

C_{11} = 97 GPa; C_{12} = 58 GPa; C_{44} = 24 GPa [Simmons and Wang, 1971]

The slip hardening and shearing rate parameters are obtained from fitting the stress-strain response to strain-rate jump tests. The fits obtained are shown in Figure 3-8. The material parameters for Al1100 at 250°C obtained through the fit are[2]:-

$\dot{\gamma}_o = 10^6 \text{sec}^{-1}$; F_o = 2.3 x 10^{-19} J;

h_o = 150 MPa; s_o = 25 MPa; $\tilde{s}$ = 44 M a = 2.1; n = 0.004; q_l = 1.4

[2]An approximate value for F_o comes from $F_o \approx \alpha\mu b^3$. For Aluminum at 250°C, μ = 222.365 GPa; b = 2.86 x 10^{-10} m $\Rightarrow \mu b^3$ = 5.232 x 10^{-19} J. Here, $\alpha \approx 0.4$

The predicted stress-strain curves using these parameters for simple compression at three different values of constant true strain rates with the Taylor-type model on 100 crystals is shown in Figure 3-9. The predicitions are fairly accurate demonstrating the accuracy of the model for high temperatures. Figure 3-10 shows the comparison of the numerically calculated and experimentally measured textures for a constant true strain rate of -0.001 sec^{-1} at a true compressive strain of ϵ = -1.0. The two agree qualitatively. An interesting observation is that the model captures the diffuse nature of the texture (Figure 3-10). This is a consequence of the increase in activity in the slip systems at elevated temperatures. The {110} pole figure does not show a 'hole' at the center as seen previously in copper (recall Figure 3-4). This implies that the accuracy of the Taylor model improves with increase in temperature due to the accompanied increase in the rate-sensitivity.

3.4 Non-homogeneous deformation

Following the line of study presented by Kalidindi [1992], in this section, the comparisons of the experimental results and numerical calculations for a simple non-homogeneous, non-steady, axi-symmetric forging on annealed Al1100 at 250°C are presented.

The schematic of the axi-symmetric forging experiment done by Kalidindi [1992] is shown in Figure 3-11(a). The part of the plunger that is in contact with the specimen has a slight depression to hold the top of the specimen. The dies were ground smooth and well-lubricated.

Figure 3-11(b) shows the finite element mesh for the simulation. Each element in the mesh is an eight-noded reduced integration, axi-symmetric element (CAX8R). The interface between the top of the specimen and the depression in the plunger is modeled by restricting the motion of the nodes on the interface in the radial direction. All other interfaces were modeled as frictionless.

The material parameters used in the simulation are those previously obtained from fitting the stress-strain response for simple compression. The calculations are

based on a Taylor-model with 100 crystals at each integration point.

Figure 3-15 shows the comparison of the calculated load-displacement curve with the experimental results. The prediction is reasonably accurate. The experimental and simulated {111} and {110} pole figures at three representative material point are compared in Figures 3-12 - 3-14. Figure 3-14 shows that a material point near the axis of the specimen has essentially undergone a simple compression as seen from the similarity of Figures 3-14(a) to the compression texture Figure 3-10. The prediction for the other two material points which undergo more complex deformation history are in good agreement with the experiments.

The discussion above demonstrates the capability of the rate and temperature dependent model to predict loads and texture evolution for homogeneous and non-homogeneous processes at elevated temperature fairly accurately.

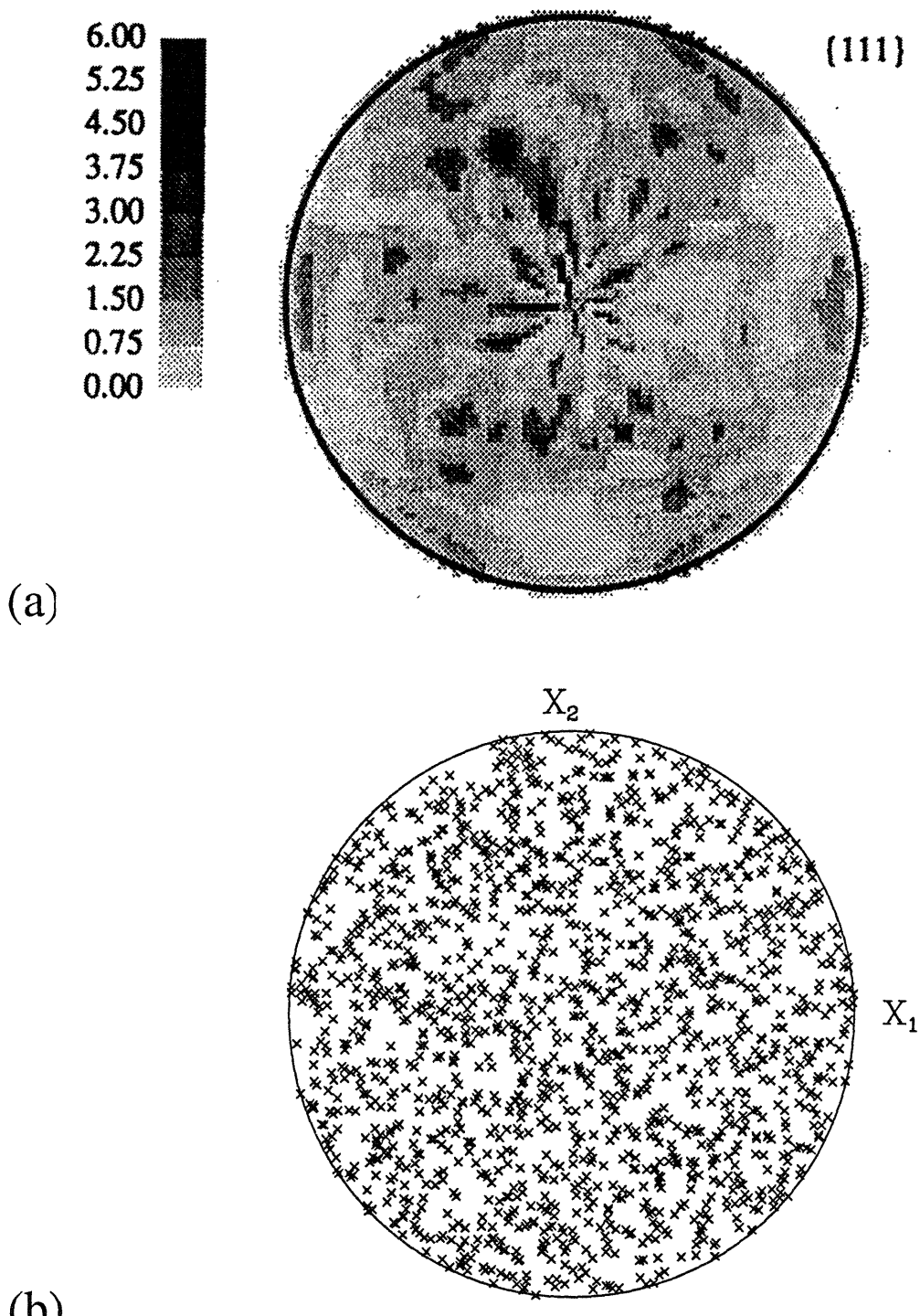

Figure 3-1: (a) Experimentally measured isotropic texture on annealed OFHC copper [Kalidindi, 1992] (b) Numerical representation by 400 crystals

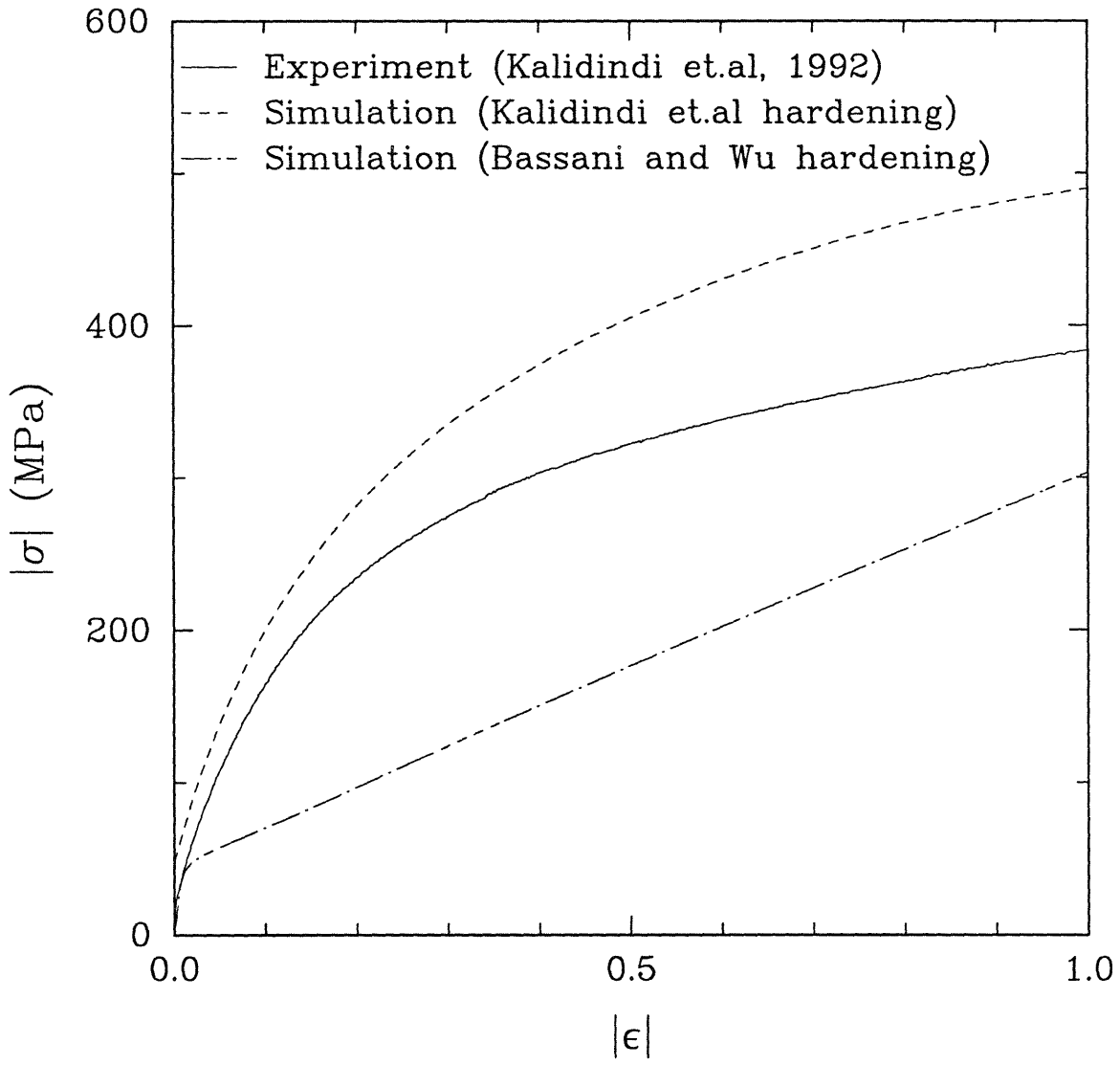

Figure 3-2: Simple compression of polycrystalline copper based on single crystal data and comparison with experiment

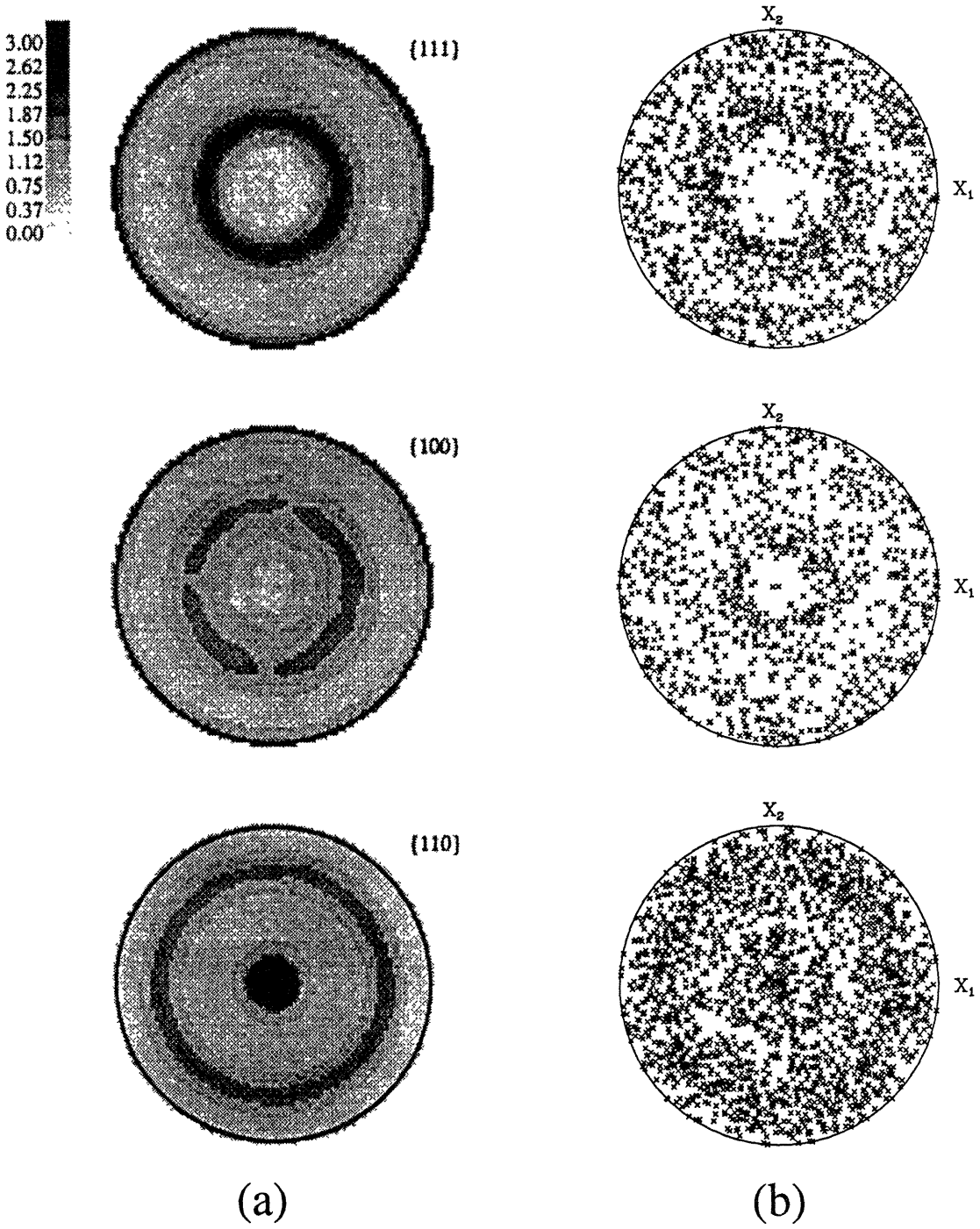

Figure 3-3: Simple compression of OFHC copper at room temperature [Kalidindi, 1992]: (a) Experimentally measured texture at ϵ = -1.0 (b) Numerical simulation on 400 crystals (Bassani *et al* hardening)

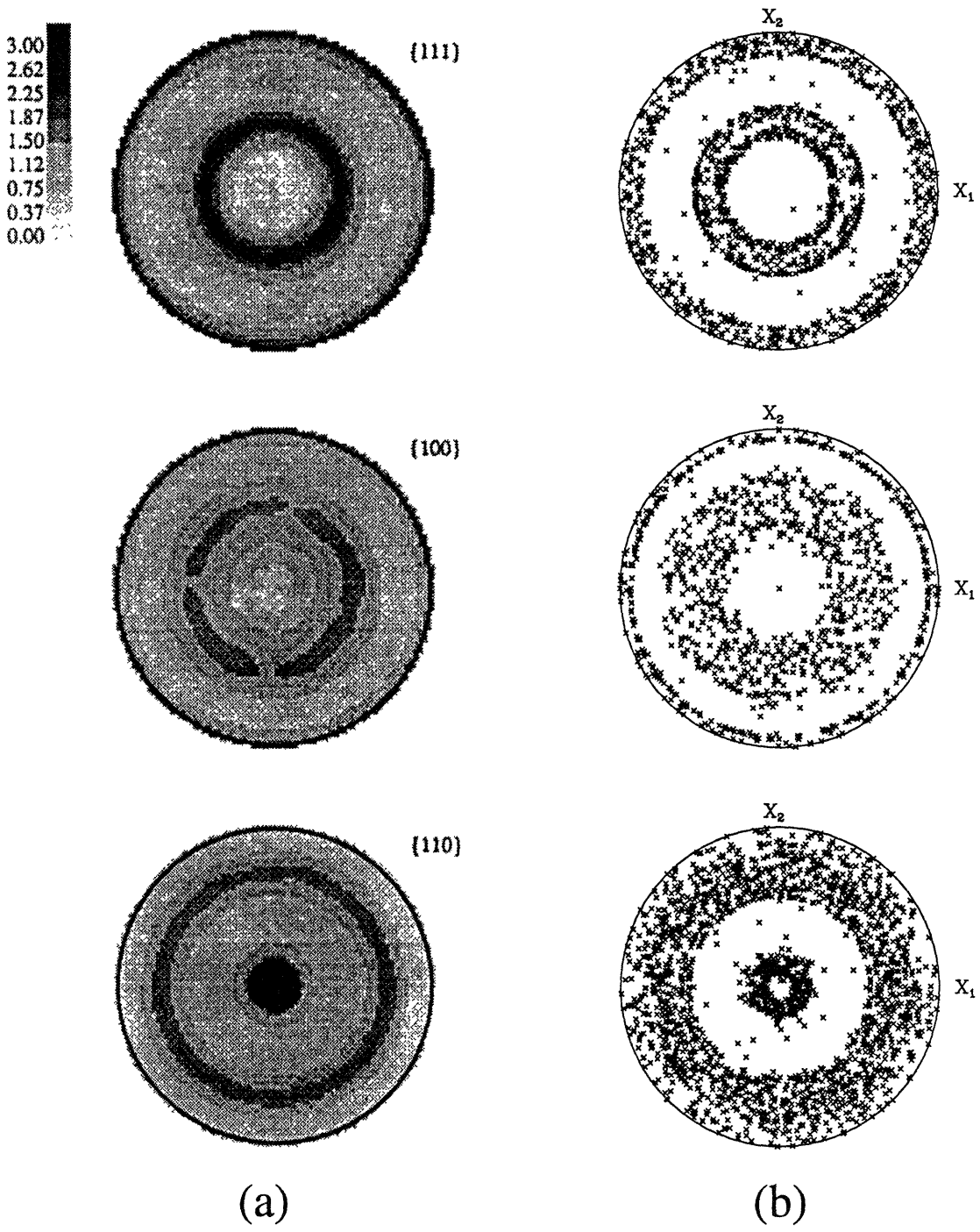

Figure 3-4: Simple compression of OFHC copper at room temperature [Kalidindi, 1992]: (a) Experimentally measured texture at ϵ = -1.0 (b) Numerical simulation on 400 crystals (Kaldindi *et al* hardening)

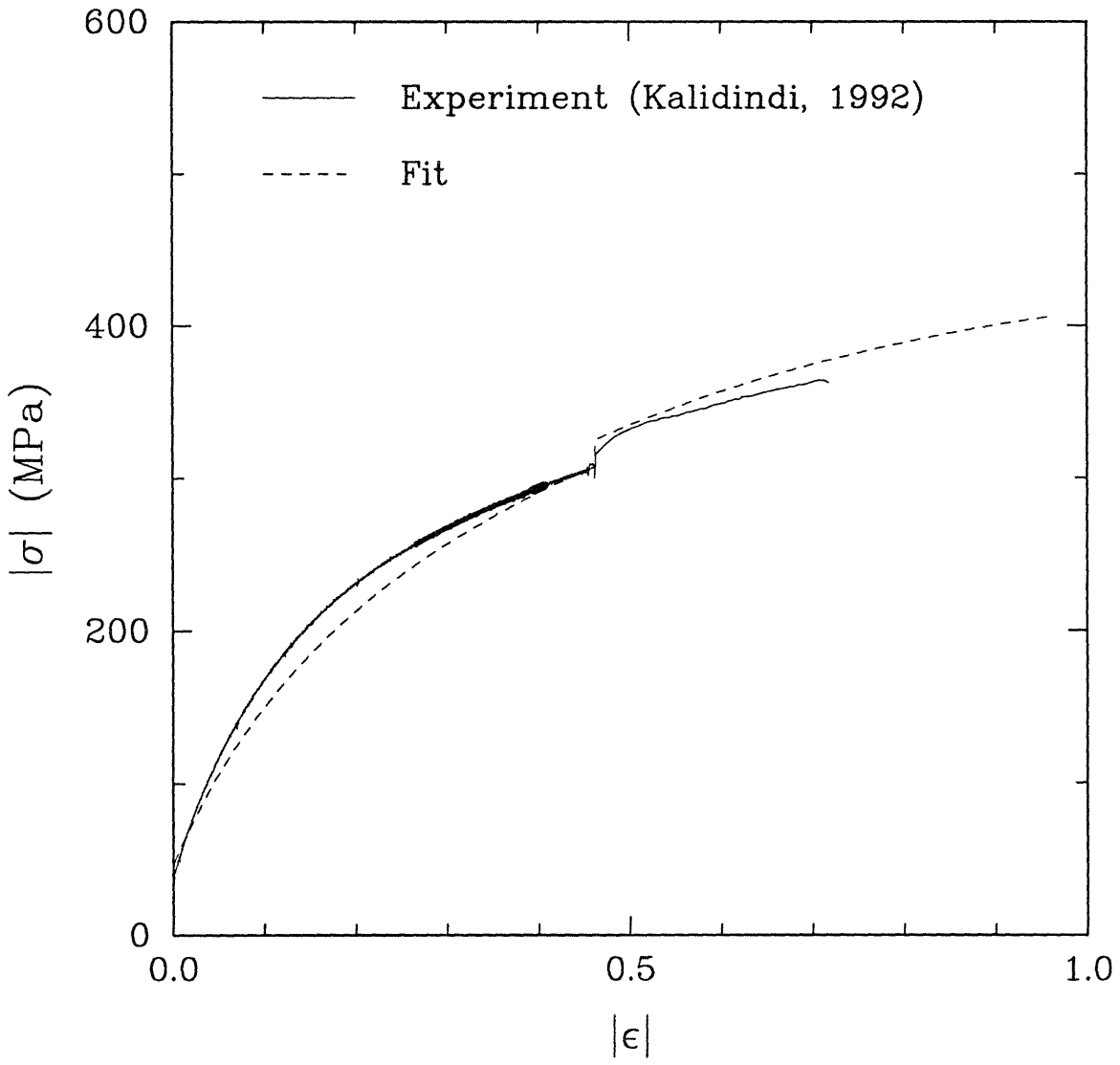

Figure 3-5: Simple compression of polycrystalline copper: Fit to strain rate jump experiments (Kalidindi *et al* hardening)

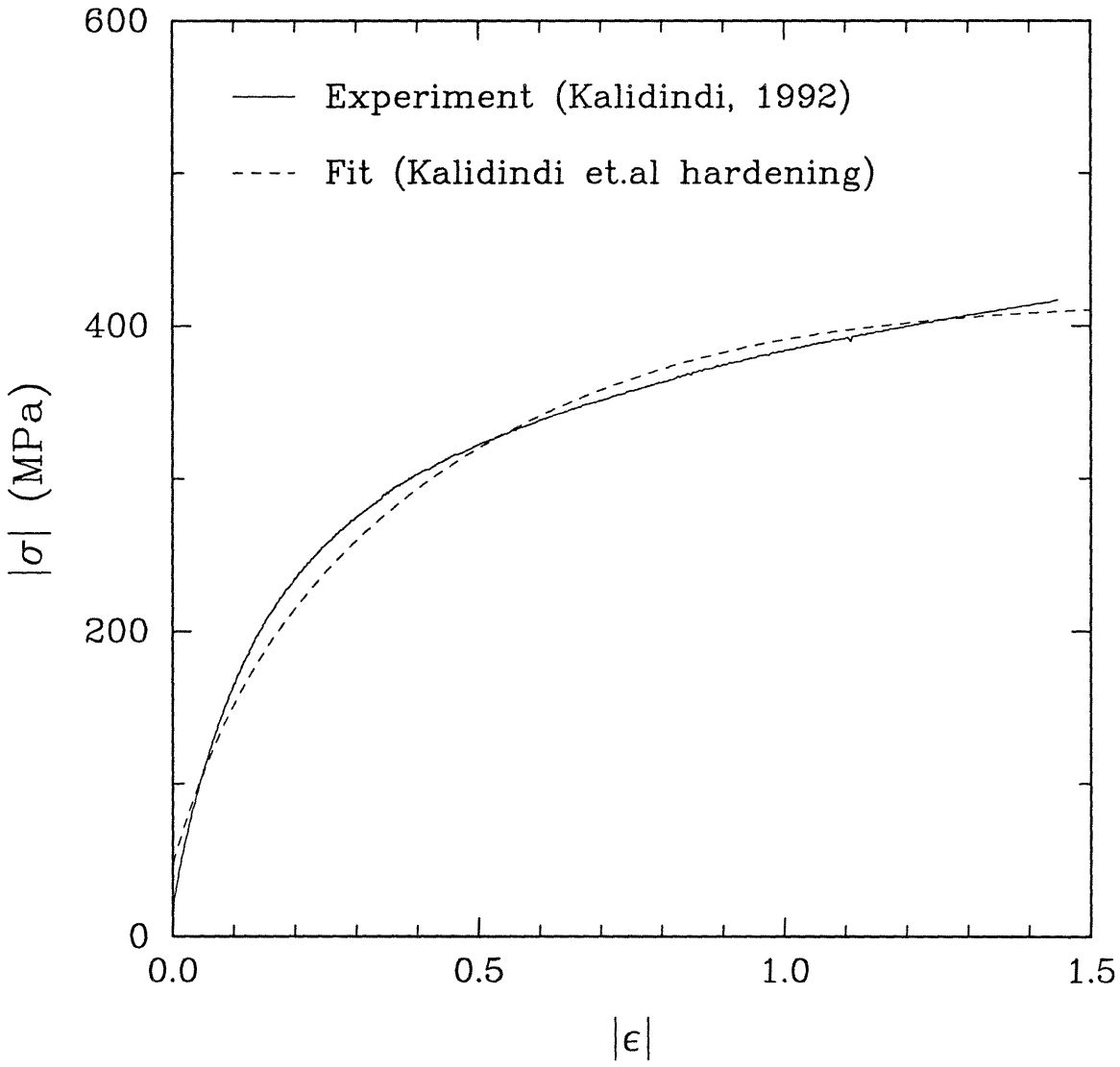

Figure 3-6: Simple compression of polycrystalline copper based on parameters from fit to strain rate jump experiments (Kalidindi *et al* hardening)

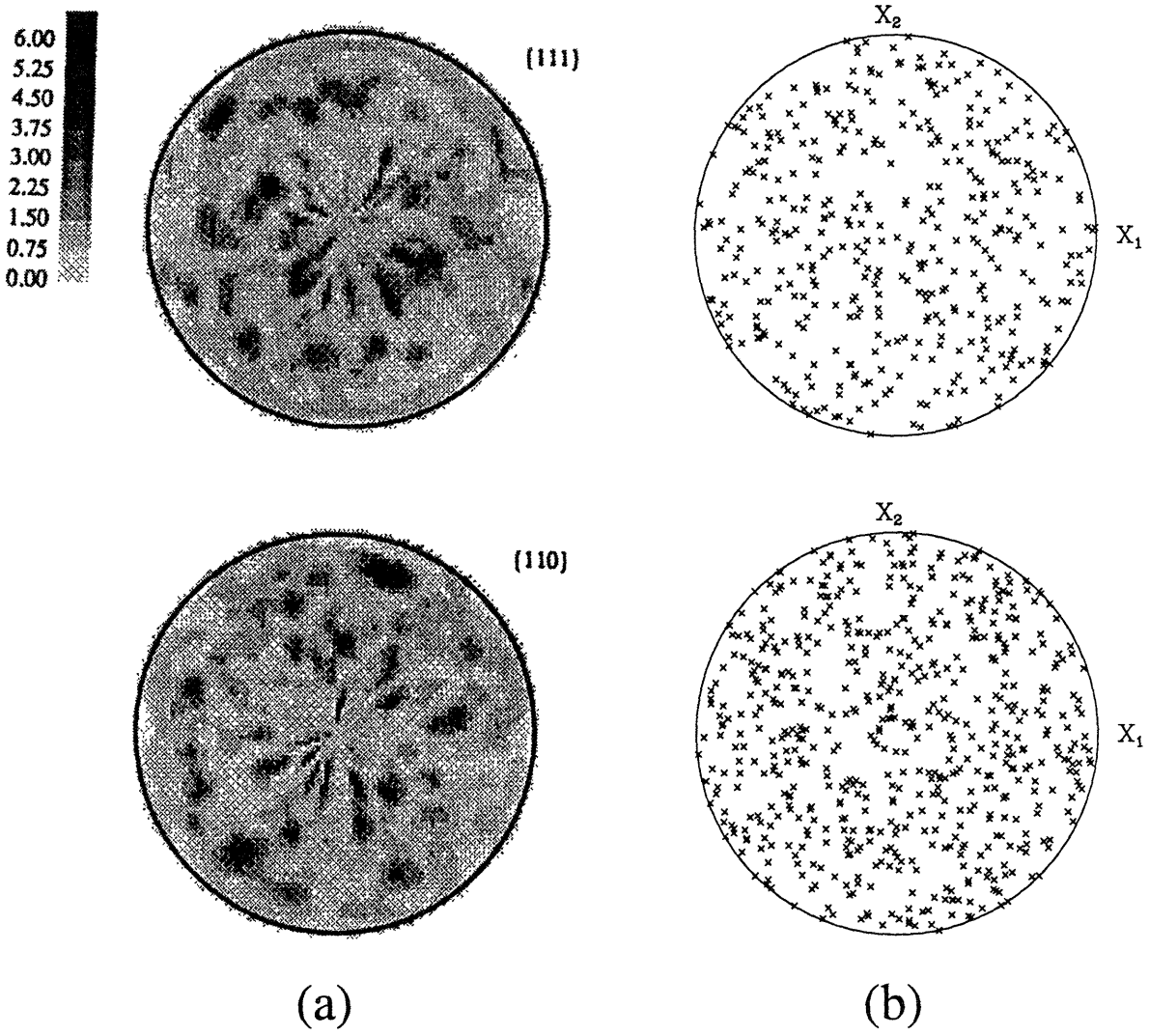

Figure 3-7: (a) Experimentally measured isotropic texture on annealed Al1100 [Kalidindi, 1992] (b) Numerical representation by 100 crystals

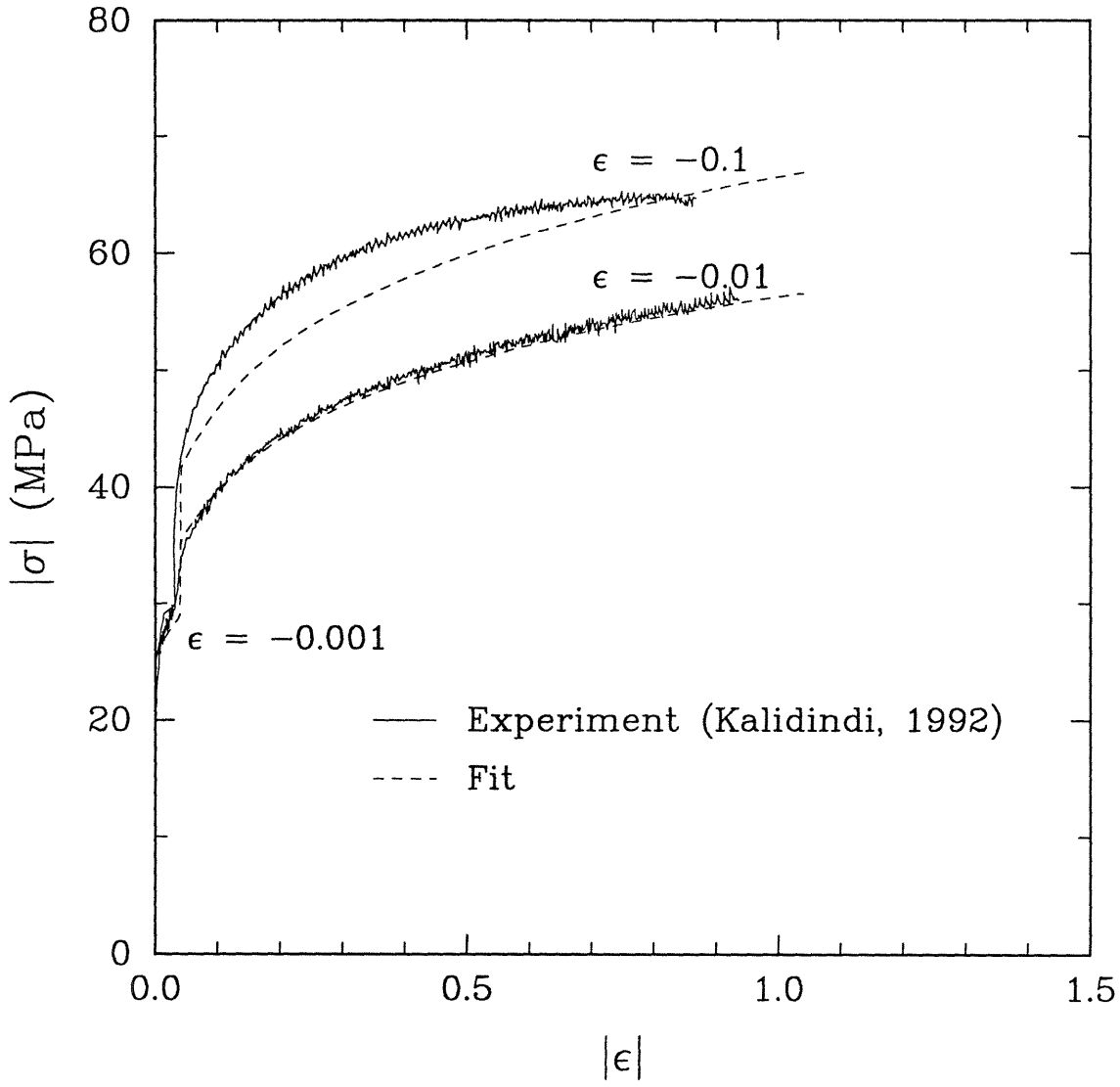

Figure 3-8: Simple compression of Al1100 at 250°C: Fit to strain rate jump experiments (Kalidindi *et al* hardening)

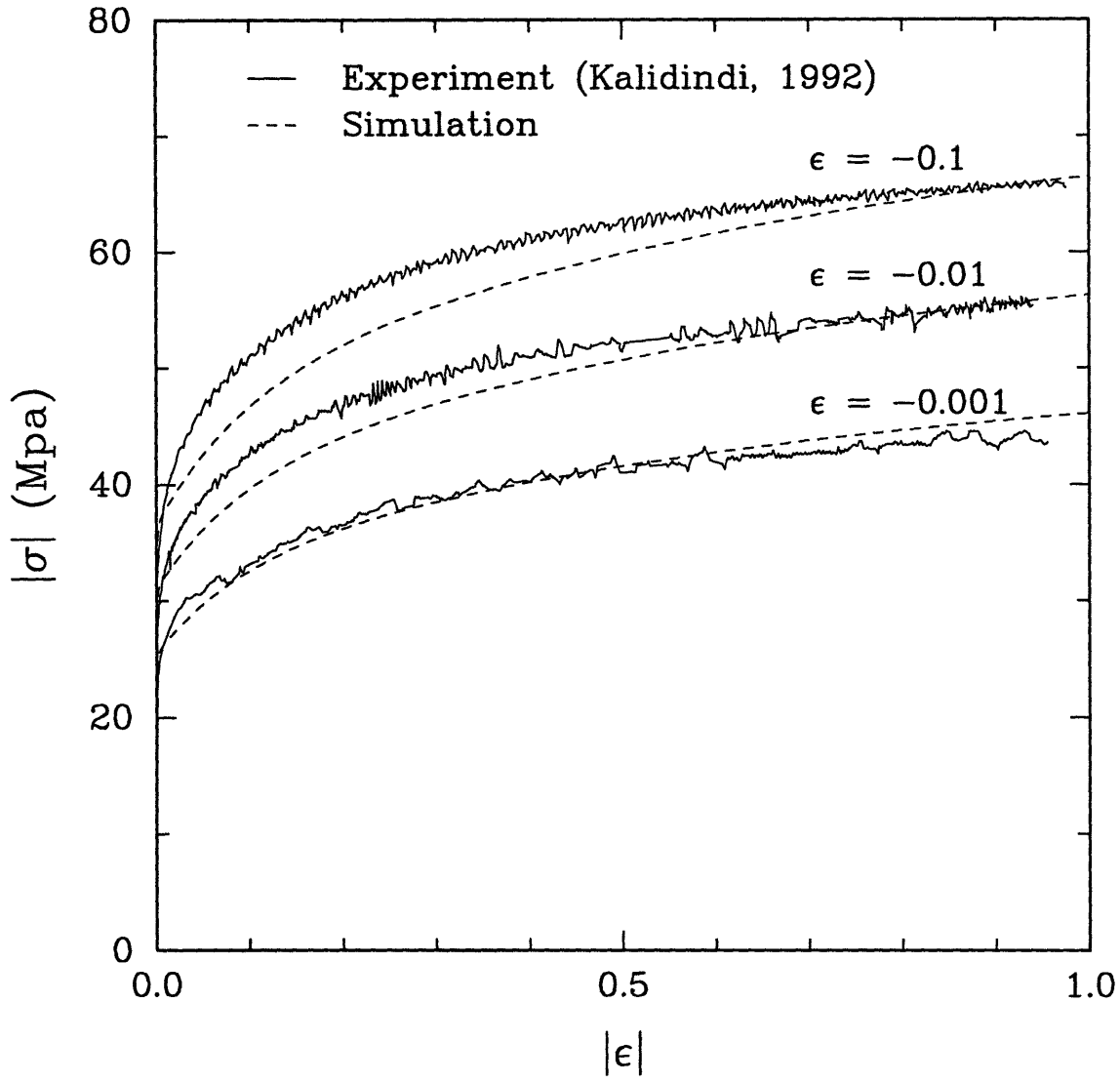

Figure 3-9: Simple compression of Al1100 at 250°C: Prediction and comparison with experiments (Kalidindi *et al* hardening)

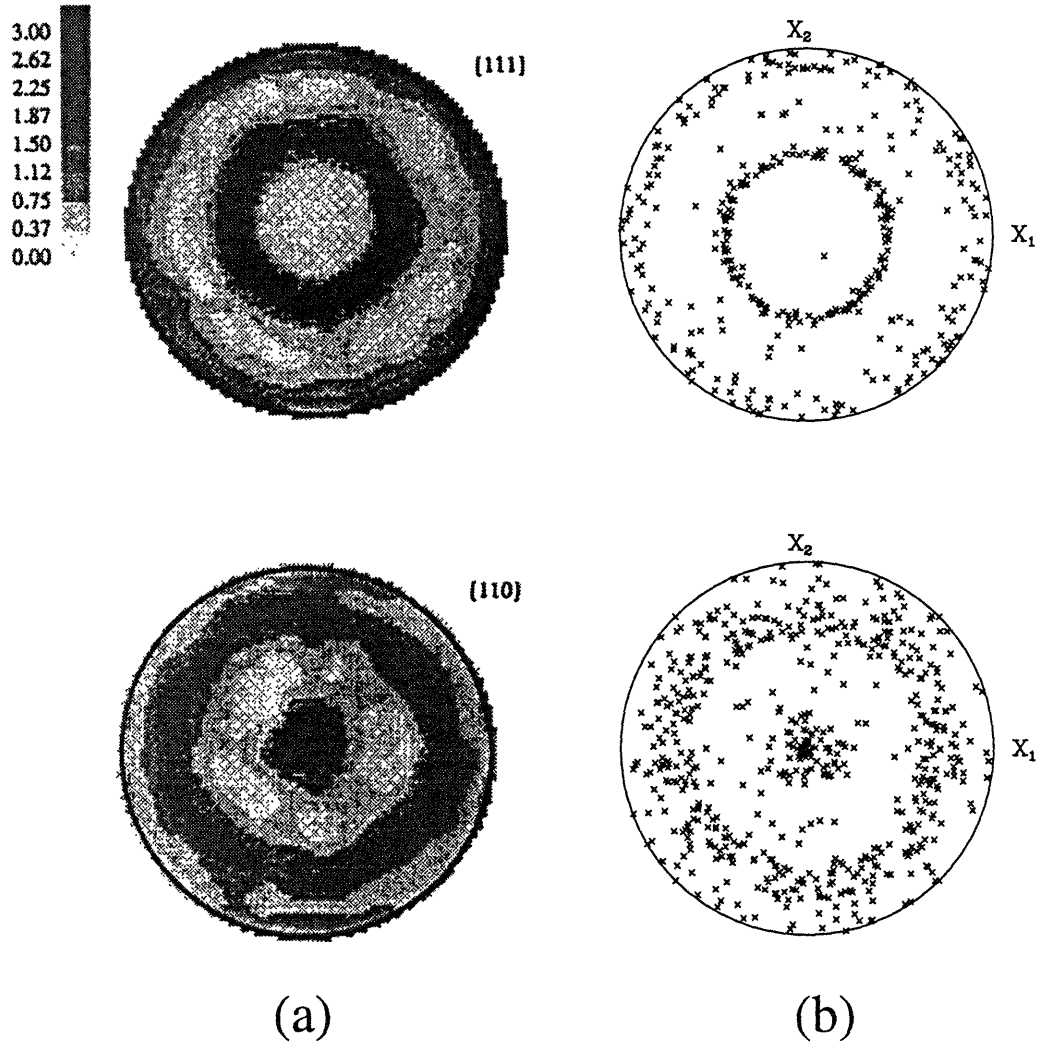

Figure 3-10: Simple compression of Al1100 at 250°C at a constant true strain rate of $\dot{\epsilon}$ = -0.001/sec [Kalidindi, 1992]: (a) Experimentally measured texture at ϵ = -1.0 (b) Numerical simulation on 100 crystals (Taylor type model)

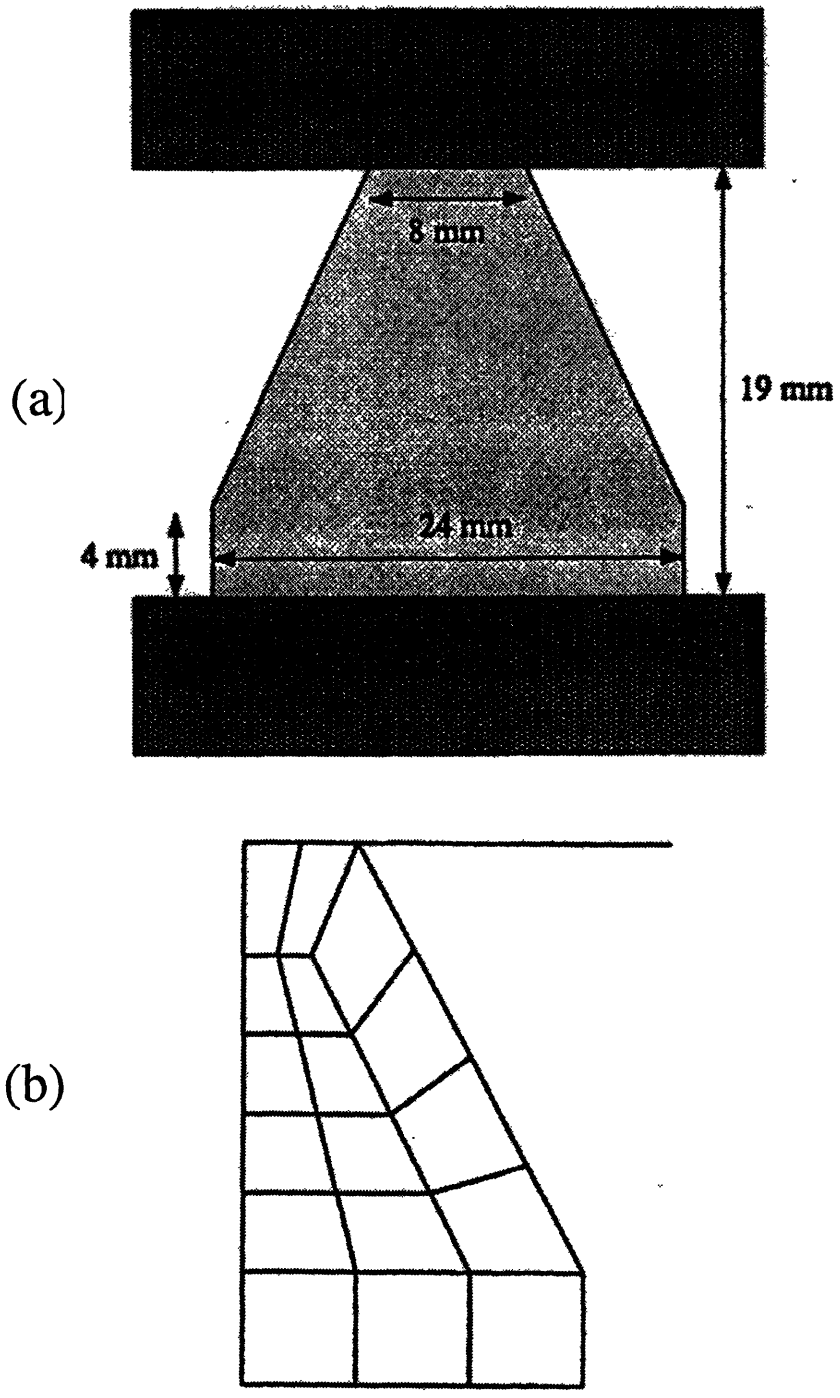

Figure 3-11: Axisymmetric forging of Al1100 at 250°C: (a) Schematic of the experiment (b) Finite element mesh used for the numerical simulation

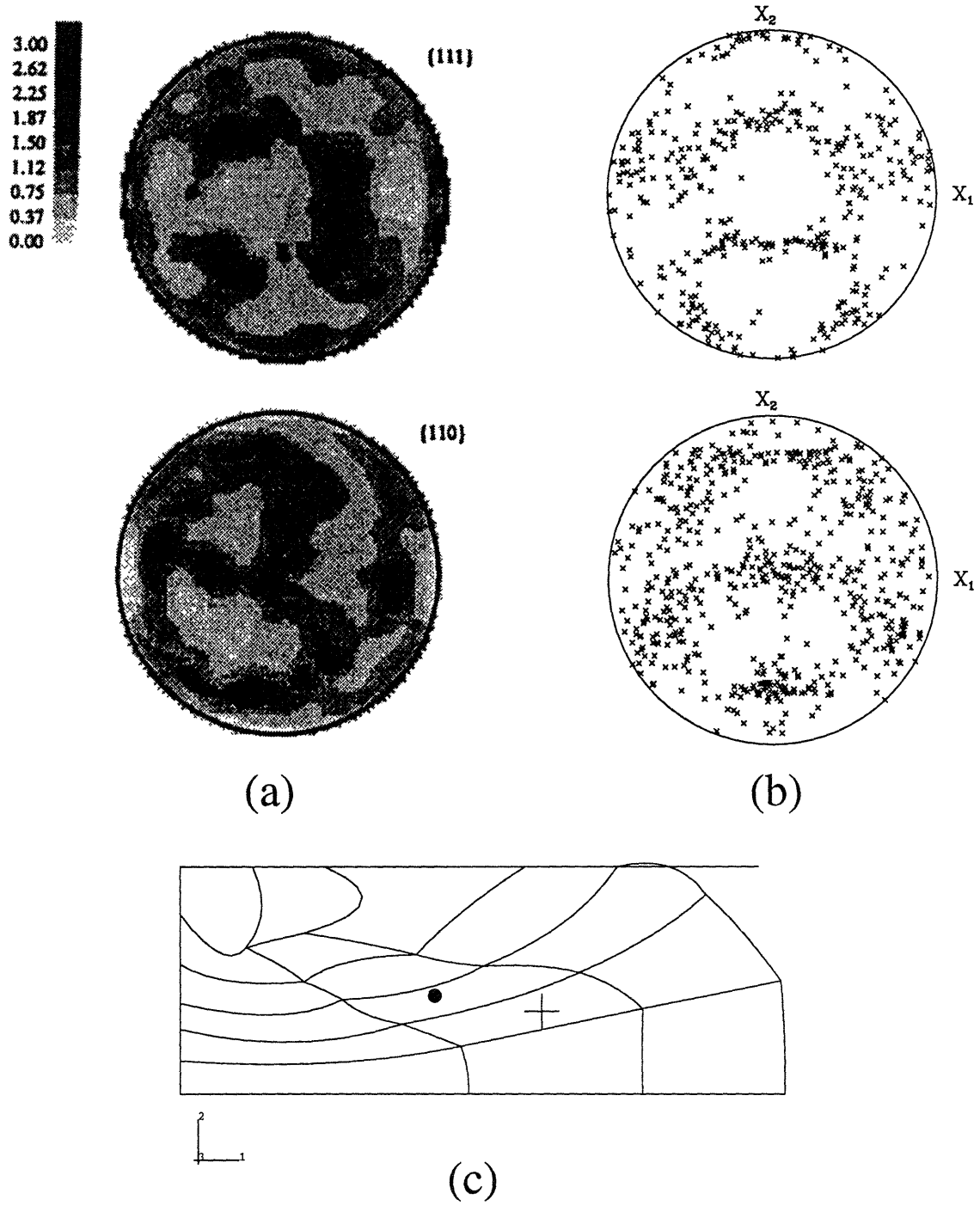

Figure 3-12: Axisymmetric forging of Al1100 at 250°C: (a) Experimentally measured texture from the deformed specimen (b) The corresponding numerical simulations (c) The deformed mesh and the point of texture measurement. $\bar{\epsilon}^p = 1.410$

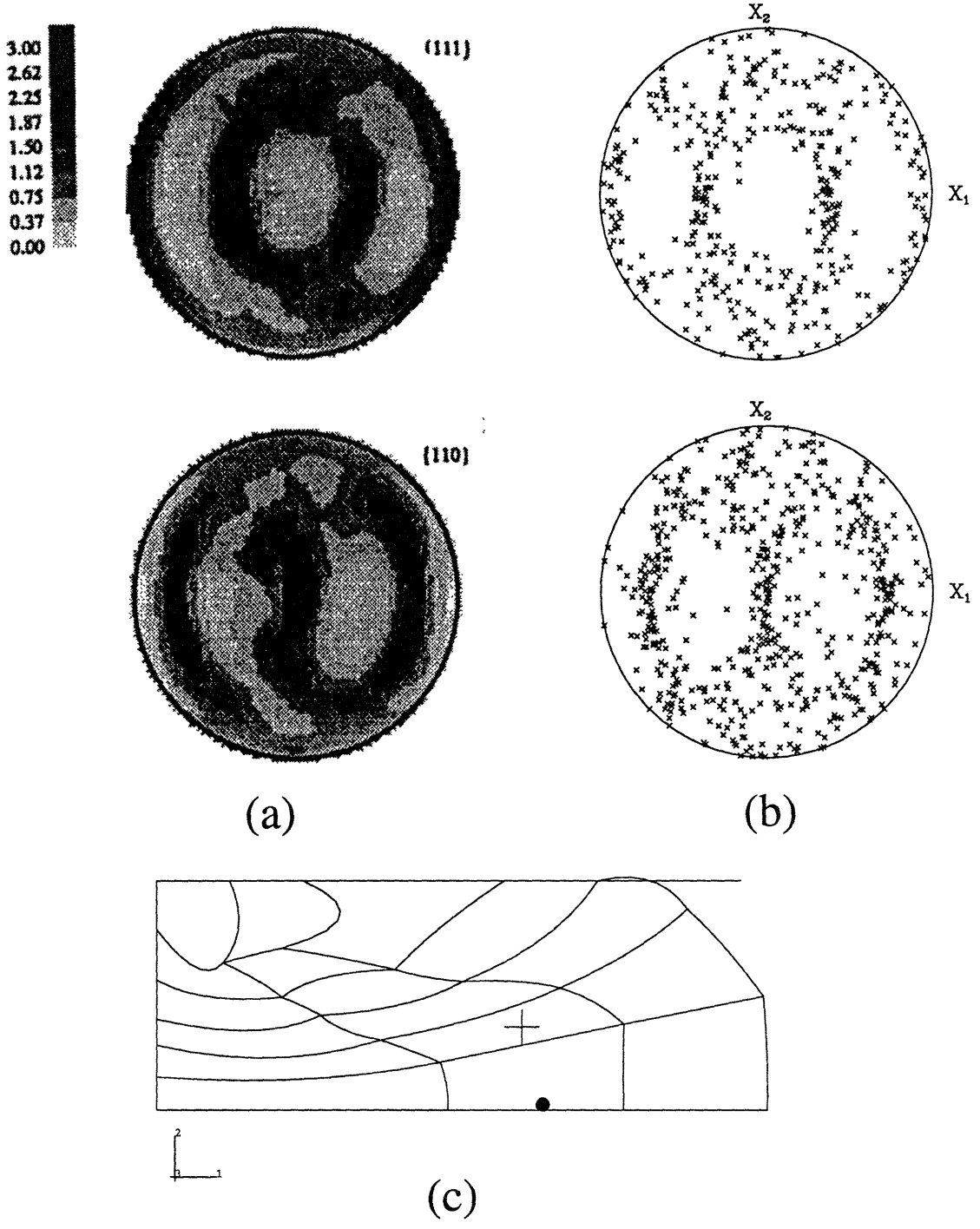

Figure 3-13: Axisymmetric forging of Al1100 at 250°C: (a) Experimentally measured texture from the deformed specimen (b) The corresponding numerical simulations (c) The deformed mesh and the point of texture measurement. $\bar{\epsilon^p} = 0.6442$

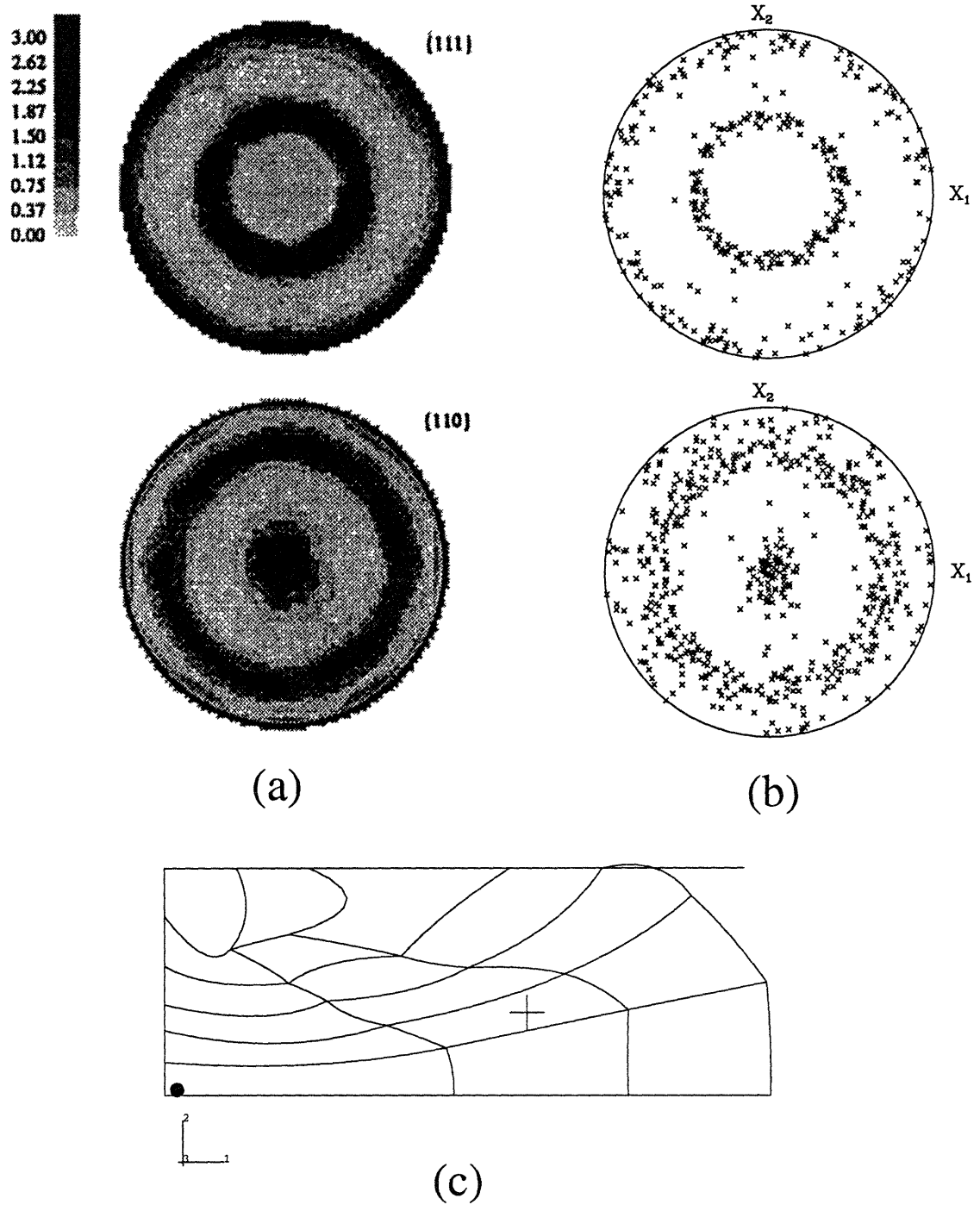

Figure 3-14: Axisymmetric forging of Al1100 at 250°C: (a) Experimentally measured texture from the deformed specimen (b) The corresponding numerical simulations (c) The deformed mesh and the point of texture measurement. $\bar{\epsilon^p} = 1.647$

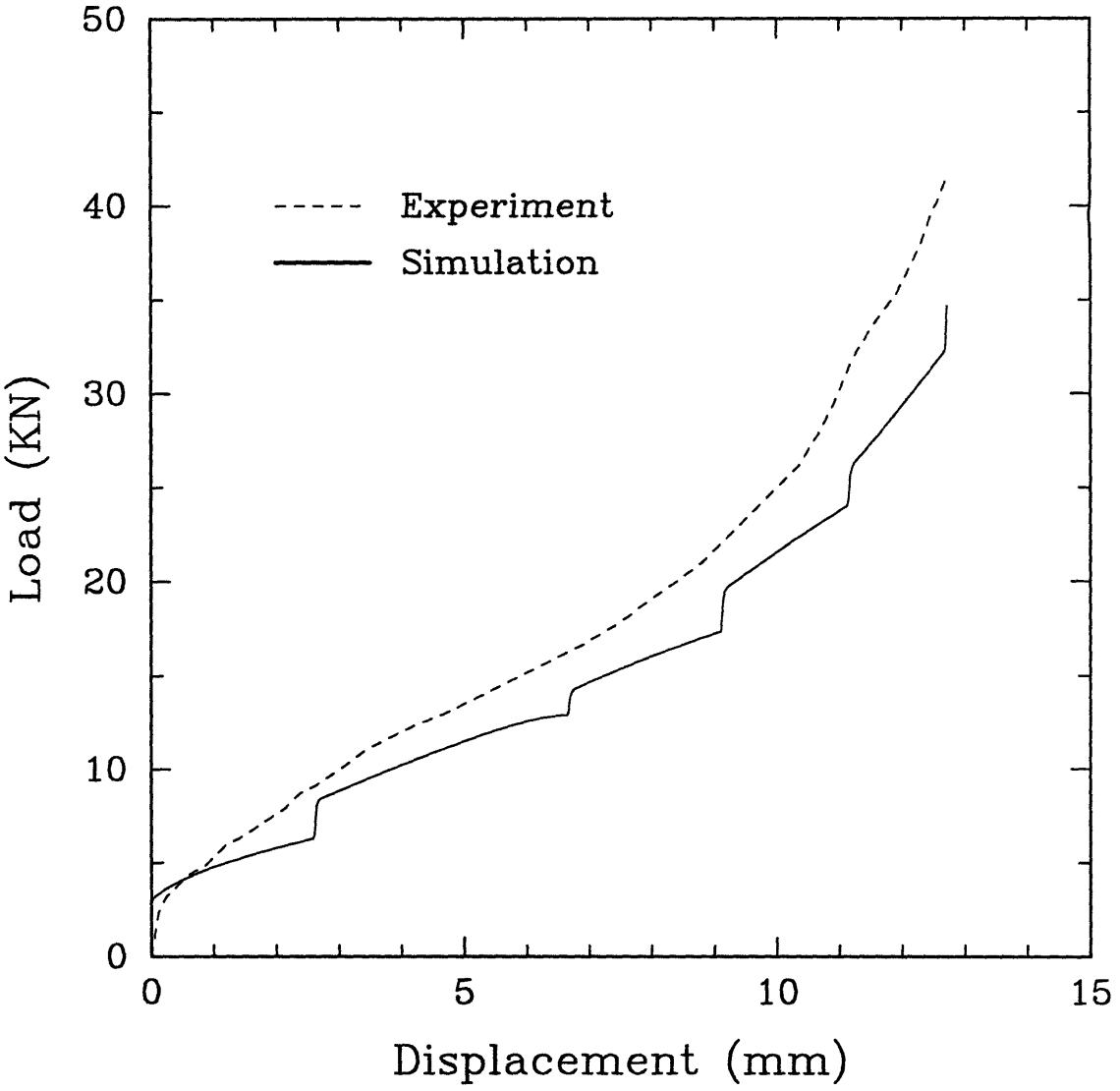

Figure 3-15: Axisymmetric forging of Al1100 at 250°C: Experimental and predicted load-displacement curves

Chapter 4

Applications to deformation processing

In the previous chapters, a rate and temperature dependent crystal plasticity model was proposed and its predictions for simple deformations in single crystals and polycrystals were studied. Since the primary objective of this study is to build a capability to model and design deformation processing, in this chapter, the applicability of the model to actual industrial forming operations is investigated. For this purpose, the earing of single crystals and polycrystals in deep-drawing operation is examined.

The solution of large problems with complicated tooling can be computationally very intensive, making the choice of a suitable computational procedure very important. Hence, at first, a little discussion on the computational procedures available and their advantages and disadvantages are presented. Later, the predictive capabilities of the model in the earing of single crystals in two different orientations and a polycrystal are studied.

4.1 Implicit vs. Explicit procedure

Implicit procedures for solving boundary value problems, with implicit integration schemes like Euler-backward method, permit large increments in time due to the

unconditional nature of these integration schemes. The accuracy, stability and speed of such procedures in solving complex bulk-forming processes has been amply demonstrated by Kalidindi *et al.* [1992], Weber *et al.* [1989]. However, the time required to solve a problem cannot be estimated apriori, since the time incrementation usually varies markedly during the course of the analysis due to the iterative nature of the solver. The analysis time is roughly proportional to the square of the size of the problem, the latter can be estimated from the number of finite elements used ([Nagtegaal and Taylor, 1992]). This poses a severe constraint in solving large problems or in resolving finer details like localization phenomena etc. An additional drawback stems from evaluating changes in contact conditions between the work and the tool which demands that the number of contact changes during an increment be small. The foregoing considerations emphasize the need for explicit schemes to solve large, complex problems involving complicated tooling. Since even a few dozen finite elements with a hundred grains at each material point could make the solution procedure computationally intensive, our model would profit substantially from its implementation in an explicit solver. In addition, the contact conditions between deforming bodies are easier to satisfy. The gains in speed are complemented by the added capabilities to solve dynamic problems e.g., high rate forming processes like explosive forming etc.

The disadvantage in any explicit scheme is that the time increments are bounded from above by stability requirements. The stability limit for an explicit operator can be given in terms of the highest eigenvalue λ_{max} in the system of ODE's e.g., for an Euler-forward operator,

$$\Delta t \leq \frac{2}{\lambda_{max}} \tag{4.1}$$

An approximate estimate of the stability limit can be obtained from evaluating the

time required for a dilatational wave to cross the most critical finite element [1] as

$$\Delta t \approx \frac{L}{c_d} \tag{4.2}$$

where L is the characteristic critical element dimension and c_d is the dilatational wave speed of the material given as $c_d = \sqrt{\frac{C_{12}+2C_{44}}{\rho}}$ (ABAQUS [1993]) where C_{12} and C_{44} are elastic constants[2] and ρ is the density of the material i.e., the time increment must be small enough so as to ensure that a perturbation does not propagate through more than one element in that interval. A recommended way (ABAQUS [1993]) of surmounting this obstacle is to decrease the time period of the process by increasing the rate of the process. Due to the rate-dependent nature of the model, adopting such a procedure would alter the response. Hence, an alternative method would require an artificial increase in the density of the material, thereby, decreasing the wave speed and increasing the stability limit. The increase in density is, however, limited by the requirement that the inertial effects be small. A good estimate for the latter has been found in this study to be a small ratio of the kinetic energy to the internal energy (approximately $0.01 - 0.05$).

The constitutive equations would also impose stability restrictions on the time step. Usually, the restrictions imposed by the wave speed of the material are more severe than these. However, it has been found in this study that the stability limit imposed by the constitutive model becomes more critical near the rate-independent limit owing to the stiff nature of the constitutive equations in this case. The task of apriori-estimation of the stability limit for the constitutive equations is a formidable one due to their non-linear nature.

In the present study, the problem of estimating the stability limit for the constitutive equations has been overcome by using an iterative Newton-Raphson method at the constitutive level to evaluate the stresses $\mathbf{T}^*$ and s^α in each crystal (see Appendix A). This has been found to allow for larger time increments obtained

[1] Critical element is the one which has the smallest characteristic dimension. Different elements may become critical at different times as the deformation progresses

[2] For an isotropic material, $C_{44} = \frac{1}{2}(C_{11} - C_{12}) = \mu$

through appropriate changes in density at the global level.

In the current study both, the implicit and the explicit schemes have been used wherever appropriate. The implicit schemes were found to be efficient in simple deformations. The simple tension, compression and axi-symmetric forging were done using the implicit scheme. The deep-drawing problem has been studied using the explicit scheme through a user-material subroutine VUMAT in ABAQUS 5.3. The explicit procedure exploits the vectorization capabilities in modern workstations so as to gain efficiency. Also, the boundary conditions were found easy to impose in the explicit procedure.

4.2 Earing in the deep-drawing of fcc single crystals

The development of ears in the deep-drawing of sheets is known to be due to the planar anisotropy of the sheet. Since the anisotropy is the most severe in single crystals, the earing in single crystals is worth studying . The motivation comes from the pioneering work of Tucker [1961] who performed extensive experiments to study the earing patterns of deep-drawn single crystal cups of Aluminum in different orientations. Figure 4-1(a) shows the fully-drawn cups arranged in the standard stereographic triangle. It can be seen that there is a wide variety in the number of ears and their position and heights. There has been a lot of effort in the recent years to numerically simulate the earing in single crystals and predict the positions and heights of the ears. Barlat [1991b] have incorporated the material anisotropy through an anisotropic yield surface. This enables them to capture the earing phenomenon, but the model does not capture the effects of the evolving texture on the deformation. Becker [1993] have incorporated the latter through a crystallographic texture model and have shown that their predictions are in good agreeement with the experiments done by Tucker. Their model is based on a simple power law hardening on each slip system. Also, they neglect effects due to latent hardening. In this section, we

investigate the predictions of our crystal plasticity model of the earing behavior for two corner orientations [3], namely, [001] and [111]. The choice is based on the different earing patterns observed in these orientations (see Figures 4-1(b) and (c))

The geometry of the cup-drawing apparatus (Figure 4-2(a)) assumed for the simulations is the same as the one used by Tucker for his experiments. Circular blanks of 0.81 mm thickness and 79 mm diameter are considered. The blank-material is OFHC copper. Recall, the material properties for the same obtained in Chapter 2:
$h_o = 300$ MPa; $s_o = 19$ MPa; $s_s = 215$ MPa; $a = 2.2$; $n = 0$; $q_l = 1.4$
$\dot{\gamma}_o = 10^6 \text{sec}^{-1}$; $F_o = 4.7536\text{x}10^{-19}$ J; $p = q = 1$

Figure 4-2(b) shows the finite element mesh used for the simulation. Note that as both orientations [001] and [111] possess rotational symmetries about the punch axis, only a sector of the circular blank need be considered for the analysis. The blank is meshed with C3D8R and C3D6 elements. The interfaces between the punch and the blank; the blank and the blankholder; the blank and the die are taken to be frictionless. The die, blankholder and the punch are treated as rigid surfaces. The blankholder is assumed to be clamped at a fixed distance from the die surface. This is different from the boundary condition in practice where a uniform pressure is maintained on the blankholder [Becker *et al.*, 1993]. But, the displacement boundary conditions were found to be easier to incorporate in the numerical simulations. Since the inplane-deformation of the sheet is of primary interest, only one element is taken through the thickness of the blank. The punch speed is taken to be 1 m sec^{-1}.

4.2.1 Drawing in the [001] orientation

This orientation has 4-fold symmetry about the punch axis permitting the use of a 45° sector of the blank. The 0° and 45° planes are symmetry planes and are free of shear traction.

Figure 4-3 shows a schematic of the earing pattern observed in fcc single crystals in this orientation. Four ears form at 0°, 90°, 180° and 270° along the [100], [010], [$\bar{1}$00]

[3]The orientations mentioned refer to the crystallographic direction that is normal to the blank and aligned with the punch-axis

and $[0\bar{1}0]$ respectively. This is clearly evident in Tucker's experiment (see Figure 4-1(b))

Figure 4-4 shows the final shape and the equivalent plastic strain contours on the fully drawn cup. For the sake of clarity, the entire cup has been shown. Figure 4-4 also shows the final shape of the Aluminum single crystal cup in this orientation (Tucker [1961]). The cup from the simulation has been rotated so that the view coincides with that of Tucker's photograph. It can be seen that the prediction of the number of ears and their position is accurate. No attempt has been made to compare the heights of the ears as the materials are different. The emphasis is only on the capability to predict the formation of ears. Figures 4-5(a) - (d) and 4-6(a) - (d) show the slip-system activity in the outermost row of elements[4]. The element located on the 2.8125^o plane has 4 active slip-systems, namely, D1, C1, B2, A2 (Figure 4-5(a)). The same slip-systems are active in the 8.4375^o and 14.0625^o planes (Figures 4-5(b), (c)). In the neighborhood of the $22\frac{1}{2}^o$ plane, 4 additional slip-systems D6, A3, B4, C5 become active(Figure 4-5(d), Figure 4-6(a)). Along the planes at angles higher than $22\frac{1}{2}^o$, slip-systems D6, A3, B4, C5 are the only ones showing significant activity (Figure 4-6(b) - (d)). These results are in agreement with Tucker's first-order predictions where he identified the slip-systems with maximum resolved shear stress based on the slip-system geometry. However, there are no strain discontinuities near the $22\frac{1}{2}^o$ plane in our predicitions owing to the operation of additional slip-systems. The activity is also not the same in all the active slip-systems due to the anisotropic nature of the hardening matrix. Based on slip-system geometry and assuming a diagonal form for the hardening matrix with parabolic hardening on each slip-system, Tucker showed that due to such a slip-system activity the radial strains are the maximum along the 0^o plane and minimum along the 45^o plane which explains the formation of ear on the 0^o plane and a trough along the 45^o plane. The material in the ears is not constrained laterally to the same extent as that immediately below the troughs, allowing material to flow laterally resulting in spreading. This results in higher accumulated plastic

[4]The planes under consideration are the radial planes that pass through the centers of the elements in the outermost row of elements

strain in the ears as seen in Figure 4-4.

4.2.2 Drawing in the [111] orientation

In this orientation, the punch-axis becomes an axis with 3-fold symmetry allowing the use of only a 60° sector of the circular blank for the analysis with symmetry boundary conditions imposed on either ends of the sector. Figure 4-7 shows a schematic of the earing pattern observed in this orientation. This is evident in Tucker's photograph reproduced in Figure 4-1(c).

Figure 4-8 shows the predicted final shape of the cup with equivalent plastic strain contours. It is compared with the results of Tucker. The number of ears, namely, six and their position are predicted accurately. Again, the accumulated plastic strain is the maximum in the ears.

4.3 Earing in the deep-drawing of fcc polycrystals

In industrial practice, cup-drawing operations are performed on polycrystalline material. As the blank is cut from a rolled sheet, its properties are not isotropic. The planar anisotropy results in the formation of ears during deep-drawing. Cold-rolled fcc metals are known to give ears at approximately 45° to the rolling direction (RD). Figure 4-10 shows a schematic of the earing of fcc polycrystals with initial rolling texture.

Here, the deep-drawing of polycrystalline OFHC copper is simulated. Recall, the material properties of the same are:-

$h_o = 190$ MPa; $s_o = 19$ MPa; $\tilde{s} = 173$ MPa;

a = 2; n = 0; $q_l = 1.4$;

$\dot{\gamma}_o = 10^6 \text{sec}^{-1}$; $F_o = 2.06\text{x}10^{-19}$ J; $p = q = 1$

It is to be noted that in order to alleviate the numerical difficulties in the rate-independent limit, the rate-sensitivity has been increased slightly through a decrease in F_o. However, we do not expect this to affect the qualitative aspects of the results.

The initial rolling texture is approximated by the plane-strain compression

texture. In sheet rolling, the strains related to the increase in the width of the material in the transverse direction (TD) are small compared to those due to the thickness reduction in the normal direction (ND) and the elongation in the rolling direction (RD). Hence, the plane-strain assumption is a reasonable one. The initial texture is obtained by carrying out a plane-strain compression simulation on a polycrystal of 400 initially random grains to a strain of $\epsilon = -1.0$. The resulting texture is represented by a weighted[5] average over 21 components using popLA [Kallend *et al.*, 1991].

Figure 4-11 shows the cup with fully-developed ears and its comparison with the experiments by Wilson and Butler [1961] on polycrystalline copper with initial rolling texture. The position and number of ears are accurately predicted. However, the severity of the earing is overpredicted due to the representation of the initial texture by a few ideal components. Becker *et al* [1993] have shown that an assumption that most of the volume fraction of grains contribute to random components is more in agreement with the experimental results. A quantitative comparison is meaningful only when the initial texture is properly characterized.

In conclusion, the study has established a capability to predict the formation of earing defects in deep-drawing. The same capability can be used for finding a feasible approach to reduce earing. It is clearly evident that the initial texture of the sheet plays a dominant role in the formation of ears. Figure 4-12 shows the effect of initial texture on the final shape of the cup. It shows that the presence of cube texture and rolling texture in balanced amounts reduces the severity of ears. Hence, the issue is to design the deformation processing scheme to get a desirable texture for the sheet. The task is a challenging one as the cube texture is known to be unstable in rolling [Rollett *et al.*, 1987].

[5] A weighted representation has been found to be reasonably good and saves a lot of computational effort

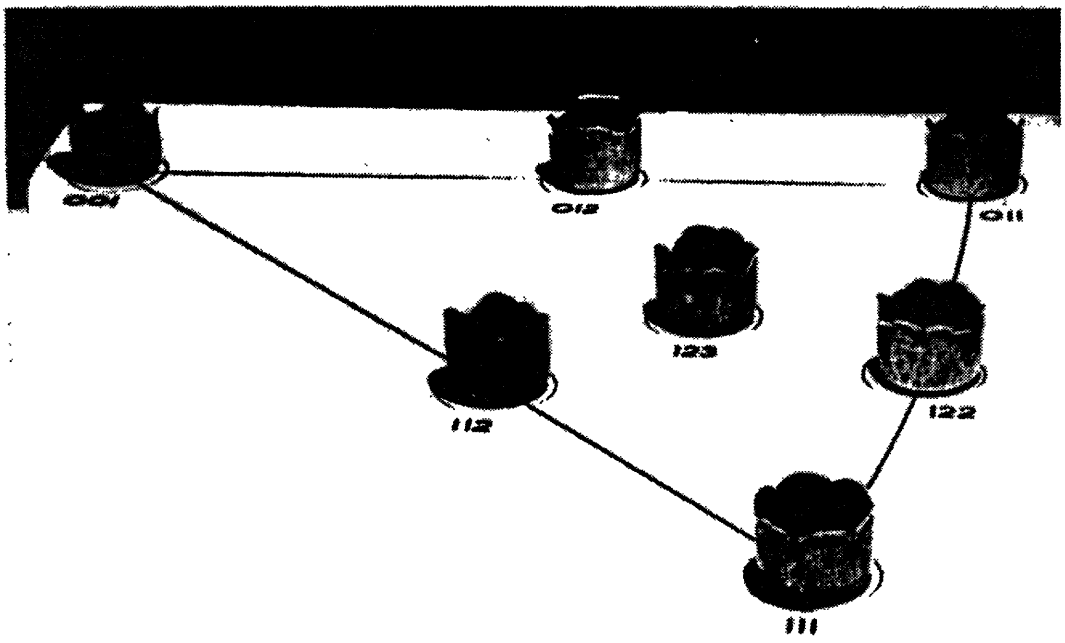

(a)

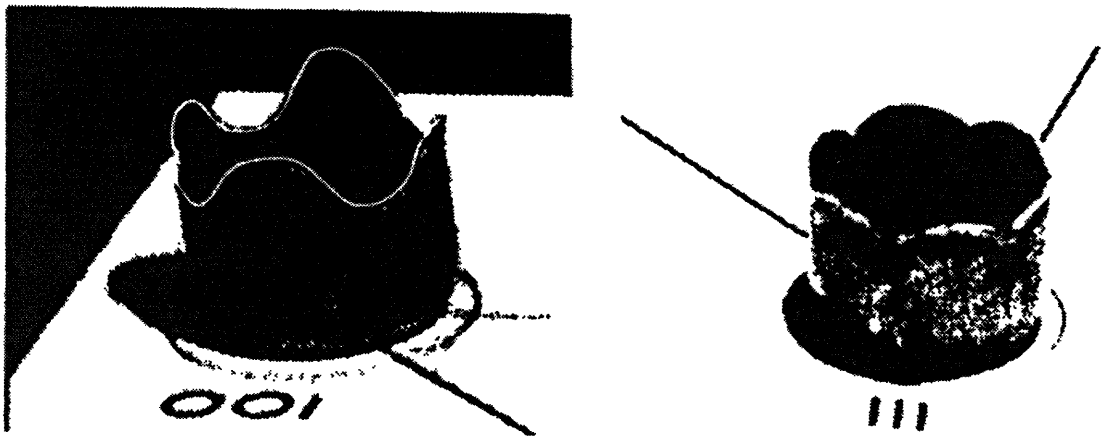

(b) (c)

Figure 4-1: (a) Deep-drawn cups from single crystals of pure aluminum arranged on stereographic projection of unit triangle [Tucker, 1961] (b) Drawn cup with the [001] direction along the punch axis (c) Drawn cup with the [111] direction along the punch axis

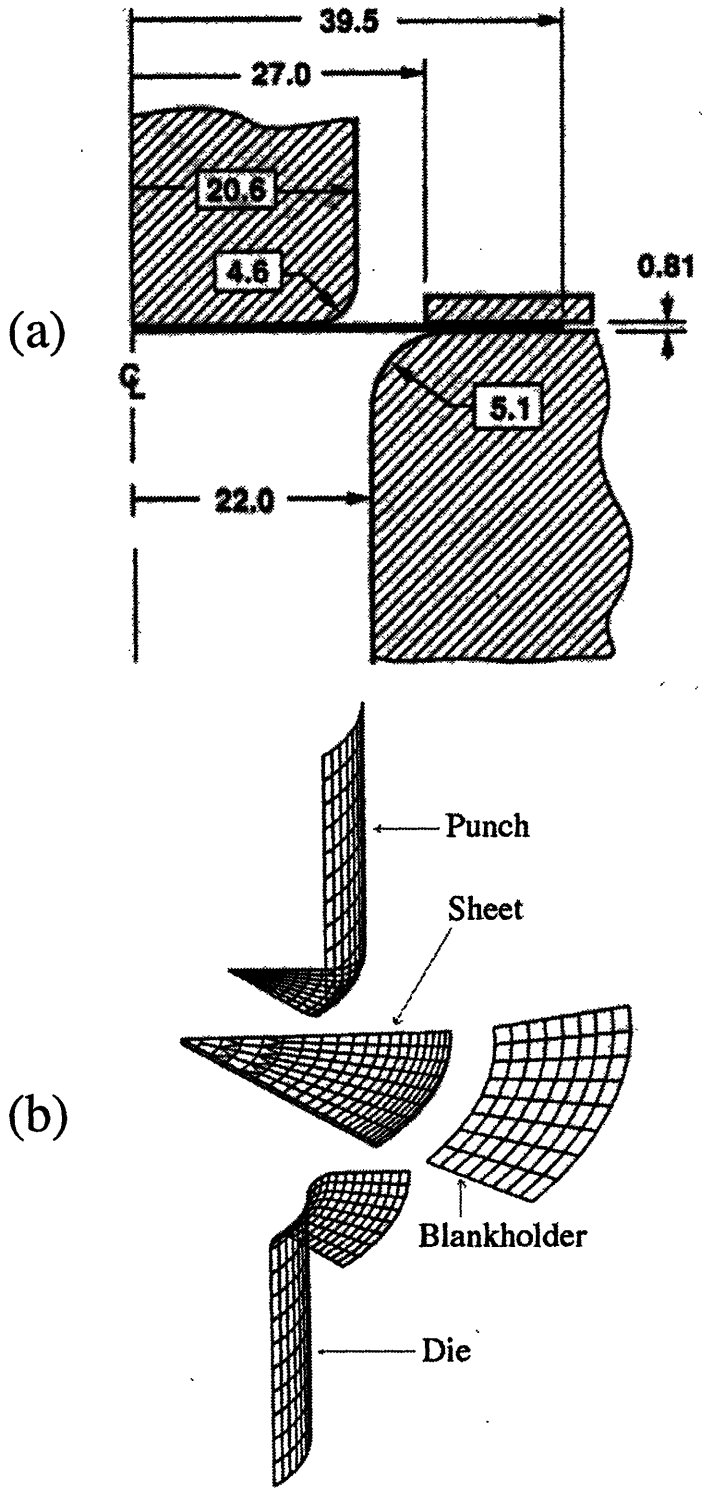

Figure 4-2: (a) Geometry for the single crystal drawing simulations [based on experiments done by Tucker, 1961] (b) Exploded view of the finite element mesh

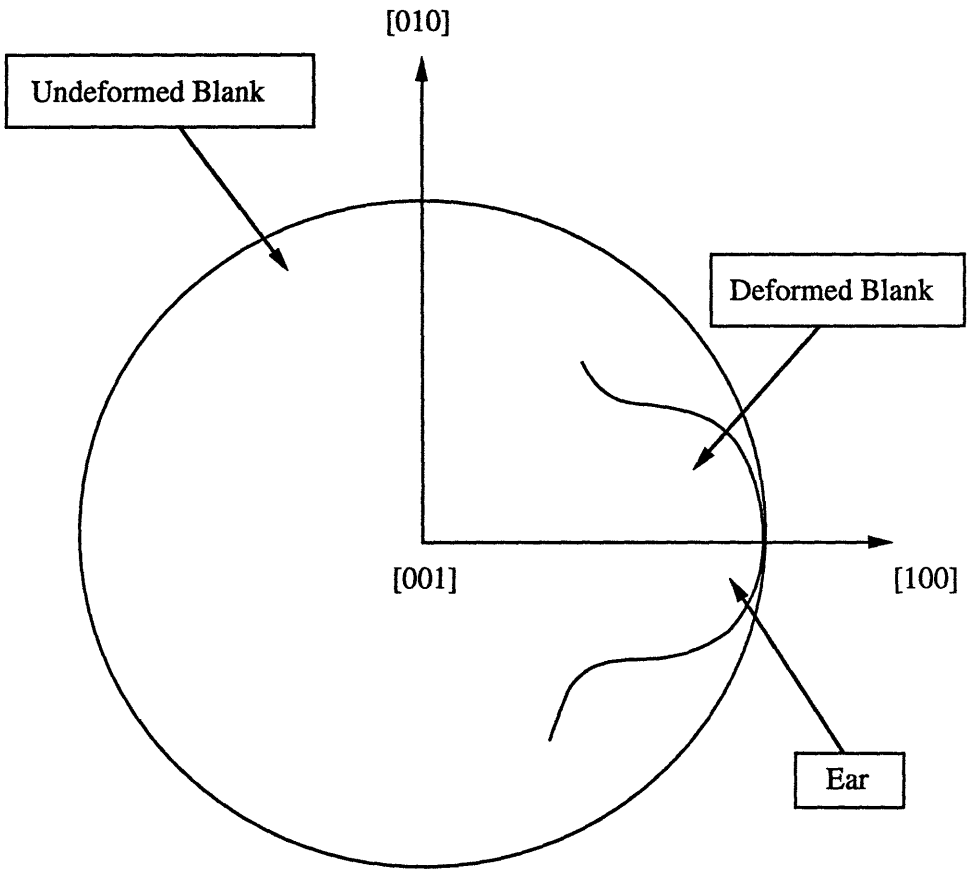

Figure 4-3: Schematic of the earing pattern observed in the drawing of fcc single crystals with the [001] direction oriented along the punch direction

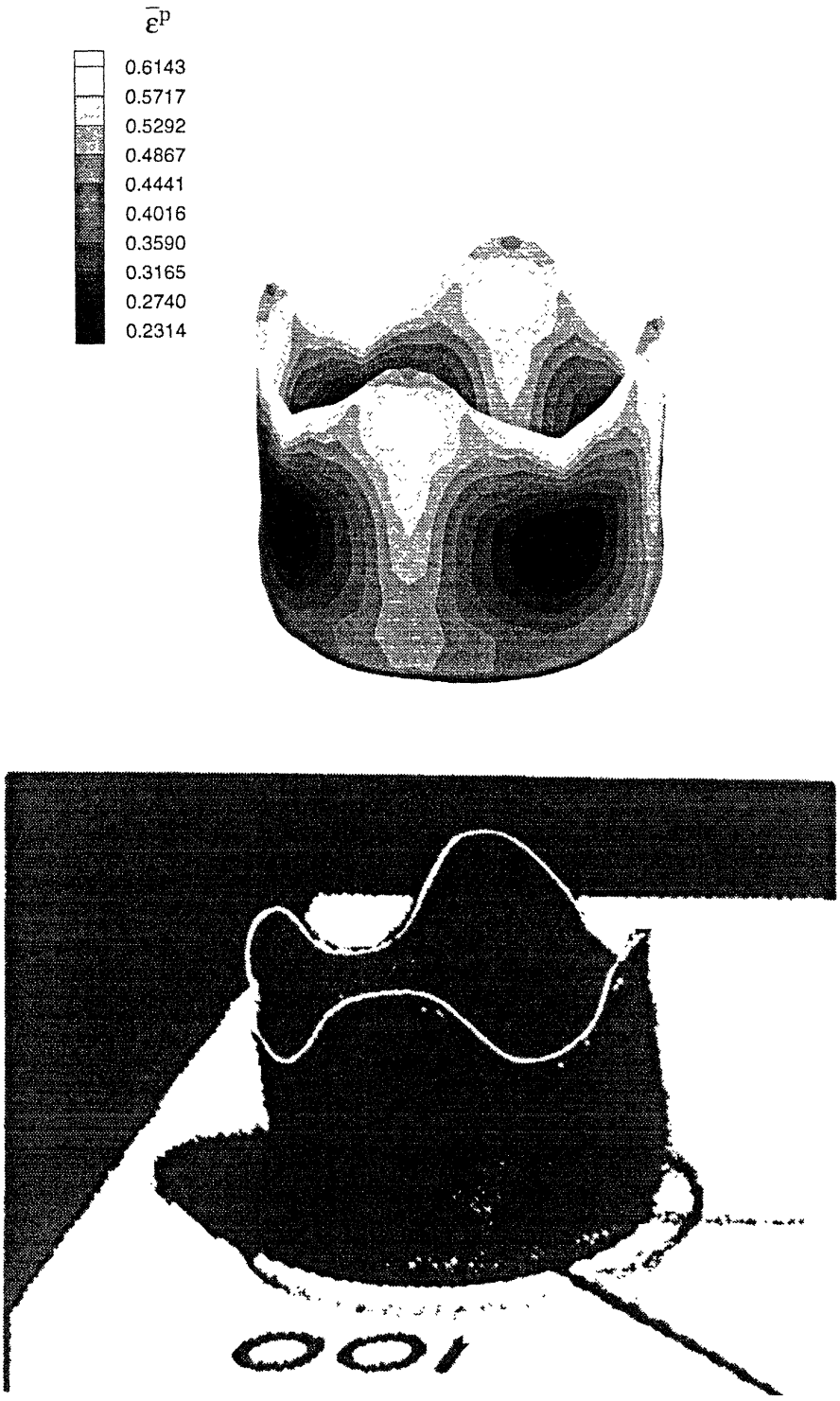

Figure 4-4: Equivalent plastic strain contours on a fully-drawn copper single crystal cup with the [001] direction oriented along the punch direction and the drawn aluminum cup in the same orientation [Tucker, 1961]

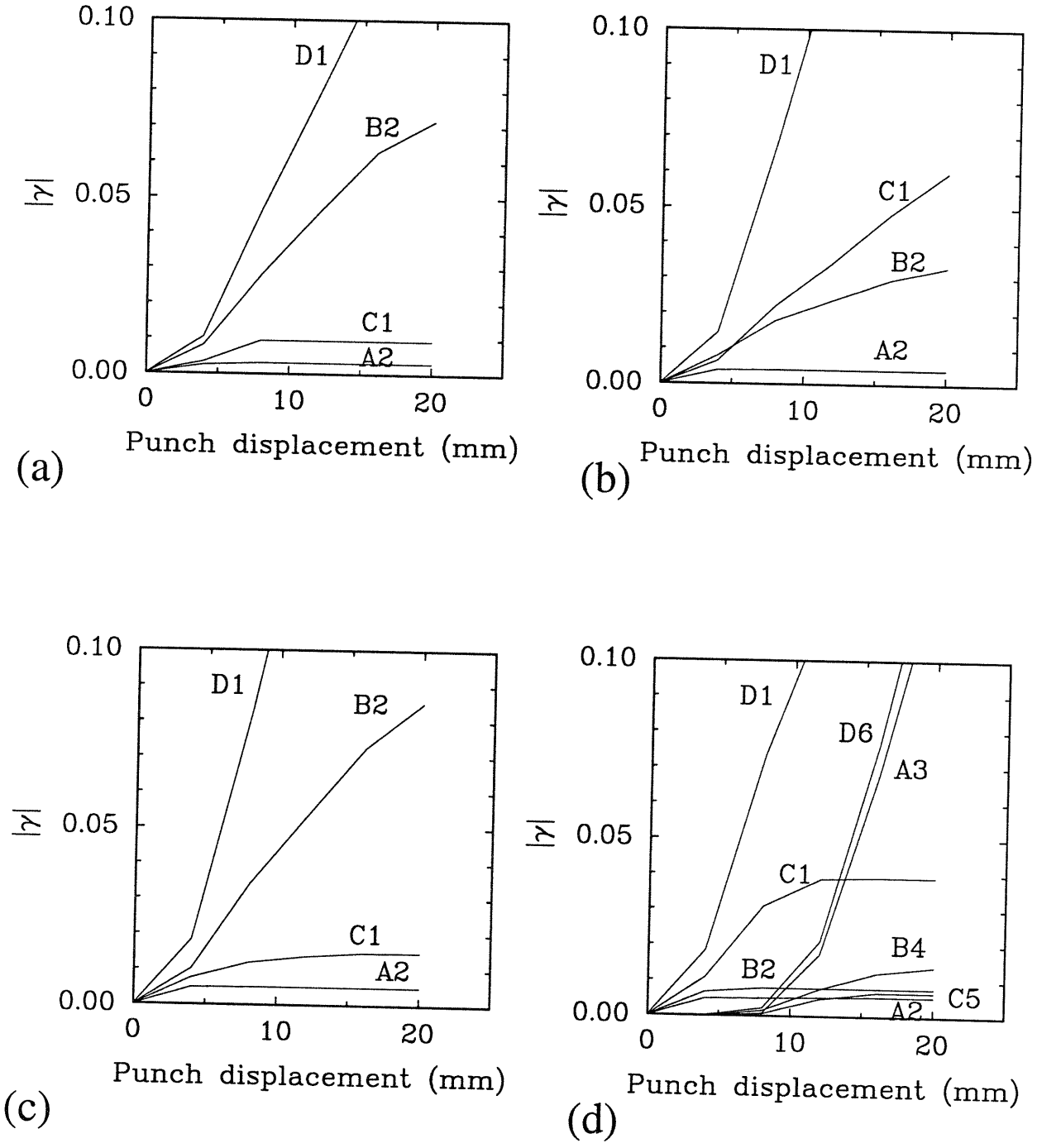

Figure 4-5: Slip-activity at different positions on the outer periphery of the blank in the [001] orientation: (a) 2.8125° plane (b) 8.4375° plane (c) 14.0625° plane (d) 19.6875° plane

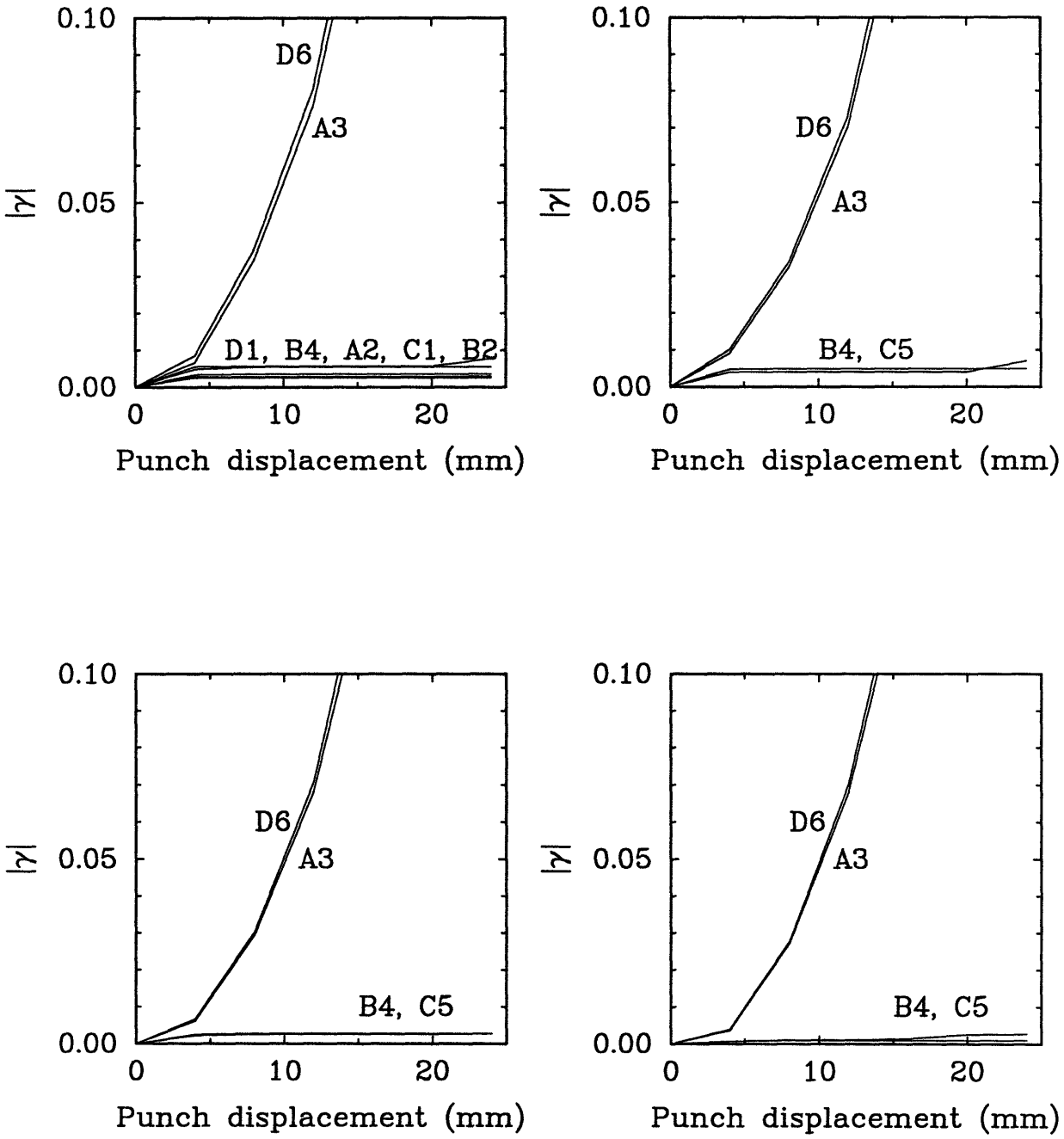

Figure 4-6: Slip-activity at different positions on the outer periphery of the blank in the [001] orientation: (a) 25.3125° plane (b) 30.9375° plane (c) 36.5625° plane (d) 42.1875° plane

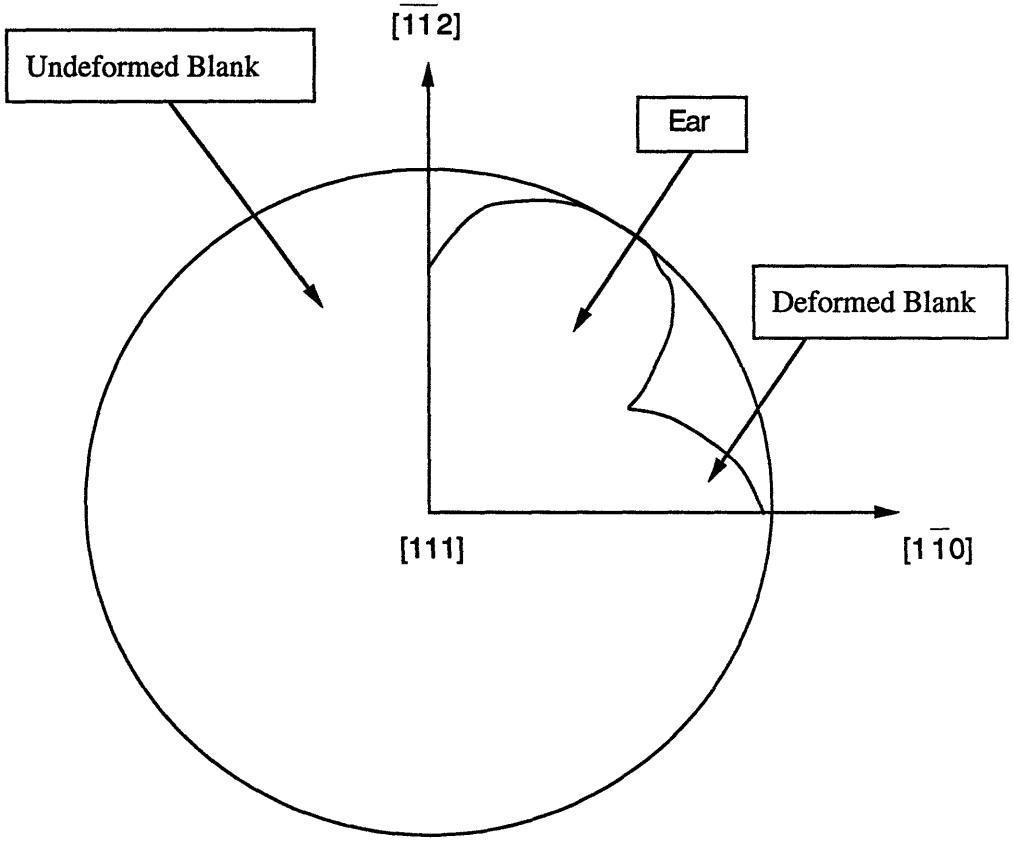

Figure 4-7: Schematic of the earing pattern observed in the drawing of fcc single crystals with the [111] direction oriented along the punch direction

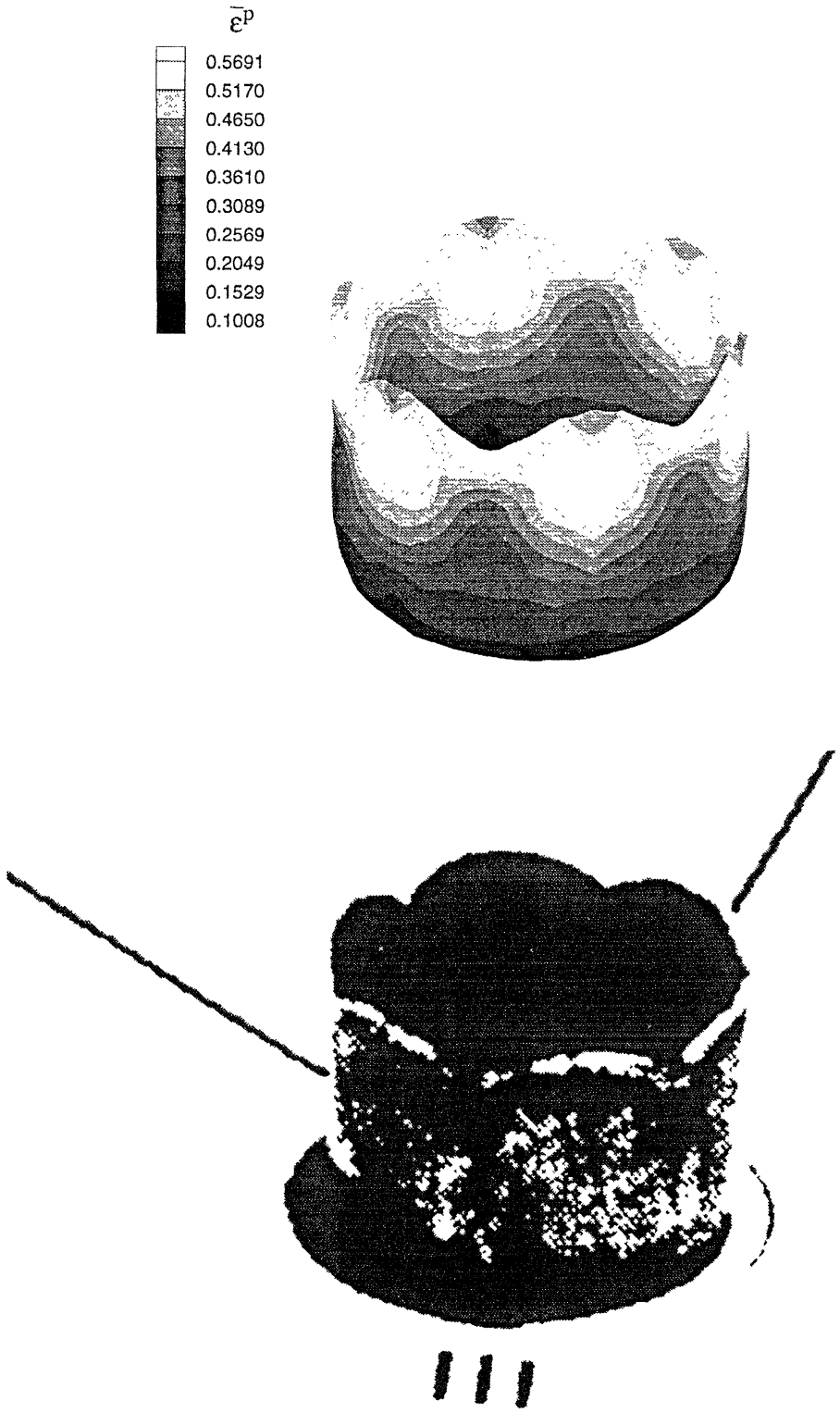

Figure 4-8: Equivalent plastic strain contours on a fully-drawn copper single crystal cup with the [111] direction oriented along the punch direction and the drawn aluminum cup in the same orientation [Tucker, 1961]

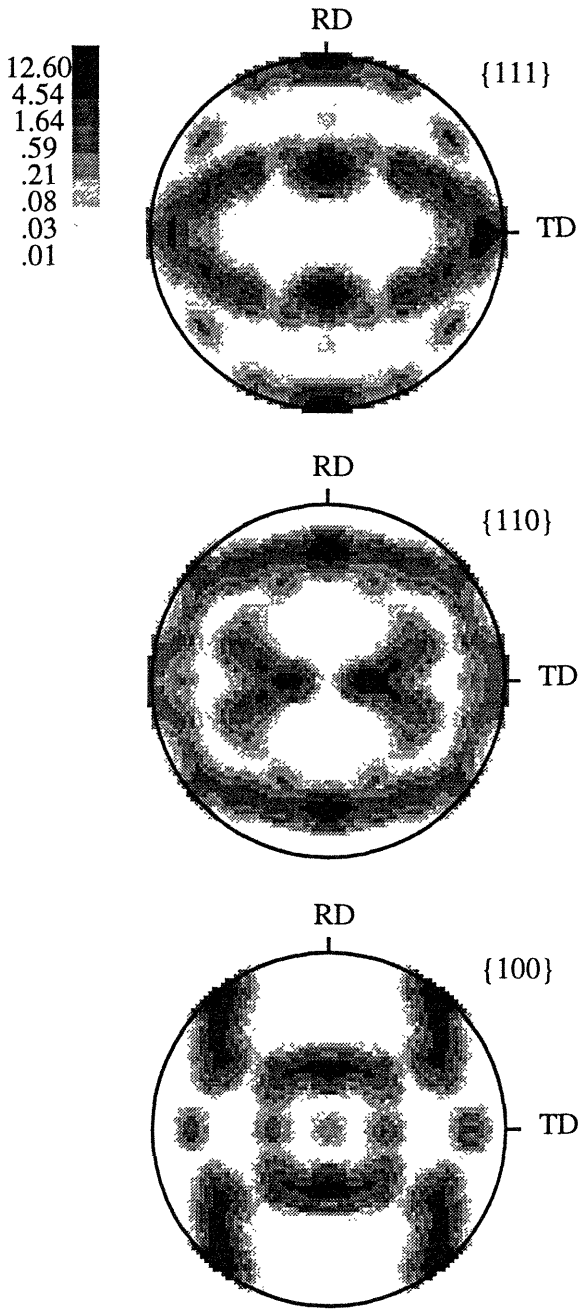

Figure 4-9: Initial rolling texture for the deep-drawing of polycrystalline copper represented by the plane-strain texture obtained by a plane-strain compression simulation on 21 weighted crystals with initial isotropic texture

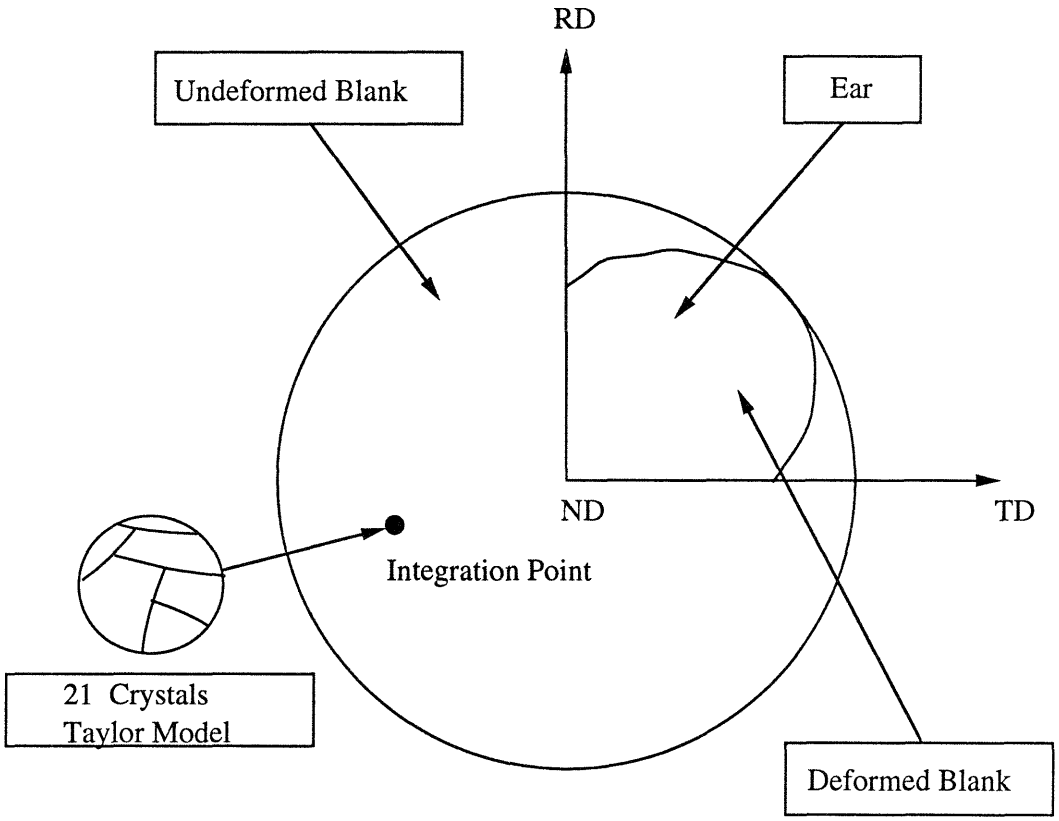

Figure 4-10: Schematic of the earing pattern observed in the drawing of fcc polycrystals

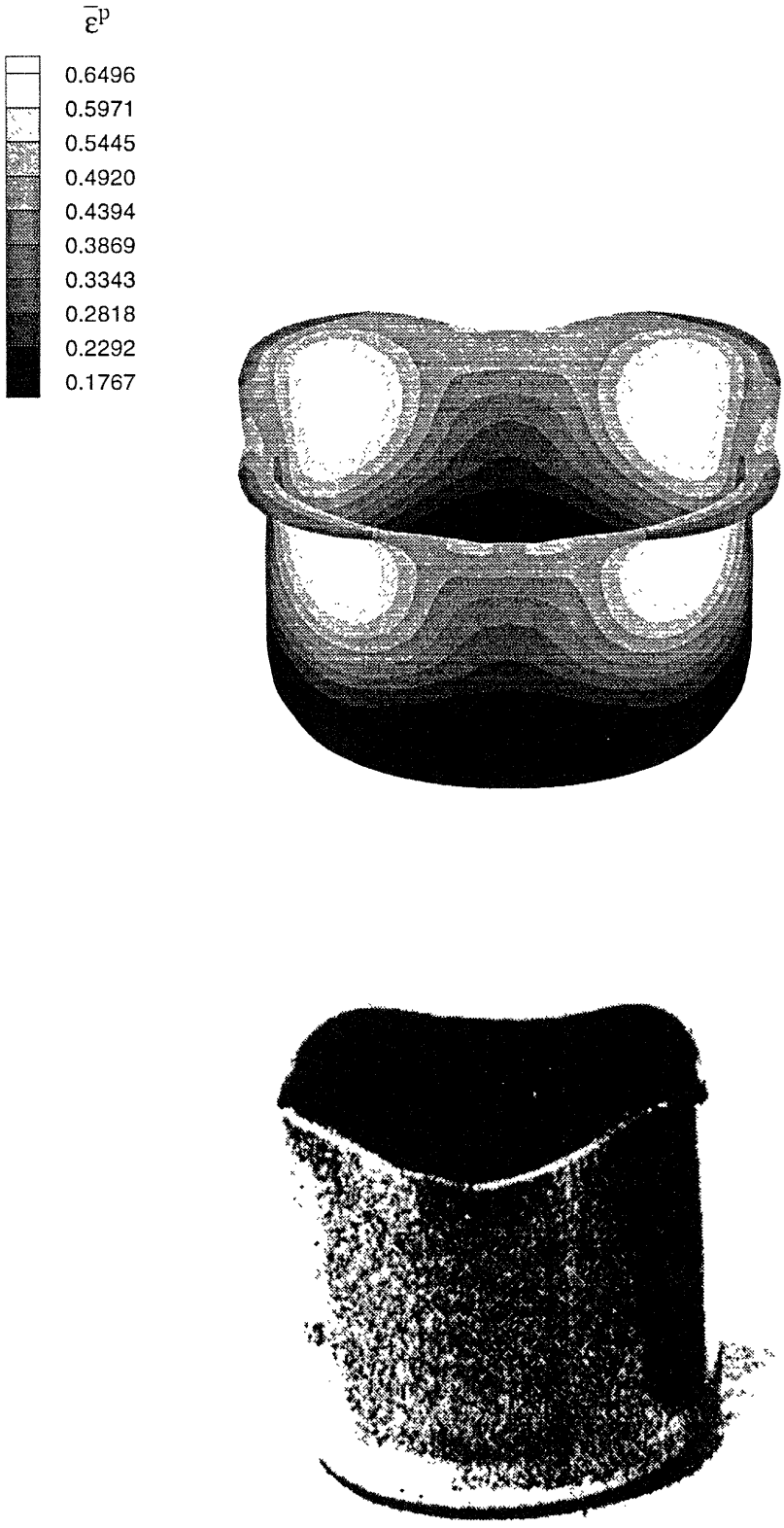

Figure 4-11: Equivalent plastic strain contours on a copper polycrystal cup with fully-developed ears with the rolling direction from left to right and the experimental result of Wilson and Butler, 1961 on copper with initial rolling texture

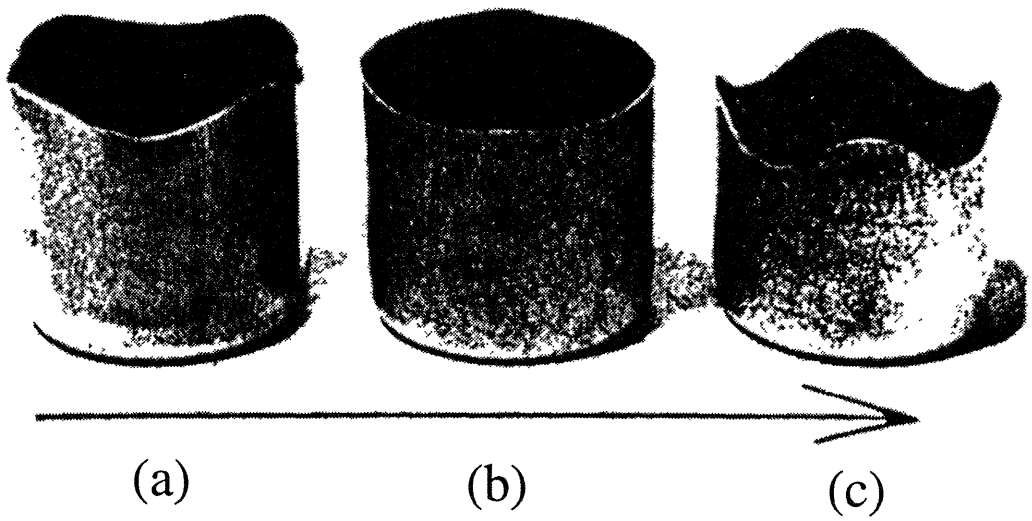

Figure 4-12: The earing behavior and maximum cup depths obtained in deep-drawing of copper [Wilson and Butler, 1961]: (a) Initial rolling type texture (b) Initial balanced texture (c) Initial cube texture. The arrow indicates the rolling direction in the sheets

Chapter 5

Closure

A rate and temperature dependent crystal plasticity model with a physically-based constitutive law for slip has been proposed. The predictions of the same for simple tension of single crystals for two different hardening forms have been investigated. Though some key aspects of the single crystal behavior are reasonably well-predicted, the hardening parameters do not directly carry over to the predictions for polycrystalline response. For the polycrystalline behavior, the form of the hardening used by Kalidindi *et al* has been found to give better predictions of evolution of texture and, hence, is retained.

The macroscopic response and evolution of texture are well-predicted at elevated temperatures where the material shows significant rate-sensitivity. The predictions of evolution of texture and load-displacement response are in agreement with the experimental results for the non-homogeneous deformation of axi-symmetric forging.

Finally, the predictive capability of the model in the formation of earing defects in cup-drawing of fcc single crystals and polycrystals has been demonstrated. The results are in qualitative agreement with some experimental observations.

The work is primarily directed towards a better design of deformation processing and the results have shown that a capability exists for the same. Future work along these lines would be to utilize the tools made available here to address some crucial practical issues like the optimization of mechanical properties (both at the macroscopic and microscopic levels), shape and loads. In particular, there is a need

to design a thermo-mechanical processing history so as to get a desirable initial state that would eliminate defects like earing.

Another matter of importance is the failure of products during processing e.g., tearing, wrinkling etc. in deep-drawing. There is a need to incorporate some first-order measures of damage accumulation in the model in order to predict the most probable modes of failure. Finally, experiments have to be conducted to validate the results quantitatively.

Appendix A

Time Integration Procedure

A.1 Time Integration Procedure for the Taylor-type Polycrystal Model

The time-integration procedure may be stated as follows. Let $\tau = t + \Delta t$. Then, given

(1) $\mathbf{F}(t)$, $\mathbf{F}(\tau)$, $\theta(t)$, $\theta(\tau)$

(2) $(\mathbf{m}^{\alpha}{}_{o}, \mathbf{n}^{\alpha}{}_{o})$ — time independent quantities, for each grain,

(3) $\{\mathbf{F}^{p}(t), s^{\alpha}(t), \mathbf{T}(t)\}$ in each grain,

calculate

(a) $\{\mathbf{F}^{p}(\tau), s^{\alpha}(\tau), \mathbf{T}(\tau)\}$ for each grain,

(b) volume averaged macroscopic stress $\bar{\mathbf{T}} = \sum_{k=1}^{N} v_k \, \mathbf{T}^{(k)}$,

(c) texture at time τ from

$$\begin{aligned} \mathbf{m}^{\alpha}{}_{\tau} &= \mathbf{F}^{*}(\tau)\mathbf{m}^{\alpha}{}_{o} = \mathbf{F}(\tau)\mathbf{F}^{p^{-1}}(\tau)\mathbf{m}^{\alpha}{}_{o}, \\ \mathbf{n}^{\alpha}{}_{\tau} &= \mathbf{F}^{*^{-T}}(\tau)\mathbf{n}^{\alpha}{}_{o} = \mathbf{F}^{-T}(\tau)\mathbf{F}^{p^{T}}(\tau)\mathbf{n}^{\alpha}{}_{o}, \end{aligned}$$

and march forward in time.

The steps in part (a) are ([Kalidindi *et al.*, 1992]):-

(i) Compute

$$\mathbf{A} \equiv \mathbf{F}^{p^{-T}}(t)\,\mathbf{F}^{T}(\tau)\,\mathbf{F}(\tau)\,\mathbf{F}^{p^{-1}}(t), \tag{A.1}$$

$$\mathbf{T}^{*tr} \equiv \mathcal{C}\left[\frac{1}{2}\{\mathbf{A}-\mathbf{1}\}\right], \tag{A.2}$$

$$\mathbf{B}^{\alpha} \equiv \mathbf{A}\mathbf{S}^{\alpha}{}_{o} + \mathbf{S}^{\alpha^{T}}{}_{o}\mathbf{A}, \tag{A.3}$$

$$\mathbf{C}^{\alpha} \equiv \mathcal{C}\left[\frac{1}{2}\mathbf{B}^{\alpha}\right] \tag{A.4}$$

(ii) Solve

$$\mathbf{T}^{*}(\tau) \doteq \mathbf{T}^{*tr} - \sum_{\alpha}\Delta\gamma^{\alpha}\mathbf{C}^{\alpha}, \tag{A.5}$$

$$s^{\alpha}(\tau) = s^{\alpha}(t) + \sum_{\beta} h^{\alpha\beta}(\tau)\mid\Delta\gamma^{\beta}\mid, \tag{A.6}$$

with

$$\Delta\gamma^{\alpha} \equiv \dot{\gamma}^{\alpha}(\tau)\,\Delta t, \tag{A.7}$$

for $\mathbf{T}^{*}(\tau)$ and $s^{\alpha}(\tau)$ using the following two-level iterative procedure.

In the first level of iterations, solve A.5 for $\mathbf{T}^{*}(\tau)$, keeping $s^{\alpha}(\tau)$ fixed at its best available estimate using a Newton-type iterative algorithm as follows:

$$\mathbf{T}^{*}{}_{n+1}(\tau) = \mathbf{T}^{*}{}_{n}(\tau) - \mathcal{J}_{n}^{-1}[\mathbf{G}_{n}], \tag{A.8}$$

where

$$\mathbf{G}_{n} \equiv \mathbf{T}^{*}{}_{n}(\tau) - \mathbf{T}^{*tr} + \sum_{\alpha}\Delta\gamma^{\alpha}\left(\mathbf{T}^{*}{}_{n}(\tau), s_{k}^{\alpha}(\tau)\right)\mathbf{C}^{\alpha}, \tag{A.9}$$

$$\mathcal{J}_{n} \equiv \mathcal{I} + \sum_{\alpha}\mathbf{C}^{\alpha}\otimes\frac{\partial}{\partial\mathbf{T}^{*}{}_{n}(\tau)}\Delta\gamma^{\alpha}\left(\mathbf{T}^{*}{}_{n}(\tau), s_{k}^{\alpha}(\tau)\right), \tag{A.10}$$

where the subscripts n and $n+1$ refer to estimates of $\mathbf{T}^{*}(\tau)$ at the end of n and $n+1$ iterations respectively, in the first level of the iterative scheme. The second level of

the iterative procedure involves a simple update (without iterations) of $s^{\alpha}(\tau)$ using

$$s^{\alpha}_{k+1} = s^{\alpha}(t) + \sum_{\beta} h^{\alpha\beta}\left(s^{\beta}_{k}(\tau)\right) \mid \Delta\gamma^{\beta}\left(\mathbf{T}^{*}_{n+1}(\tau), s^{\beta}_{k}(\tau)\right) \mid, \tag{A.11}$$

where the subscript k refers to the value of $s^{\alpha}(\tau)$ at the end of the k^{th} update in the second level of the iterative scheme.

In the rate-independent limit of plastic flow, *i.e.*, for large values of ΔF, the set of equations A.5 becomes very stiff and it becomes necessary to apply constraints to the Newton corrections (A.8) in the first level of the iterative procedure. In this work, the following constraint procedure has been adopted:

Let

$$\mid \Delta\gamma^{\alpha} \mid_{\max}(\tau) = \max_{\alpha} \mid \Delta\gamma^{\alpha}(\tau) \mid \tag{A.12}$$

If

$$\mid \Delta\gamma^{\alpha} \mid_{\max} < \Delta\gamma_{\mathrm{tol}}, \tag{A.13}$$

then accept the Newton correction, else

$$(T^{*}_{ij})_{n+1}(\tau) = (T^{*}_{ij})_{n}(\tau) + \eta\ \Delta T^{*}_{ij}, \tag{A.14}$$

where η is a small factor. A value of η of 0.25 was found to give good results in the calculations in this study.

(iii) Compute

$$\mathbf{F}^{p}(\tau) \doteq \left\{\mathbf{1} + \sum_{\alpha} \Delta\gamma^{\alpha}\mathbf{S}^{\alpha}_{o}\right\}\mathbf{F}^{p}(t). \tag{A.15}$$

It was necessary to normalize $\mathbf{F}^{p}(\tau)$ by dividing the computed values of each of its components by the cube root of the computed determinant so as to ensure that the determinant of $\mathbf{F}^{p}(\tau)$ is unity.

(iv) Compute

$$\mathbf{T}(\tau) = \frac{1}{\det \mathbf{F}(\tau)}\mathbf{F}(\tau)\mathbf{F}^{p^{-1}}(\tau)\mathbf{T}^{*}(\tau)\mathbf{F}^{p^{-T}}(\tau)\mathbf{F}^{T}(\tau) \tag{A.16}$$

After calculating the Cauchy stress in each crystal $\mathbf{T}(\tau)$, the Cauchy stress is averaged in part (b) and the orientation of the lattice is updated using part (c).

A.2 Time-stepping algorithm

In the implicit finite element procedure, the time-stepping is automatically controlled based on the maximum value of the slip increment. A parameter $R = \frac{\Delta\gamma^{\alpha}_{\max}}{\Delta\gamma_{\lim}}$ is used as a measure for controlling time-increments where $\Delta\gamma^{\alpha}_{\max}$ is the maximum value of $\Delta\gamma^{\alpha}$ over all the crystals and all the integration points in the finite element mesh and $\Delta\gamma_{\lim}$ is a prescribed value of slip increment based on the desired accuracy. A value of $\Delta\gamma_{\lim} = 0.02$ was found to give good results in this work. If the value of R is greater than 1 then the time-step is repeated with a time increment, $\Delta t_{\text{new}} = \frac{1}{2}\Delta t_{\text{old}}$. If $0.5 < R < 1$, the value of the time-increment is maintained and if $R < 0.5$, the time-increment is doubled *i.e.*, $\Delta t_{n+1} = 2\Delta t_n$. The efficiency and speed of the scheme depends on the rate- sensitivity of the material. The equations A.5 become stiffer in the rate-independent limit requiring more iterations to solve for the stresses.

For the explicit finite element scheme, a time-stepping scheme is not required and the problem is solved with nearly equal increments in time subject only to slight variations due to changes in the stability limit arising from changes in the geometry.

Bibliography

[ABAQUS, 1993] Hibbit, Karlson and Sorenson Inc., Providence, R. I. *ABAQUS, Reference Manuals*, 1993.

[Anand, 1985] L. Anand. Constitutive equations for hot-working of metals. *International Journal of Plasticity*, 1:213–231, 1985.

[Asaro and Needleman, 1985] R. J. Asaro and A. Needleman. Texture development and strain hardening in rate dependent polycrystals. *Acta Metallurgica*, 33:923–953, 1985.

[Barlat *et al.*, 1991b] F. Barlat, S. Panchanadeeswaran, and O. Richmond. Earing in cup drawing face-centered cubic single crystals and polycrystals. *Metallurgical Transactions. A.*, 22:1525–1534, 1991b.

[Bassani and Wu, 1991] J. L. Bassani and T. Y. Wu. Latent hardening in single crystals (ii). analytical characterizations and predictions. *Proceedings of the Royal Society of London*, A 435:21–41, 1991.

[Bassani, 1993] J. L. Bassani. Plastic flow of crystals. *Advances in Applied Mechanics*, 30:191–254, 1993.

[Becker *et al.*, 1993] R. Becker, R. E. Smelser, and S. Panchanadeeswaran. Simulations of earing in aluminium single crystals and polycrystals. *Modelling and Simulations in Materials Science and Engineering*, 1:203–224, 1993.

[Bronkhorst *et al.*, 1992] C. A. Bronkhorst, S. R. Kalidindi, and L. Anand. Polycrystalline plasticity and the evolution of crystallographic texture in fcc metals. *Philosophical Transactions of the Royal Society of London. A*, 341:443–477, 1992.

[Brown *et al.*, 1989] S. Brown, K. Kim, and L. Anand. An internal variable constitutive model for hot working of metals. *International Journal of Plasticity*, 5:95–130, 1989.

[Budiansky and Wu, 1962] B. Budiansky and T. Y. Wu. *Proceedings of the 4th U.S. National Congress on Applied Mechanics*, page 1175, 1962.

[Chastel and Mathur, 1991] Y. B. Chastel and P. R. Mathur. Comparison of polycrystalline rolling simulations with experiment: Modeling of the deformation of crystalline solids, (edited by lowe, t. c., rollett, a. d., follansbee, p. s. and daehn, g. s.). pages 225–238, 1991.

[Frost and Ashby, 1982] H. J. Frost and M. F. Ashby. *Deformation Mechanism Maps.* Pergamon Press, New York, 1982.

[Hutchinson, 1976] J. W. Hutchinson. Bounds and self-consistent estimates for creep of polycrystalline materials. *Proceedings of the Royal Society of London*, A 348:101–127, 1976.

[Kalidindi *et al.*, 1992] S. R. Kalidindi, C. A. Bronkhorst, and L. Anand. Crystallographic texture evolution in bulk deformation processing of fcc metals. *Journal of the Mechanics and Physics of Solids*, 40:536–569, 1992.

[Kalidindi, 1992] S. R. Kalidindi. *Polycrystal Plasticity: Constitutive Modeling and Deformation Processing.* PhD thesis, Massachusetts Institute of Technology, 1992.

[Kallend *et al.*, 1991] J. S. Kallend, U. F. Kocks, A. D. Rollett, and H. R. Wenk. popla - an integrated software system for texture analysis. *Textures and Microstructures*, 14-18:1203–1208, 1991.

[Kocks *et al.*, 1975] U. F. Kocks, A. S. Argon, and M. F. Ashby. Thermodynamics and kinetics of slip. *Progress in Material Science*, 19, 1975.

[Kocks, 1970] U. F. Kocks. The relation between polycrystal deformation and single-crystal deformation. *Metallurgical Transactions*, 1:1121–1143, 1970.

[Koiter, 1953] Koiter. page 1175, 1953.

[Lee, 1969] E. H. Lee. Elastic-plastic deformation at finite strains. *Journal of Applied Mechanics, Transactions of the ASME*, 36:1–6, 1969.

[Lush *et al.*, 1989] A. M. Lush, G. Weber, and L. Anand. An implicit time-integration procedure for a set of internal variable constitutive equations for isotropic elasto-viscoplasticity. *International journal of plasticity*, 5:521–549, 1989.

[Nagtegaal and Taylor, 1992] J. C. Nagtegaal and L. M. Taylor. Comparison of implicit and explicit finite element methods for analysis of sheet forming processes. 1992.

[Nye, 1957] J. F. Nye. *Physical properties of crystals: their representation by tensors and matrices.* Oxford University Press, London, 1957.

[Orowan, 1934] E. Orowan. *Zeit. Phys.*, 89:605,614,634, 1934.

[Pierce *et al.*, 1983] D. Pierce, R. J. Asaro, and A. Needleman. Material rate-dependence and localized deformation in crystalline solids. *Acta Metallurgica*, 31:1951, 1983.

[Polyani, 1934] M. Polyani. *ibid.*, 89:660, 1934.

[Rollett *et al.*, 1987] A. D. Rollett, G. R. Canova, and U. F. Kocks. The effect of the cube texture component on the earing behavior of rolled f.c.c. metals. *Proc. Conf. on Formability and Metalurgical Structures (edited by Sachdev, A. K. and Embury, J. D.)*, pages 147–155, 1987.

[Schmid and Boas, 1935] E. Schmid and W. Boas. *Plasticity of Crystals.* Chapman and Hall, London, 1935.

[Simmons and Wang, 1971] G. Simmons and H. Wang. *Single Crystal Elastic Properties and Calculated Aggregate Properties: A HANDBOOK.* The M.I.T. Press, Cambridge, 1971.

[Taylor and Elam, 1923] G. I. Taylor and C. F. Elam. The distortion of an aluminum crystal during a tensile test. *Proceedings of the Royal Society of London*, A 102:643–667, 1923.

[Taylor, 1934] G. I. Taylor. *Proceedings of the Royal Society of London*, A 145:362, 1934.

[Taylor, 1938] G. I. Taylor. Plastic strain in metals. *Journal of the Institute of Metals*, 62:307–324, 1938.

[von Mises, 1928] R. von Mises. *Z. angew. Math. Mech.*, 8:161, 1928.

[Wu *et al.*, 1991] T. Y. Wu, J. L. Bassani, and C. Laird. Latent hardening in single crystals (i). theory and experiments. *Proceedings of the Royal Society of London*, A 435:1–19, 1991.